

UNIVERSITY OF
BIRMINGHAM

[Towards experimental research on quantum thermodynamics with ultracold atoms]

by

Xi Wang

A thesis submitted to

The University of Birmingham

for the degree of

Doctor of Philosophy

School of Physics and Astronomy

College of Engineering and Physical Sciences

The University of Birmingham

February 2021

UNIVERSITY OF
BIRMINGHAM

University of Birmingham Research Archive

e-theses repository

This unpublished thesis/dissertation is copyright of the author and/or third parties. The intellectual property rights of the author or third parties in respect of this work are as defined by The Copyright Designs and Patents Act 1988 or as modified by any successor legislation.

Any use made of information contained in this thesis/dissertation must be in accordance with that legislation and must be properly acknowledged. Further distribution or reproduction in any format is prohibited without the permission of the copyright holder.

Abstract

This thesis is devoted to experimental research on non-equilibrium quantum thermodynamics using ultracold atoms. An ultracold atom cloud with 1×10^5 ^{87}Rb atoms are immersed in a cold ^{39}K MOT to investigate the novel thermodynamics of ultracold atoms in the presence of a dissipative environment. As a result, a metastable state with a finite BEC fraction at a temperature above the critical temperature has been observed in this system. The relaxation time of this state is longer than the typical experimental time scale (0.1 ms 100 ms). This result can be used as a tool to experimentally prepare a high condensate fraction state at a high temperature, it is also potentially to trigger the theoretical curiosity on the microscopic description of out-of-equilibrium quantum gases. Additionally, an experimental apparatus for trapping a single neutral ^{41}K atom has been also discussed. Once constructed, the single ^{41}K atom and the surrounding ultracold ^{87}Rb atom gas will act as the working fluid and the thermal bath and the quantum thermodynamics transformations are expected to be achieved in this system.

Acknowledgements

First of all, I would like to thank my supervisor Dr Giovanni Barontini, for giving me the opportunity to join this group, for his motivation, patience, and for sharing his knowledge. I also would like to thank Dr Anna Kowalczyk for her guiding and teaching, she always keeps encouraging me to work harder and shares her useful experience and knowledge which makes my job much easier than I thought.

I want to thank my coworker and friend Jorge Muñoz, for his great contribution and hard work in our project. With his can-do attitude and senses of humor, the long hours we have spent in our lab were great and happy. I also want to thank my colleagues, Dr Jixun, Aaron, Jamie, Nadine, Daniel, and Tom, for their help and guidance.

I also want to thank the people in Cold Atom group, including but not limited to Dr Vincent, Dr John, and Prof. Kai for the helpful discussion and support given to me throughout the years.

I would like to thank Ellie, Calton, and Joe, for their proofreading of my thesis and friendship.

Many thanks to all my friends in Birmingham and my family, your help and encouragement supported me through the whole duration of my PhD.

Table of Contents

1 Introduction **1**

1.1 Research background 1

1.2 Thesis overview 3

2 Fundamental concepts **5**

2.1 Basics of laser cooling and trapping: specific on ^{87}Rb,^{39}K,^{41}K 5

2.1.1 Laser cooling 5

2.1.2 Magneto-optical trap 7

2.1.3 Sub-Doppler cooling after MOT 8

2.2 Dipole trapping and creation of BEC 11

2.2.1 Optical dipole trap 11

2.2.2 Thermodynamics and characterization of BEC 12

2.3 Quantum heat engines 18

2.3.1 Single atom heat engine 18

2.3.2 Single atom in an optical tweezer 21

2.3.2.1 Species selective optical tweezer 21

2.3.2.2 Trapping potential and heating rate of the optical tweezer 22

2.3.2.3 Collisional blockade 23

2.3.3 Feshbach resonance 24

3 Experimental apparatus **27**

3.1 Vacuum system 28

3.2 Laser system . . . 30
3.2.1 Fibre preparation . . . 33
3.2.2 Magneto-optical trap . . . 38
3.2.3 Optical dipole trap . . . 40
3.3 Detection system . . . 45
3.4 Computer control system and data acquisition . . . 49
3.5 Optical tweezer . . . 54
3.5.1 Optical setup . . . 54
3.5.2 Tweezer loading and fluorescence imaging . . . 56

4 Results and discussion **60**
4.1 Non-equilibrium supercritical BEC . . . 60
4.1.1 Inducing dissipation in ^{87}Rb BEC . . . 60
4.1.1.1 Measuring the inter-species scattering rate . . . 62
4.1.1.2 Systematic correction of error in data analysis . . . 66
4.1.1.3 Calibration of trapping frequency . . . 70
4.1.1.4 Evolution of the thermodynamics parameters and phase diagram . . . 72
4.1.2 Relaxation towards equilibrium state . . . 79
4.1.3 Modeling the system . . . 80
4.2 Vortex conveyor belt for matter-wave coherent splitting and interferometry 85

5 Conclusions and Further Remarks **93**

References **102**

A appendix **103**
A.1 Locking system . . . 103
A.2 Design of TAs and AOMs . . . 107
A.3 Distillation of Zeeman sub-level . . . 108

A.4 Effort on producing a ^{39}K BEC 111

List of Figures

2.1 Excitation scheme of the ^{87}Rb atom 8

2.2 Schematic of the confining potential in one direction of a MOT. The ω_0 is the frequency of the atomic transition, the ω_{light} is the frequency of the laser, it is red detuned with respect to the atomic transition. The Zeeman splitting is linear expanded by a magnetic gradient along the z direction. Figure and caption taken from Ref [32]. 9

2.3 Observation of BEC with different expansion time. 17

2.4 From top to bottom: the schemes of the Quantum Carnot Engine (QCE), the Quantum Otto Engine (QOE), and the Quantum Diesel engine (QDE) realising in an ultracold single atom. The frequency of the harmonic confinement of the working fluid is changed in time in order to realise the compression or expansion on the single atom. The background colors (red→blue) indicate the temperature of the bath is changed from hot to cold. The (B → C) and (D → A) transformations are realised by decoupling the working fluid and the bath. Figure and caption taken from Ref [50]. 20

2.5 Choice of the wavelength of the species-selective optical tweezer: the behaviour of the dipole potential as a function of the wavelength for both Rb and K atoms. The magic wavelengths at which have zero dipole potential have already shown in the diagram. Figure and caption taken from Ref [55]. 22

2.6 Average number of atoms in the optical tweezer as a function of loading rate R for different waists. Figure and caption taken from Ref [53]. 24
2.7 Basic two-channel model for a Feshbach resonance. Figure and caption taken from Ref [57]. 25
2.8 Theoretical calculation of the inter-species scattering length as function of the magnetic field for the ^{41}K-^{87}Rb mixture in the |1,1> state. Figure and caption taken from Ref [55]. 26

3.1 Picture of vacuum setup from side view. 29
3.2 Excitation scheme of the ^{39}K and ^{41}K atoms. Where F and F' are the quantum numbers of the hyperfine ground states and the hyperfine excited states, the dashed lines represent the cross-over of the hyperfine ground states. The black (green) solid arrow is the cooling (repumping) transition. The dashed arrow is the locking frequency. 32
3.3 Schematics of the fibre transmission. 34
3.4 Schematics of the laser layout used for ^{87}Rb laser cooling. The input lasers are from 3 TAs and their frequencies are already locked. 35
3.5 Schematics of the laser layout used for ^{39}K laser cooling. The laser input is from Optica It is locked by the absorption spectroscopy shown in the figure. 36
3.6 Schematics of the laser layout used for ^{41}K laser cooling. The laser input is from Optica It is locked by the absorption spectroscopy shown in the figure. 37
3.7 Picture from the top of the vacuum system, with the 3D MOT chamber in the left and the 2D MOT chamber in the right. 40
3.8 Layout of the transmission of the laser beams for the optical dipole trap. Yellow (green) beam represents 1070 nm (1550 nm) beam. 41
3.9 Measurement of the widths for dipole trap beams. left (right) beam represents 1070 nm (1550 nm) beam. 42

3.10 Trapping frequency measurement through parametric heating approach: The average width of the atom cloud in the optical dipole trap has been measured after 20ms TOF as a function of the modulation frequency applied to the 1070nm trap beam. The depth of the modulation is 10% of the total beam power. 43
3.11 Trapping frequency measurement through collective mode of BEC: The centre mass of the atom cloud in the optical dipole trap has been measured with 20ms TOF after a magnetic gradient pulse and a variable amount of holding time. 44
3.12 Schematics of the imaging system. 46
3.13 Temperature measurement of the ultracold atoms. The black solid dots are the experimental measurement of $\sigma^2 = \sigma_x^2 + \sigma_y^2$. The red line is the linear fit of σ^2 over the square of the expansion time t^2. 48
3.14 Schematic of control system. 50
3.15 The experimental sequence on the interface of Cicero. 50
3.16 The experimental sequence for ^{87}Rb BEC. 51
3.17 Measurement of the atoms in the optical dipole trap. The atoms are trapped by the laser at wavelength 1070 nm with power 12 W. The photo is taken from the horizontal imaging system. 52
3.18 Absorption image of a BEC after 25 ms ballistic expansion. 53
3.19 Absorption measurement of BEC with different BEC fraction. (top left) fitting by the Gaussian profile, (bottom right) fitting by the Thomas-Fermi profile, (top right and bottom left) fitting by the bi-model distribution. . . 54
3.20 Schematics of the optic layout for the optical tweezer. 55
3.21 Sequence of the fluorescence imaging of the ^{41}K atoms in the optical tweezer. 56
3.22 (left) measurement of the fluorescence of the atoms in the optical tweezer. Readout from the histogram measurement corresponding to these data set, we can deduce that 5 atoms are in the optical tweezer. 58

3.23 (left) Florescence imaging of the atoms in the tweezer versus the detuning of the cooling light, (right) florescence imaging of the atoms in the tweezer versus the detuning of the repumping light. 59

4.1 a) Schematic demonstration of the distillation protocol. we switch on an MOT of ^{39}K during the last stages of the ^{87}Rb evaporative cooling. This provides a dissipative environment for the ^{87}Rb atoms. b) The red dots are the measured densities of the ^{39}K atoms as a function of time. The blue diamonds are the measured dissipation rates of the ^{87}Rb while the blue shaded area is the calculated dissipation rate by the model explained in the text. Error bars are the standard errors of the mean. Figure and caption taken from Ref [27] 61

4.2 Experimental sequence used to study the dissipation rate of the ^{87}Rb atoms in ^{39}K MOT. 63

4.3 ^{87}Rb atom number as a function of time for a condensate (upper panel) and a thermal gas (lower panel). The blue points and curves correspond to the measurement without the dissipation. The green points and curves correspond to the measurement with the dissipation. 65

4.4 Δ versus N_{th}/T without dissipation in a viable amount of intensity of push beam for ^{87}Rb atom 67

4.5 Δ versus N_{th}/T with dissipation in a viable amount of ^{39}K MOT loading time 68

4.6 α and β without dissipation as a function of ^{87}Rb MOT push intensity. $\alpha_1\beta_1$,$\alpha_2\beta_2 are from the different datasets.$ 69

4.7 α and β without dissipation as a function of ^{39}K MOT loading time. $\alpha_1\beta_1$,$\alpha_2\beta_2 are from the different datasets.$ 70

4.8 Measurement of the trapping frequency. The red dots are the mean trapping frequency $\omega/2\pi$ calculated from eq. 4.11 and the equation $T_c = 0.94\hbar\omega N^{1/3}/k_B$. The blue triangles are the mean trapping frequencies measured using parametric heating and centre of mass oscillations. The lines are linear fits to the data, the coefficients are reported in the legend. Figure and caption taken from Ref [27] 71

4.9 Measured parameters of the ^{87}Rb sample as a function of time. Red circles are with dissipation (distillation) and blue triangles are without dissipation. a) The total number of atoms. b) The temperature c) The condensate fraction F. The red dotted dashed line and the blue dashed line show the expected fraction from Eq. (1) for with and without dissipation respectively. d) The chemical potential of the thermal part in units of temperature. The dashed and dash-dotted lines are the chemical potential of the BEC with and without dissipation respectively. Error bars and the shaded regions are the standard errors of the mean. Figure and caption taken from Ref [27] 73

4.10 Phase diagram showing the BEC fraction as a function of reduced temperature τ. The open symbols are for the case of no dissipation while filled symbols are the trajectories during our distillation protocol. For open diamonds and circles, the wait time after the end of the evaporation ramp is 4 s, while for others it is 20 ms. For the filled circles the dissipation rate is 4 times the dissipation rate of the filled squares. For the data in absence of dissipation, we vary the number of atoms from 7×10^4 to 2.5×10^4 at t = 1s in order to explore as much parameter space as possible. The solid blue line corresponds to Eq. 4.11. The dotted lines are the results of the rate equation model described in the latter. Error bars are the standard errors of the mean. Figure and caption taken from Ref [27] 75

4.11 Same as the Fig. 4.9, but with the dissipation rate increased by a factor of 4, corresponding to filled circles in Fig. 4.10. Figure and caption taken from Ref [27] 76
4.12 Same as Fig. 4.10 but using the Bose-enhanced polylogarithm to fit the data. Figure and caption taken from Ref [27] 78
4.13 Difference between the measured F and that expected using Eq. (4.8) after the dissipation from the ^{39}K MOT is switched off and the sample is held with constant trap depth. Error bars are the standard errors of the mean. The line shows an exponential fit to the data after 1.5 seconds, when the supercritical gas relaxes towards equilibrium. The time constant is 3.9 ± 0.3 s. Figure and caption taken from Ref [27] 79
4.14 Pictorial representation of our rate equation model. Figure and caption taken from Ref [27] 81
4.15 From left to right, evolution as a function of time of the atom number (in thousands) in the thermal component, the atom number in the BEC (in thousands) and the condensate fraction F. The points are the experimental data, the line are the results of our model. Figure and caption taken from Ref [27] 84
4.16 a) Phase pattern resulting from the imprinting of Eq. 4.20 with l = 1. b) Phase pattern generated by Eq. 4.21 with d = 0:25. c) and d) are the corresponding velocity fields. Figure and caption taken from Ref [28]. . . . 88
4.17 Column density profiles of the BEC at different evolution times t after the phase imprinting. (a)-(f) shows the dynamics after the imprinting of Eq. 4.20, while (g)-(l) of Eq. 4.21 Note that for t=0.24 and 7.7 the axis range is reduced to better show the initial formation of the vortex conveyor belt and the final interference patterns. Figure and caption taken from Ref [28]. 89

4.18 Initial exit velocity along the y-axis v_y vs. half initial vortex distance d after the imprinting of the pattern in Eq. 4.21. The blue circles and the red squares represent the values obtained by fitting the simulated density profiles with the procedure explained in the text. The solid lines are calculated with $v_y = d\phi_1/dy$ with l = 4d. Figure and caption taken from Ref [28]. 91

4.19 Phase of the interference fringe α vs. acceleration β for different values of the phase imprinting coefficient l or d. The filled symbols are the results of the numerical simulations after imprinting the pattern in Eq. 4.20. The solid lines are linear fits to the data. The open points are data extracted from the simulations resulting from the imprint of Eq. 4.21. The dashed line is the corresponding linear fit. Figure and caption taken from Ref [28]. 92

A.1 Frequency modulation spectroscopy. Left panel: the error signal for ^{87}Rb; right panel: the error signal for ^{85}Rb. 104

A.2 Schematic principle of the offset locking: The beat signal is from a fast PD and amplified with up to 40 60dB. The power is split into two signals for a purely diagnostic reason. One is checked by a spectrum analyzer. The mixer produces a series of algorithm signals by mixing with a signal from the VCO. The consequent beat spectrum is filtered with a low pass filter, its high order contribution is removed. With the aid of another power splitter, the signal is split in half. One half passes through a constant -3dB attenuator, the other half passes through a high pass filter which has a cutting frequency at 3dB. Given that the frequency is above or below the cutting frequency, the signal experiences a larger or smaller attenuation. The amplitude response of the two signal paths is compared in the RF balance detector that gives out a voltage varying between positive and negative given which of the two signals is greater. Figure and caption taken from Ref [100]. 106

A.3 Layout of the tapered amplifier: the incident seeding laser passes through a polariser (P) and is focused onto the tapered amplifier chip by a lens (L). The output laser is collimated by the collimation lens and its astigmatism is compensated by a cylindrical lens. Figure and caption taken from Ref [100]. 107

A.4 Double pass regime of AOM: The linear polarised laser passes through a polarising beam cube (PBC) and the AOM. A lens (L) with a focus length of f=15cm focuses the laser onto a mirror (M). The laser passes twice through a quarter-wave plate (1/4 WP) and obtains a total polarisation shift of $\lambda/2$ followed by passing through the AOM for a second time. The output beam is deflected by the PBC to the perpendicular direction with respect to the incident beam.Figure and caption taken from Ref [100]. . . 108

A.5 Theoretical plots of Rabi oscillations. The red, green and blue lines correspond to the m_F=+1,0,-1 states respectively. Typical Rabi oscillations with different detuning are shown. In the left column from top to the bottom it illustrates the oscillation with detuning Δ=$0, 0.3\Omega_{RF}, 0.7\Omega_{RF}$, in the right column the oscillations with detuning $\Delta = \Omega_{RF}, 2\Omega_{RF}, 3\Omega_{RF}$ have been demonstrated. 110

A.6 Absorption imaging of different Zeeman components of the ^{87}Rb atoms . . 111

A.7 Measurement of the atom number and the temperature after the sub-Doppler cooling of the ^{39}K atoms. 112

A.8 Loading ^{39}K atoms in the optical dipole trap. 112

List of Abbreviations

$\hbar$	Reduced Planck constant constant ($\hbar/2\pi$= 1.05457187×10^{-34} m^2kgs^{-1}).
k_B	Boltzmann constant (= 1.38×10^{-23} J K^{-1}).
amu	Atomic Mass Unit (= 1.66×10^{-27} kg).
AOM	Acousto-optic modulator.
BEC	Bose-Einstein Condensate.
ECDL	External-cavity diode lasers.
EOM	Electro-optic modulator.
Laser	Light amplification by stimulated emission of radiation.
PID	Proportional–integral–derivative controller.
TA	Tapered amplifier.

Chapter 1

Introduction

1.1 Research background

Thermodynamics plays a pivotal role in modern technologies and physics. The refrigerator and heat engines, both of which improve the quality of our daily lives, are based on classical thermodynamics cycles. It was already predicted by Feynman in the 60s that technological progress would eventually make it possible to realise a small scale machine consisting of a few atoms, or potentially even a single atom. In contrast to classical machines, quantum mechanics can play a role in a small scale machine [1, 2]. Unlike other well-developed fields in quantum science, non-equilibrium quantum thermodynamics (NEQT), which aims to put quantum processes forward to the stochastic thermodynamics perspective, is still new [3]. In recent years, several theoretical studies have been put forward to address the role of thermodynamics in quantum engines [4–6]. It has been also indicated that a heat engine operating in the quantum regime can have higher efficiency than its classical counterpart [7, 8]. A few experimental attempts to realise highly efficient nano- and micro-engines, based on NEQT and taking advantage of quantum coherence have also been seen [9]. For example, nitrogen-vacancies in diamonds [10] and ultracold atoms [11] have been used to realise heat engines with quantum features.

At temperatures close to the absolute zero, the De Broglie wavelength associated with

an atom can be larger than the average distance between atoms in a dilute atom gas, resulting in collective behaviors dominating the system. By using evaporative cooling, a cloud of bosonic atoms can be brought to such temperatures where a Bose-Einstein condensate (BEC) is realised [12]. This phase transition is only possible when the temperature is below the critical temperature T_c. Due to its quantum properties and microscopic scale, a BEC is considered as an ideal candidate for the investigation of quantum thermodynamics and for the implementation of small scale engines.

The thermodynamics of the BEC can be also affected by the environment, for example through collisions. In the last few decades, collisions between different atomic species have been investigated [13]. In a multiple atomic species, one of the species can be used as the working fluid and the other as a thermal bath. The inter-species collisions can induce heat exchange between the working fluid and the thermal bath. In some circumstances, such collisions can also induce losses of atoms. This dissipative environment is usually considered as a detrimental effect on the collective and quantum properties of the working fluid. However, if properly tamed, it can also play productive roles, such as creating novel states of matter [14, 15] and generating quantum entanglement [16]. Recently, dissipation driven states which are not accessible in equilibrium have been observed [17], and considerable attention has been paid to the non-equilibrium evolution in an ultracold atom system [18]. Thanks to the use of techniques such as optical traps, optical tweezers, optical lattices, etc, the research scope of the non-equilibrium regime can be expanded to a wide range of systems, including low dimensional Bose gases [19, 20], quenched quantum gases [21, 22] and prethermalized states [23].

In this thesis, I present an experiment to study the thermodynamics of a BEC in a dissipative environment. We realised a novel non-equilibrium phase, which is denoted as the supercritical BEC. By controlling the dissipation rate, a long-lived metastable state can be observed with a finite BEC fraction when the temperature of the ultracold atoms is above the critical temperature.

Furthermore, trapping and manipulating single atoms have drawn much attention in

the last decade, and the near-deterministic preparation of a single atom in an optical microtrap has been achieved [24]. Later, some new experimental developments focusing on engineering a few particles in operating heat engines have been seen [25]. Presently, only one work achieving a single atom engine operating fully in the classical regime has been seen [26]. In this thesis, I also present some preliminary work to produce a quantum heat engine using a system consisting of a single neutral atom immersed in an ultracold atom cloud, where the single atom acts as the working fluid and the ultracold atom cloud as the thermal bath.

1.2 Thesis overview

This thesis describes the steps taken to set-up an experimental apparatus to investigate the non-equilibrium thermodynamics in the ultracold atoms. We consider a two species ultracold mixture ^{87}Rb-^{39}K. The ^{87}Rb atoms are trapped in a dipole trap and transit into a BEC through evaporative cooling. They have immersed in the ^{39}K atoms, which are confined in a 3D MOT. Due to the large temperature gap between the two species, the collision is nearly elastic and the heat exchange from the collision can be ignored. The ^{39}K atoms are therefore a dissipative environment for the ^{87}Rb BEC. We investigate the influence of dissipation on the thermodynamics of the BEC. Furthermore, we also aim to investigate the quantum thermodynamics of a single-atom and the possibility to achieve a heat engine in the quantum regime with the ultracold mixture ^{87}Rb-^{41}K.

The thesis is organized in the following way:

The theoretical and experimental background relevant for our experiment is first presented. The basic concept of laser cooling and its application on the relevant species, including the MOT, evaporative cooling, and the phase transition to a BEC, furthermore, the fundamental concept and of a single-atom heat engine in the quantum regime and the experimental techniques required for its realisation are reviewed.

In chapter 3, the experimental apparatus is illustrated in detail. The vacuum system,

laser system, the sequence to produce ultracold atoms, the detection system, and the computer-based control system are discussed. At the end of this chapter, the setup for the single-atom trapping and its measurement are also reported.

In chapter 4, the experimental result of the evaporative cooling in a dissipative environment is fully discussed. The thermodynamics of the ultracold atom cloud is analysed in the presence and absence of dissipation. In contrast to the case in equilibrium, we found that the system can be driven into a metastable state in a non-equilibrium regime with dissipation. The relaxation property of this state has also been investigated. Additionally, a phenomenological theoretical explanation that may favor the further progress on rigorous microscopic theory is provided. The results have been published in [27].

At the end of this chapter, I also discuss a numerical study on a novel atom interferometer and its potential application as a compact and high precision accelerometer that was completed as a side project of my thesis. It has also been published in [28].

Chapter 2

Fundamental concepts

2.1 Basics of laser cooling and trapping: specific on ^{87}Rb,^{39}K,^{41}K

2.1.1 Laser cooling

Consider a moving atom with momentum $\vec{p} = m\vec{v}$ in a laser field, where m and $\vec{v}$ are the mass and velocity of the atom. We assume the atom is a two-level system, with ground state$|g\rangle$ and excited state $|e\rangle$. When the wavelength of the laser is near-resonant with respect to the atomic transition $|g\rangle \rightarrow |e\rangle$, an optical cycle of the atom can be driven by absorbing and emitting photons continually. During this cycle, when the atom absorbs a photon traveling from the opposite direction with a momentum $\vec{p} = \hbar\vec{k}_{photon}$, where $\hbar$ is the Plank constant and $\vec{k}_{photon}$ is the wave vector of the photon, defined as $\vec{k}_{photon} = 2\pi/\lambda$, with λ being the wavelength, the velocity of the atom changes by $\hbar\vec{k}_{photon}/m$, as it is given a momentum kick from the photon. Assuming any spontaneous decay is isotropic, the total momentum transfer in the photon absorption and emission process is nonzero. A radiation force, or friction force, can therefore be produced. This effect is analogous to a particle moving in a viscous fluid and is therefore referred to as viscous-like cooling or optical molasses. The radiation force, $\vec{F} = -a \cdot \vec{v}$, is always in the opposite direction to

the velocity of the atom.

In the weak-field approximation, the number of optical cycles per second scales as the spontaneous emission rate, $1/\tau = \Gamma/2\pi$, where Γ is the linewidth of the excited state and τ is the lifetime of the excited state of atom. The momentum change of the atom is determined by the number of scattered photons per unit time, which is referred to as scattering rate $R_{sc} = \Gamma\rho_{ee}$. The radiation force can be expressed as $\vec{F} = \hbar\vec{k}\Gamma\rho_{ee}$. Where ρ_{ee} is the occupation probability of the excited state,

$$\rho_{ee} = \frac{1}{2}\frac{I_R}{1 + I_R + \frac{4}{\Gamma}(\Delta - \frac{\nu_L}{c}v)^2}, \tag{2.1}$$

where I_R is the relative laser intensity with respect to the saturation intensity, ν_L is the radiation frequency and Δ is the detuning of the photons with respect to the atomic transition. (Saturation intensity: in some materials, the absorption rate of light decreases with increasing light intensity, the saturation intensity is the maximum of the photon absorption.) The moving atoms have a velocity-dependent detuning with respect to a laser, $\Delta_{Doppler}=\vec{k}\cdot\vec{v}$, meaning the scattering force is therefore velocity-dependent. By manipulating the detuning, one should be able to address a group of atoms with a chosen velocity.

The velocity distribution of atoms at a finite temperature is ruled by the Maxwell-Boltzmann distribution. The average velocities of the Rb atoms and the K atoms at room temperature are 292 m/s and 431 m/s, respectively. The viscous-like force can be used to reduce the average velocity of the atoms, which in turn lowers the temperature of the atoms. However this force cannot cool the atoms indefinitely, the fundamental limits on the lowest attainable temperature are (1) the recoil temperature T_R : $\frac{1}{2}k_BT_R = \frac{1}{2m}(\frac{\hbar\nu_L}{c})^2$, which is based on the fact the photon momentum is discrete in quantum regime and the quantum indetermination cannot be broken up to reach a lower temperature; (2) the Doppler temperature T_D :$k_BT_D = \frac{\hbar\Gamma}{2}$, which corresponds to the natural linewidth of the atomic transition.

2.1.2 Magneto-optical trap

Cooling and trapping atoms from the background gas are the beginning stages in cold atom experiments. A commonly used technique is the magneto-optical trap (MOT), where moving atoms can be decelerated and trapped in the presence of pairs of counter-propagating beams and a magnetic field gradient. [29].

The photon scattering rate inversely scales as the frequency detuning between the wavelength of light and the intrinsic atomic transition. For alkali metal atoms, when the laser frequency is near-resonant, the intensity balanced counter-propagating beams can be used to dramatically decelerate the average velocity of moving atoms. For example, in our experiment, the moving ^{87}Rb atoms at room temperature can be decelerated to less than 1 m/s in a few ms.

However, this viscous-like force cannot be used to trap the atoms, meaning the atoms can diffuse out of the beam region. As a solution, a position-dependent trapping force is created by applying an additional magnetic field gradient with the orthogonal circular polarised ($\sigma^+ - \sigma^-$) counter-propagating beams.

Combining the viscous-like force and position-dependent force, we obtain

$$\vec{F} = \vec{F}_{\sigma^+} + \vec{F}_{\sigma^-} = \frac{\hbar\vec{k}\Gamma}{2}\left[\frac{I_R}{1+4(\frac{\Delta - Kv - Bz}{\Gamma})^2} - \frac{I_R}{1+4(\frac{\Delta - Kv + Bz}{\Gamma})^2}\right] = -\alpha\vec{v} - \vec{k}z \qquad (2.2)$$

where $-\alpha\vec{v}$ is the viscous-like force and $-\vec{k}z$ is the position-dependent force. To expand this equation into a 3-dimensional frame, the mechanism of a 3D MOT can be fully explained.

Additionally, for achieving efficient laser cooling, the atomic transition must be a closed cycle. This in turn means the atoms should be undissipatively driven between states. During an optical pump, the excited atomic state can spontaneously decay to lower states and result in an irreversible atom loss. In the ^{87}Rb case, the excitation scheme for has been shown in Fig. 2.1, the laser is locked at the resonant frequency with

respect to the D2 line atomic transition from the ground hyperfine level $|F = 2>$ to the crossover of the two excitation hyperfine levels $|F' = 2>$ and $|F' = 3>$.

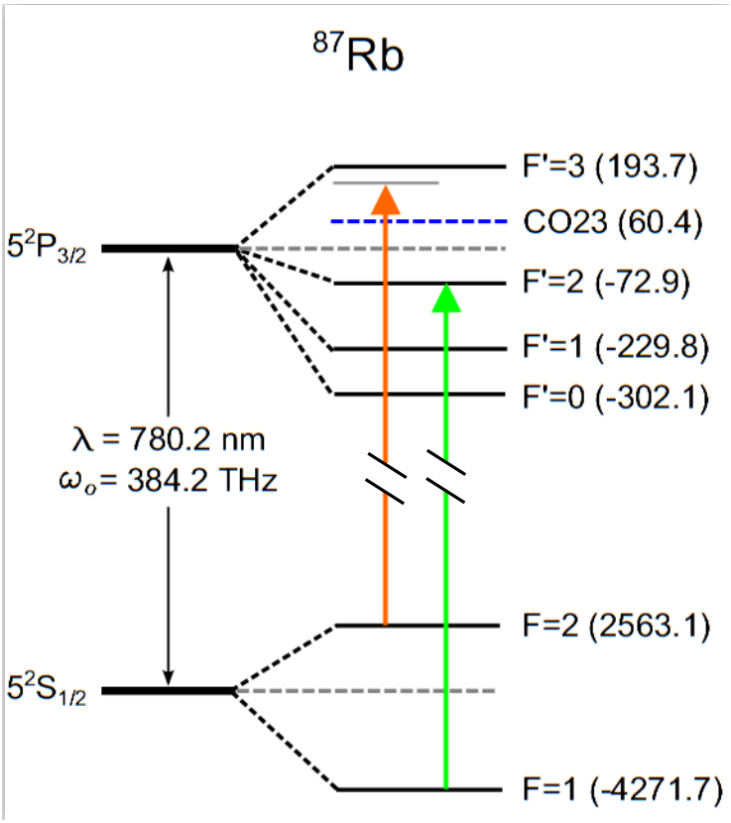


Figure 2.1: Excitation scheme of the ^{87}Rb atom

Due to the hyperfine splitting is insufficiently large, the red detuning cooling light can also pump an unwanted atomic transition $|F = 2 > \rightarrow |F' = 2 >$ that causes a finite probability for the system to spontaneously decay to a dark state, $|F = 1 >$, and fall out of the cooling cycle. To avoid these losses, an additional laser to pump the atoms back into the cooling cycle, corresponding to the atomic transition $|F = 1 > \rightarrow |F' = 2 >$, is required which is referred to as repumping light.

2.1.3 Sub-Doppler cooling after MOT

The Doppler temperature for ^{87}Rb,^{39}K and ^{41}K atoms are 146 μK, 145μK and 145μK, respectively [30, 31]. However, even the first experiments measured the temperature of the MOT to be far below these values. This is because in a real MOT there exist polarisation

gradients, providing a position-dependent light shift of the ground states. This makes a sub-Doppler cooling possible [32] as shown in Fig. 2.2. When the atom moves in a pair of counter-propagating beams with the $Lin \perp Lin$ configuration, the light shifts of the ground sub-Zeeman states $|g+\frac{1}{2}\rangle$ and $|g-\frac{1}{2}\rangle$ are functions of the position in the z-direction. (The $Lin \perp Lin$ configuration indicates the polarizations of the two counter-propagation beams are linear and perpendicular to each other.)

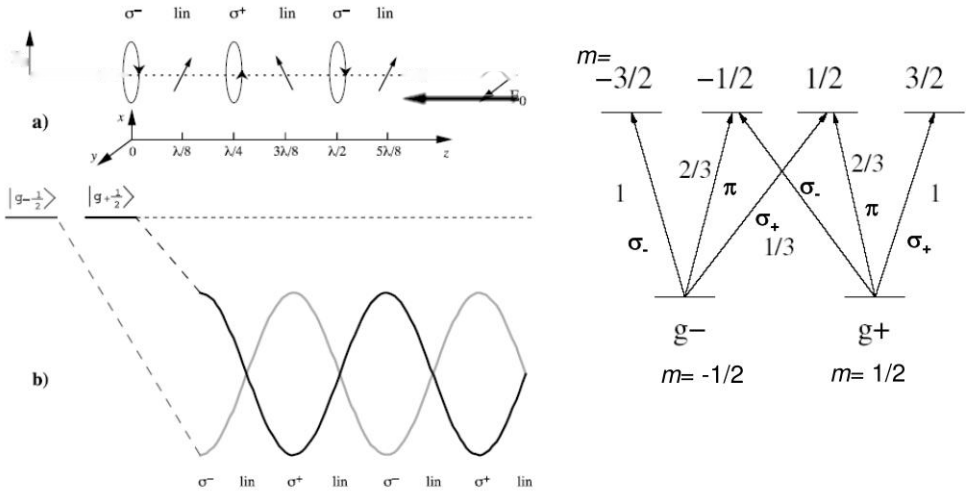


Figure 2.2: Schematic of the confining potential in one direction of a MOT. The ω_0 is the frequency of the atomic transition, the ω_{light} is the frequency of the laser, it is red detuned with respect to the atomic transition. The Zeeman splitting is linear expanded by a magnetic gradient along the z direction. Figure and caption taken from Ref [32].

The atomic transfer between different ground Zeeman states takes a finite time τ_P. If we assume the atom occupies the ground Zeeman state $|g-\frac{1}{2}\rangle$ and moves from the left to right with the beginning point at bottom of the potential valley $\lambda/8$, when the atom moves over the point $3\lambda/8$ and still stays in the initial state, the kinetic energy of the atom can be transferred to potential energy by climbing the potential hill. This energy transfer will continually be repeated unless the velocity of the atom is below $\frac{\lambda}{4\cdot\tau_P}$, where τ_p is the optical-pumping time. (This is because, if the velocity of atom is higher than $\frac{\lambda}{4\cdot\tau_P}$, the atom is on average in the same sub-level that allows the atom climbs the potential hill and reaches the top of the hill before being optically pumped to the other sub-level.)

To correspond this velocity limit to a temperature, the recoil temperatures are 0.349μK, 0.418μK and 0.414μK for ^{87}Rb, ^{39}K and ^{41}K atoms.

For the $\sigma^+ - \sigma^-$ configuration, the light shifts of different ground Zeeman states are not position-dependent. The polarisation is linearly rotated in the z-direction (as shown in Fig. 2.2 (b)) and the Sisyphus cooling mechanism is invalid in this case. However, the motion-induced population imbalance can cause different radiation forces for the ground Zeeman states. This effect equivalently contributes to sub-Doppler cooling. The achievable limit of these further cooling is usually around 15 times the recoil temperature.

In another perspective, a higher density of the atom cloud can also enhance the phase space density (PSD). In the MOT, the main frustration on the atom compression is the repulsive force between the atoms from the re-absorption of the scattered photons. This in turn means to accumulate the atoms in a dark state can allow a higher PSD of atoms. As a background, a series of "dark state" schemes have been proposed and implemented in the experiments, such as free space Raman cooling [33], grey molasses [34] and dark spot MOT [35]. In our experiment, a dark MOT of ^{87}Rb atoms is implemented by reducing the intensity of the repumping laser and increasing the detuning of the cooling laser [36], where the PSD can be increased from 1×10^{-8} to 3×10^{-6}. These efforts on the ^{39}K and ^{41}K atoms have been also made. (In the initial cooling of ^{39}K and ^{41}K atoms, we set the detuning of the cooling and repumping light both larger than whole excited manifolds and then compressed the atom cloud through compressed MOT technique.)

The sub-Doppler cooling is efficient only if the hyperfine splitting Δ is much larger than the natural linewidth Γ and an inhibition can be observed when $\Delta \sim \Gamma$ by the heating force and photon re-absorption. The excited hyperfine splittings are 3.5Γ and 2.2Γ for ^{39}K and ^{41}K, respectively. The sub-Doppler cooling efficiency is moderate with implementing a normal optical molasses and it can be enhanced by employing an appropriate tuning of frequency and power of the cooling laser [37].

2.2 Dipole trapping and creation of BEC

2.2.1 Optical dipole trap

Trapping atom cloud in an optical potential gradient has been achieved as early as 1970 by Arthur Ashkin [38], where the trapping force is produced from the interaction between the induced electric dipole of an atom and the far detuned laser field [39–41]. Unlike in a MOT, this force is not dissipative. It scales as the gradient of the potential μ, $F = -\nabla\mu$. On the other hand, the cooling of atoms in the optical dipole trap can be also achieved by allowing the hottest atoms to escape from the trap and rethermalizing the remaining atoms. This is referred to as optical evaporative cooling.

The optical potential is given by [42]

$$U(r) = \frac{\pi c^2 \Gamma}{2}\left(\frac{2 + P g_F m_F}{\Delta_{2,F}\omega_2^3} + \frac{1 - P g_F m_F}{\Delta_{1,F}\omega_1^3}\right) I(r) \tag{2.3}$$

where ω_1, ω_2 are the frequencies of the D_1 and D_2 lines of the atomic transitions, $\Delta_{1,F}$, $\Delta_{2,F}$ are the detunings of the laser beam with respect to the atomic transitions to the $P_{1/2}$ and $P_{3/2}$ states and P is the polarisation of the laser beam (P=0 for the linear polarisation and P=$\pm$1 for the $\sigma^{\pm}$ polarisation). The dipole potential scales as the intensity of the laser and has a maximum (minimum) when the detuning of the laser is positive (negative). This equation can be also used to explain the phase imprinting on a BEC by the spatial light modulator (SLM) [43]. The details of its use in an atomic interferometer will be discussed in the later chapter.

For a propagating laser field, the optical density is ruled by a spatial Gaussian distribution,

$$I(r) = \frac{2P}{\pi w^2(x)} e^{-\frac{2\rho^2}{w^2(x)}} \tag{2.4}$$

where ρ^2=$y^2 + z^2$, $w(x)$=$w_0(1 + x^2/x_r^2)^{1/2}$ is the $1/e^2$ radius, w_0 is the beam waist, $x_r = \pi w_0^2/\lambda$ is the Rayleigh length and P is the laser power. The trapping potential can

be approximated as a harmonic oscillator with cylindrical symmetry

$$U(\rho, x) = U(0)[1 - 2(\frac{\rho}{w_0})^2 - (\frac{x}{x_r})^2] \tag{2.5}$$

The oscillation frequencies of a trapped atom in the transverse directions and in the propagating direction can be estimated as $\omega_\rho = \sqrt{4U(0)/mw_0^2}$ and $\omega_x = \sqrt{2U(0)/mx_r^2}$, respectively. The ratio of their trapping frequencies is

$$\frac{\omega_\rho}{\omega_z} = \sqrt{2}\frac{w_0\pi}{\lambda} \tag{2.6}$$

Meanwhile, the laser field can be also scattered by the polarised atoms, the scattering rate is

$$\Gamma_{sc} = \frac{\pi c^2 \Gamma^2}{2\hbar}\left(\frac{2 + Pg_F m_F}{\Delta_{2,F}^2 \omega_2^3} + \frac{1 - Pg_F m_F}{\Delta_{1,F}^2 \omega_1^3}\right) I(r) \tag{2.7}$$

In a conclusion, since the scattering rate and the trapping potential are inversely proportional to Δ^2 and Δ, a far detuned laser with a strong power can provide a sufficiently strong trapping force without bringing a remarkable heating effect. Our experimental layout will be discussed in the later chapter.

2.2.2 Thermodynamics and characterization of BEC

A dramatic increase of the PSD by several orders of magnitude after the dark MOT is required for producing a BEC, which can be achieved by evaporative cooling. The thermodynamics of the atoms in a dipole trap is determined by the external potential and the inter-particle interaction. When the trapping potential slowly decreases, the atoms with more kinetic energy are easier to escape from the trap meanwhile the remaining atoms can be rethermalized to a colder temperature. The evaporative cooling depends on two scattering processes: (1) the inter-atoms collision (2) the collision between atoms and the background. Where the background collision leads to losses of atoms and the heating effect, the elastic collision contributes to the rethermalization. [44]. In the microscopic

picture, the total atom number can be depicted as

$$N = \sum_i N_i = \sum_i \frac{ze^{-\beta\epsilon_i}}{1 - ze^{-\beta\epsilon_i}} \tag{2.8}$$

where i symbolizes the ith energy level ϵ_i, N_i is the occupation number of the atoms in level ϵ_i. The number of atoms with energy ϵ is

$$f_0 = \frac{1}{ze^{-\beta\epsilon} - 1} \tag{2.9}$$

$\beta = \frac{1}{\kappa_B T}$ where κ_B is the Boltzmann constant and $z = e^{\beta\mu}$ is the fugacity, μ is the chemical potential, which can be defined as

$$\mu = (\frac{dU}{dN})_{S,V} \tag{2.10}$$

where U is the energy of the system, S is the entropy and V is the volume. The chemical potential can be explained as the energy that one needs to add an atom to a given state. We assume the sphere volume $4\pi p^3/3$ includes all the states with momentum less than p and the kinetic energy is $\epsilon = p^2/2m$. The total number of the state in volume V is

$$G(\epsilon) = V\frac{4\pi p^3}{3h^3} = V\frac{2^{1/2}}{3\pi^2}\frac{(m\epsilon)^{3/2}}{\hbar^3} \tag{2.11}$$

The density of the state as a function of the energy can be obtained by,

$$g(\epsilon) = \frac{dG(\epsilon)}{d\epsilon} = \frac{Vm^{3/2}}{2^{1/2}\pi^2\hbar^3}\epsilon^{1/2} \tag{2.12}$$

An atom in an optical dipole trap approximately behaves as a particle in a harmonic potential U,

$$U(r) = \frac{1}{2}m(\omega_1^2 x^2 + \omega_2^2 y^2 + \omega_3^2 z^2) \tag{2.13}$$

where $\omega_1, \omega_2, \omega_3$ are the harmonic oscillation frequencies. The energy level of the system is,

$$\epsilon(n_1, n_2, n_3) = (n_1 + \frac{1}{2})\hbar\omega_1 + (n_2 + \frac{1}{2})\hbar\omega_2 + (n_3 + \frac{1}{2})\hbar\omega_3 \tag{2.14}$$

Ignoring the ground state and assuming that the quantum state is continuum, the number of the state can be deduced by,

$$G(\epsilon) = \frac{1}{\hbar^3\omega_1\omega_2\omega_3}\int_0^{\epsilon_1} d\epsilon_1 \int_0^{\epsilon-\epsilon_1} d\epsilon_2 \int_0^{\epsilon-\epsilon_1-\epsilon_2} d\epsilon_3 = \frac{\epsilon^3}{6\hbar^3\omega_1\omega_2\omega_3} \tag{2.15}$$

where $\epsilon = \epsilon_1 + \epsilon_2 + \epsilon_3$. The density of the state is,

$$g(\epsilon) = \frac{G(\epsilon)}{d\epsilon} = \frac{\epsilon^2}{2\hbar^3\bar{\omega}^3} \tag{2.16}$$

where $\bar{\omega} = (\omega_1\omega_2\omega_3)^{1/3}$. In an excited state, the atom number N_{ex} can be deduced from,

$$N_{ex} = \int_0^{\infty} d\epsilon g(\epsilon) f_0(\epsilon) \tag{2.17}$$

When the atoms transit into BEC, the ground state can be occupied by a macroscopic amount of atoms, if assuming the energy cost for this transition is 0, $\mu = 0$, its temperature can be deduced by,

$$N = N_{ex}(T_c, \mu = 0) = \int_0^{\infty} d\epsilon g(\epsilon) \frac{1}{e^{\epsilon/k_B T_c} - 1} \tag{2.18}$$

T_c is referred to as critical temperature. In the harmonic trap, using the Eq. 2.16 the critical temperature is,

$$T_c = \frac{\hbar\bar{\omega}N^{1/3}}{\zeta(3)^{1/3}k_B} = \frac{0.94\hbar\bar{\omega}N^{1/3}}{k_B} \tag{2.19}$$

To re-express the interaction between atoms and the external potential in the second

quantization language, the Hamiltonian of the system is

$$\hat{H} = \int d\vec{x}\hat{\Psi}^{+}(\vec{x})(-\frac{\hbar^2\nabla^2}{2m}+U_{ext}\hat{\Psi}(\vec{x}))+\frac{1}{2}\int d\vec{x}d\vec{x'}\hat{\Psi}^{+}(\vec{x})\hat{\Psi}^{+}(\vec{x'})V(\vec{x}-\vec{x'})\hat{\Psi}(\vec{x'})\hat{\Psi}(\vec{x}) \quad (2.20)$$

where U_{ext} is the external trapping potential and $V(\vec{x}-\vec{x'})$ is the interaction between the atoms. In the low collision energy limit, $V(\vec{x}-\vec{x'})$ reduces to contact potential $V(\vec{x}-\vec{x'}) = g\delta(\vec{x}-\vec{x'})$, where $g = \frac{4\pi\hbar^2 a}{m}$ and α is the s-wave scattering length.

The Bosonic field can be treated as a classical field in the mean-field approximation, the Eq. 2.20 is replaced by

$$i\hbar\partial_t\phi(\vec{x},t) = (-\frac{\hbar^2\nabla^2}{2m} + U(\vec{x}) + \hbar g|\phi(\vec{x},t)|^2)\phi(\vec{x},t) \quad (2.21)$$

which is the so-called Gross-Pitaevskii equation. The energy eigenvalue can be diagonalized by

$$H = \int d^3\vec{x}[\phi^{+}(\vec{x})(-\frac{\hbar^2\nabla^2}{2m} + U(\vec{x}))\phi(\vec{x}) + \frac{\hbar g}{2}|\phi(\vec{x})|^4] \quad (2.22)$$

The s-wave scattering description is valid for a dilute atom gas at a low temperature, in which the interaction between atoms is a spin-dependent contact interaction. According to the rotational symmetry of spin, for a spin-1 BEC, the two-body interaction through s-wave scattering channels F=0,2 is allowed in this model. The interaction term in the Hamiltonian can be written as

$$V_{int} = \delta(\vec{x_1}-\vec{x_2})\sum_{F=0,2} g_F P_F \quad (2.23)$$

where P_F is the projector of the total momentum. Transform the V_{int} into the individual spin basis [45]

$$V_{int} = \delta(\vec{x_1}-\vec{x_2})(c_0 + c_2\vec{f_1}\cdot\vec{f_2}) \quad (2.24)$$

where

$$\begin{aligned} c_0 &= \frac{4\pi\hbar^2}{m}\frac{a_0+2a_2}{3} \\ c_2 &= \frac{4\pi\hbar^2}{m}\frac{a_2-a_0}{3} \end{aligned} \tag{2.25}$$

with a_0,a_2 being the s-wave scattering length with total spin F=0,2. The Hamiltonian of the system is

$$\begin{aligned} &\hat{H} = \int d\vec{x}\left(\sum_{i,j}\hat{\Psi}_i{}^{+}(-\frac{\hbar^2\nabla^2}{2m}+U_{ext}(\vec{x}))\hat{\Psi}_j + \frac{c_0}{2}\hat{\Psi}_i{}^{+}\hat{\Psi}_j{}^{+}\hat{\Psi}_i\hat{\Psi}_j\right. \\ &\left.+\frac{c_2}{2}\sum_{a,i,j,k,l}(f_a)_{i,j}(f_a)_{k,l}\hat{\Psi}_i{}^{+}\hat{\Psi}_k{}^{+}\hat{\Psi}_l\hat{\Psi}_j\right) \end{aligned} \tag{2.26}$$

where the subscripts i,j,k,l=$0,\pm1$. From this equation, several different phases of the ground state can be diagrammed in a variable amount of scattering lengths. If $c_2 < 0$, the energy of the system reaches the minimum when the spin-dependent term (the last term in Eq. 4.1) is at its maximum value, thus it facilitates the spins of the ground states to be aligned to the same direction. It has been confirmed in the case of ^{87}Rb [46–48]. In the opposite, if $c_2 > 0$ the system favors the anti-ferromagnetic configuration.

The proportion of the condensed component in an ultracold gas is referred to as BEC fraction [49]. The BEC fraction as a function of the temperature in equilibrium can be illustrated as:

$$F = 1 - \left(\frac{T}{T_c}\right)^3 = 1 - (\tau)^3 \tag{2.27}$$

Where τ is the reduced temperature and the critical temperature can be deduced from the Eq. 2.19. During the evaporative cooling, not only the temperature can be reduced by the rethermalization but also the critical temperature can be reshaped by the dissipative losses of atoms that in turn means these losses of atoms (It is usually the two-body losses, however in the high-density case, the system is also suffered by three-body losses), can drive the atoms in the optical dipole trap in non-equilibrium. If the dissipation is mild, the equilibrium can be still a good approximation. However, in our experiment, the collision with the surrounding ^{39}K atoms can bring an unneglectable

dissipation rate of the ultracold ^{87}Rb atoms. Surprisingly, we found that this dissipation does not act a detrimental role in the evaporative cooling and the collective properties of the system, but favors to produce a long-lived metastable state of the ultracold ^{87}Rb atoms in non-equilibrium.

Besides, some intrinsic characteristics of the BEC have been observed, such as its inversion of the aspect ratio which is exhibited in its absorption imaging detection with a variable amount of TOF time, as shown in Fig.2.3

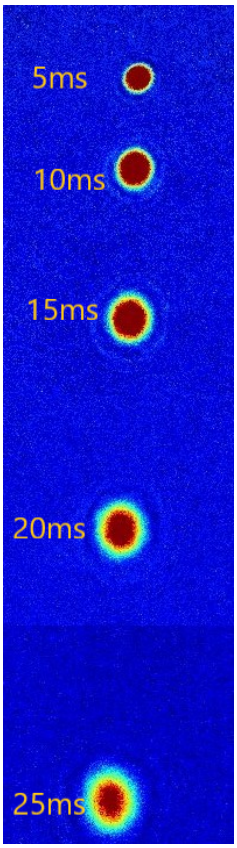


Figure 2.3: Observation of BEC with different expansion time.

The expansion time is 5 ms, 10 ms, 15 ms, 20 ms, and 25 ms, respectively. The BEC falls from the centre to the bottom edge of the glass cell due to gravity. The aspect ratio (vertical width: horizontal width) of the BEC is changed from 0.9:1 to 4:3 within 5 ms to 25 ms expansion.

2.3 Quantum heat engines

2.3.1 Single atom heat engine

One of our research goals is to achieve the thermodynamics cycle in quantum regime. A single neutral atom trapped in an optical tweezer at a low temperature is considered as a good candidate to explore the heat engines in the quantum thermodynamics framework. Specifically, we aim to engineer a novel experimental setup to trap the single neutral atom in an optical tweezer and immerse it in an ultracold atom cloud, where the single atom and the ultracold atom cloud act as the working fluid and the thermal bath, respectively. Our experimental realisation is still under construction. In the recent future, we expect to achieve the thermodynamics transformations, the quantum adiabatic transformation, the quantum isothermal transformation, the quantum isochoric transformation, and the quantum isobaric transformation. After that, the quantum thermodynamics cycle, including multiple strokes, such as quantum Carnot, Otto, and Diesel cycles is expected to be machined as well.

The Hamiltonian of a single atom in the low lying states in a one-dimensional harmonic trap can be written as $H = \sum_n E_n |n><n|$ where E_n and $|n>$ are the eigen-energy and eigen-vector of the oscillator. The total energy is

$$U = \sum_n P_n E_n \tag{2.28}$$

where P_n is the occupation probability. To differentiate the Eq. 2.28,

$$dU = \sum_n P_n dE_n + E_n dP_n \tag{2.29}$$

this is similar to the classical first law of thermodynamics $dU = dQ + dW$. The von Neumann entropy is

$$S = -k_B Tr(\rho \cdot log\rho) \tag{2.30}$$

where ρ is the density matrix of the system. In our case, the thermal entropy can be deduced as,

$$S = -k_B \sum_n P_n ln P_n \tag{2.31}$$

to differentiate the Eq. 2.31, due to $\sum_n dP_n = 0$

$$dS = \sum_n \frac{E_n}{T} dP_n \implies dQ = TdS = \sum_n E_n dP_n \tag{2.32}$$

the total energy change denoted in Eq. 2.29 is the sum of the heat exchange dQ and the work exchange $dW = \sum_n P_n dE_n$. The quantum pressure is calculated out by $\Pi = -dW/dV$ where V is the trapping volume. With these redefined thermodynamics parameters, four quantum thermodynamics transformations can be plotted:

(1) the quantum adiabatic transformation in which the thermal entropy is preserved, the heat exchange is forbidden $dQ = 0$.

(2) the quantum isothermal transformation, in which the temperature is preserved. This requires a constant trapping potential for the thermal bath when the heat exchange channel is open and the optical tweezer is compressed or decompressed. The working fluid exchanges heat with the thermal bath during the compression or expansion of the energy levels at a constant temperature.

(3) the quantum isochoric transformation, in which the volume of the quantum levels is preserved, the work exchange is zero $dE_n = 0$. The heat exchange channel is open when the thermal bath temperature is changed by tuning the trapping potential of the ^{87}Rb BEC. This leads to $dp_n \neq 0$ and $dS \neq 0$.

(4) the quantum isobaric transformation, which requires the quantum pressure is preserved, $d\Pi = 0$. The heat exchange channel is open while the trapping potential of the optical tweezer and the thermal bath temperature are cooperatively changed. The pressure can be calculated as $\Pi = \sum_n P_n (dE_n/da_{ho})$, where $a_{ho} = \sqrt{\hbar/m\omega}$ is the length of the harmonic oscillator, yielding $\Pi = \frac{\sqrt{\epsilon} sinh\beta}{cosh\beta - 1}$ where $\epsilon = hm\omega^3$ and $\beta = \hbar\omega/(k_B T)$. The

temperature should be accorded to

$$\frac{\hbar\omega}{k_B T} = ln(\frac{\Pi + \sqrt{\epsilon}}{\Pi - \sqrt{\epsilon}}) \tag{2.33}$$

Combined with these quantum thermodynamics transformations into a cycle, we can perform different quantum engines, as shown in Fig. 2.4

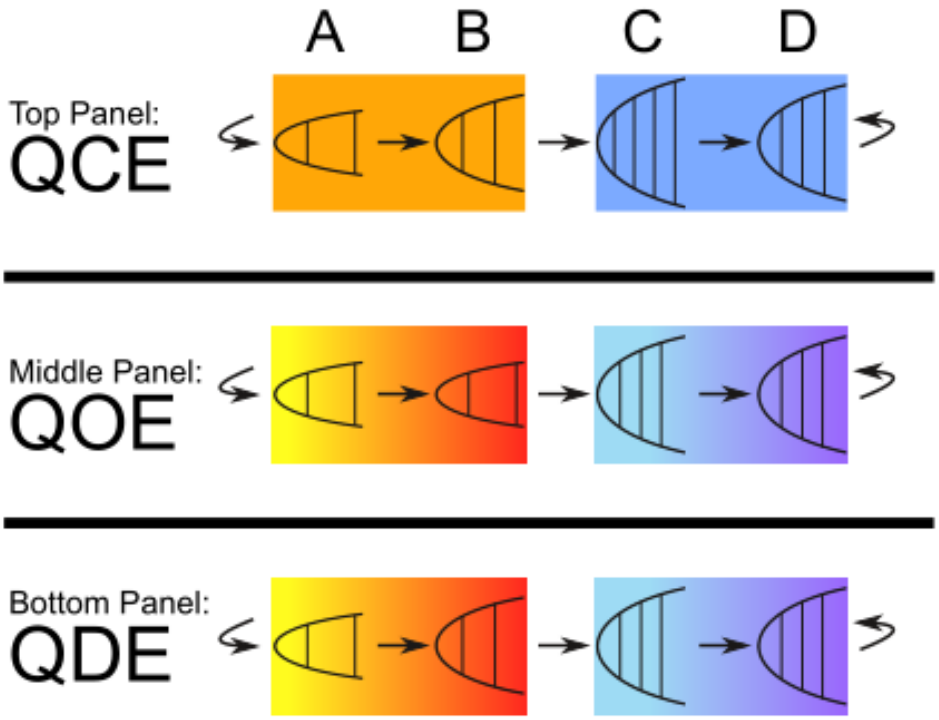


Figure 2.4: From top to bottom: the schemes of the Quantum Carnot Engine (QCE), the Quantum Otto Engine (QOE), and the Quantum Diesel engine (QDE) realising in an ultracold single atom. The frequency of the harmonic confinement of the working fluid is changed in time in order to realise the compression or expansion on the single atom. The background colors (red→blue) indicate the temperature of the bath is changed from hot to cold. The (B → C) and (D → A) transformations are realised by decoupling the working fluid and the bath. Figure and caption taken from Ref [50].

Take the quantum Carnot engine as an example, it includes four strokes: (1) a quantum isothermal expansion at a hot temperature T_1, the working fluid absorbs heat from the thermal bath (A → B). (2) a quantum adiabatic expansion, the work is extracted from

the working fluid (B $\rightarrow$ C). (3) a quantum isothermal compression at a cold temperature T_2, the thermal bath obtains the heat from the working fluid (C $\rightarrow$ D). (4) a quantum adiabatic compression, the work has been applied on the working fluid (D $\rightarrow$ A). This cycle requires $T_1/T_2 = \hbar\omega_B/\hbar\omega_C = \hbar\omega_A/\hbar\omega_D$.

Our dual-species mixture system is the quantum counterpart of a system of the classical working fluid in a thermal bath. We expect the sympathetic cooling of ^{41}K atom can be achieved in the further experiment to maintain the single atom at a cold temperature and in quantum regime. In practice, the trapping frequency of the ^{41}K atom in the optical tweezer is determined by the geometric property and the wavelength of the laser, it can be properly tailored to be much lower in the axial direction than the radial directions. If so, the system can be considered as a one-dimensional harmonic oscillator and its operating temperature is determined by the 1D quantum states. The compression on the working fluid and the heat exchange between the working fluid and the thermal bath can be engineered by controlling the tweezer power and the inter-species interaction. On the other hand, the temperature of the thermal bath is controlled by the trapping potential of the optical dipole trap of ^{87}Rb atoms. The interference on the single ^{41}K atom from the dipole trap can be ignored since the trap beam's waist and frequency are much larger and further detuned than the tweezer light, .

2.3.2 Single atom in an optical tweezer

2.3.2.1 Species selective optical tweezer

Trapping a single neutral atom at a cold temperature is challenging. To date, with spatial modulation of the laser power density, single atoms can be trapped in 2D [51] or 3D [52] arrays. In another work, the light-induced collision can be employed to near-deterministically prepare a single atom in an optical tweezer [53]. Ideally, this method can provide a 50 % chance to observe only a single atom in an optical dipole trap, depending on whether odd or even atom number at the beginning [24]. In our experiment, after the pre-cooling of the ^{41}K and ^{87}Rb atoms, the ^{87}Rb atoms are transferred into a crossed

optical dipole trap while the ^{41}K atoms is confined by a species-selective optical tweezer [54]. The trapping potential of the optical tweezer as a function of laser wavelength for the ^{87}Rb and ^{41}K atoms is plotted in Fig. 2.5.

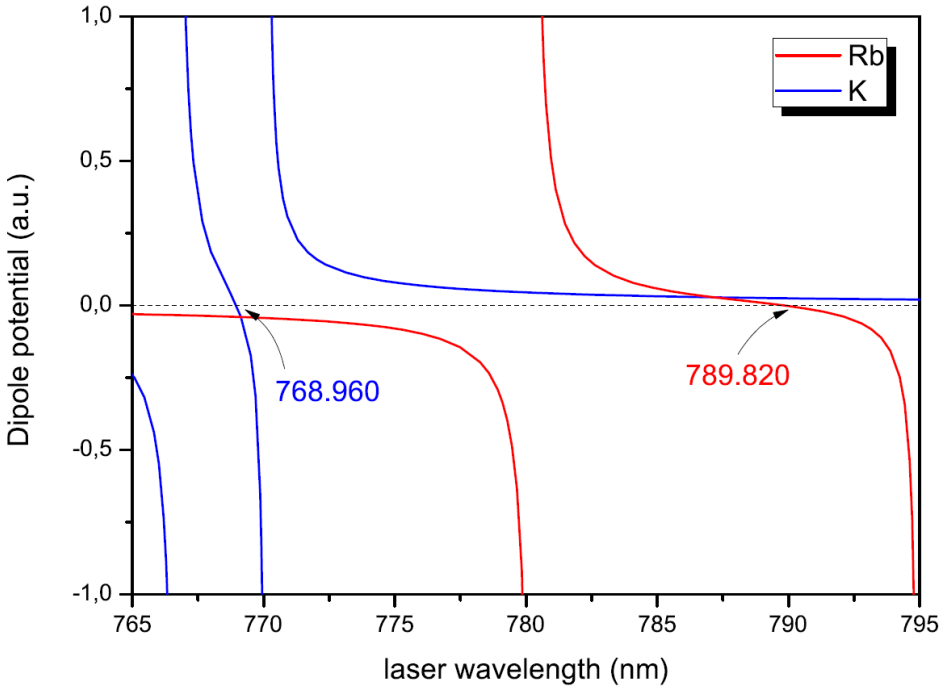


Figure 2.5: Choice of the wavelength of the species-selective optical tweezer: the behaviour of the dipole potential as a function of the wavelength for both Rb and K atoms. The magic wavelengths at which have zero dipole potential have already shown in the diagram. Figure and caption taken from Ref [55].

In our mixture system, trapping a single ^{41}K atom should avoid the interference on the ^{87}Rb atoms at the same time, the wavelength of the tweezer light is therefore selected at a magic wavelength, 789.82 nm, that allows the beam to be transparent with respect to the ^{87}Rb atoms.

2.3.2.2 Trapping potential and heating rate of the optical tweezer

Specifically, the tweezer light at the magic wavelength with a power 25 mW and a beam waist 2 μm can provide the trapping frequency (f_x, f_y, f_z)=(15.7,153,152) kHz for ^{41}K atom, where the x-direction is the propagation direction. The heating effects are mainly

from the spontaneous photon scattering of the tweezer light, that is detrimental for trapping atom at a cold temperature and it can be estimated as

$$E_{rec} = k_B T_{rec}/2 \tag{2.34}$$

per each scattering event, where T_{rec} is the recoil temperature. Assuming the atoms are in thermal equilibrium, the mean energy of the atom is

$$\bar{E} = \frac{2}{3}(1+\kappa)k_B T \tag{2.35}$$

where κ is the ratio of potential and kinetic energy, for a 3D harmonic trap $\kappa = 1$. The increasing rate of temperature is

$$\dot{T} = \frac{2}{3} T_{rec} \bar{\Gamma}_{sc} \tag{2.36}$$

where $\bar{\Gamma}_{sc}$ is the mean photon scattering rate, that can be calculated by Eq. 2.7. As a result, the heating rate in our case is 132 $\mu K/s$ and 664 $\mu K/s$ for the ^{41}K and ^{87}Rb atoms, respectively.

2.3.2.3 Collisional blockade

In contrast to the optical dipole trap used for BEC creation, our optical tweezer is designed to trap a single atom. The mechanism for maintaining few atoms even a single atom in the tweezer has been discussed in [53, 56], which is based on a variety of inelastic collision mechanisms as shown in the following equation,

$$\frac{dN}{dt} = R - \gamma N - \beta' N(N-1) \tag{2.37}$$

where R is the atom loading rate, γ is the one-body decay rate from the collision with the background and β' is the two-body decay rate which inversely proportional to the trap volume V,

$$V = \pi w_0^2 z_R ln(\frac{1}{1-\eta})\sqrt{\frac{\eta}{1-\eta}} \tag{2.38}$$

with w_0 and z_R being the tweezer beam waist and the Rayleigh length. $\eta = k_B T/U_0$, where U_0 is the potential depth. Due to the dependence of the two-body decay on the tweezer waist, suppression of the tweezer loading is predicted in the presence of a small beam waist, as shown in Fig. 2.6

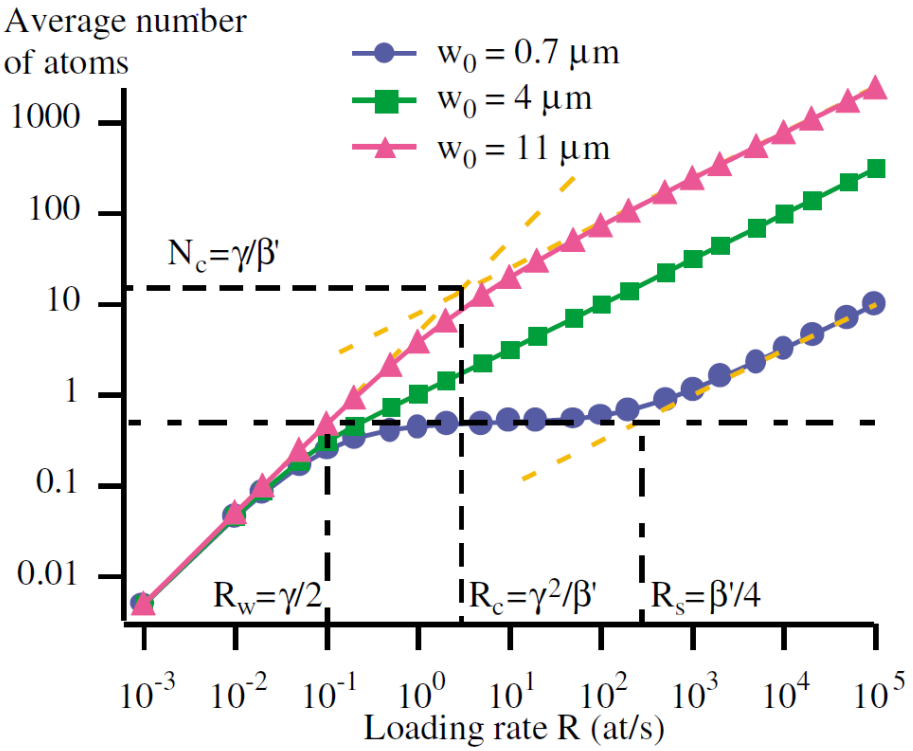


Figure 2.6: Average number of atoms in the optical tweezer as a function of loading rate R for different waists. Figure and caption taken from Ref [53].

The plateau around 0.5 atom is observed when the waist is 0.7 μm, which strongly indicates a blockade mechanism or the single atom regime.

2.3.3 Feshbach resonance

The property of the inter-atom interaction is sensitive to the average separation of the atoms R, which can be described in a two potential channels system, the background

channel and the closed channel, as shown in Fig. 2.7 [57].

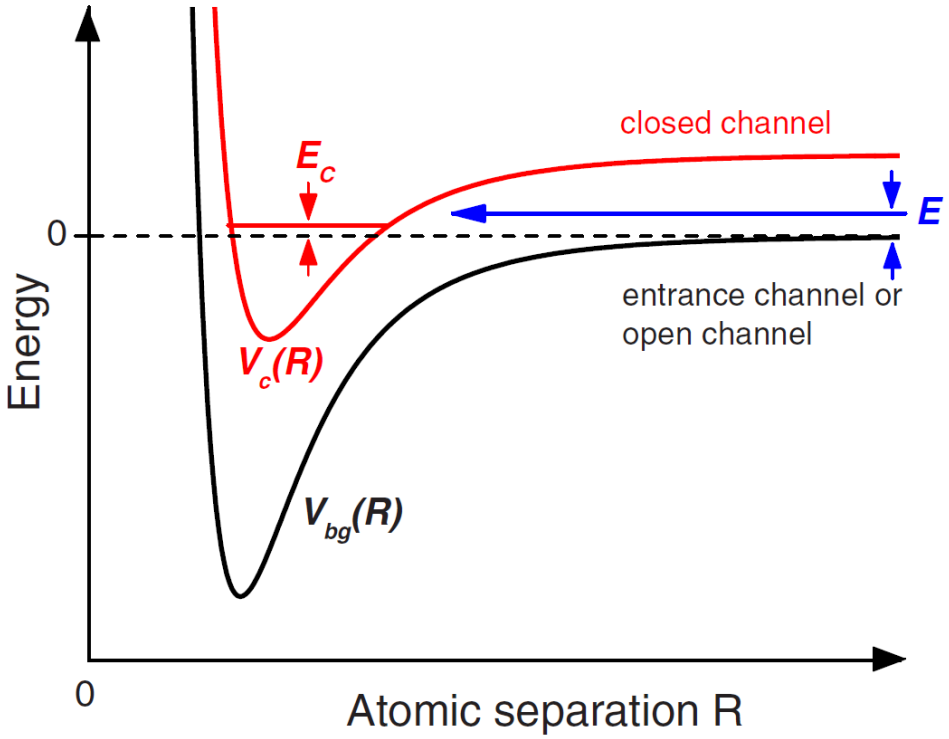


Figure 2.7: Basic two-channel model for a Feshbach resonance. Figure and caption taken from Ref [57].

For a large inter-atom distance, the background potential asymptotically approaches zero. For a small distance, the collision process dominates the dynamics, bringing a small energy potential, which is referred to as open channel. The molecular bound state in the closed channel $V_c(R)$ can be energetically degenerate to the scattering state in the open channel as a strong mixing between the two channels can be induced. The energy levels in the closed channel can be shifted into the open channel by applying a magnetic field and become a metastable molecular state, that alters the property of the collision. In S-wave scattering approximation, it can be simply explained as [58],

$$\alpha(B) = \alpha_{bg}(1 - \frac{\Delta}{B - B_0}) \tag{2.39}$$

where α_{bg} is the background scattering length, B_0 indicates the magnetic field when the resonance appears and Δ is the resonance width. This method is used to control the

inter-atom interaction in our experiment.

In specific, due to the inter-species interaction is sensitive to the Zeeman sub-levels, we select the isotopes ^{41}K $|1,1\rangle$ and ^{87} Rb $|1,1\rangle$, which has been shown in Fig. 2.8

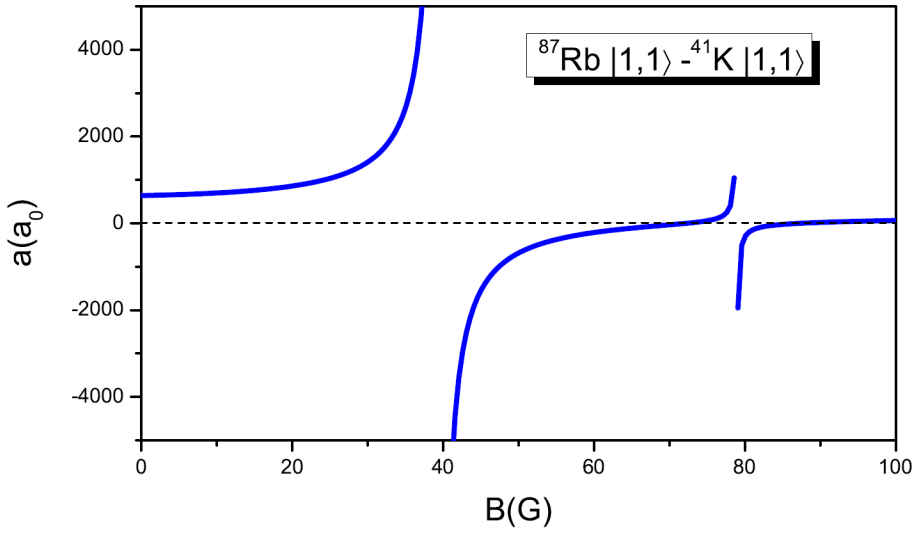


Figure 2.8: Theoretical calculation of the inter-species scattering length as function of the magnetic field for the ^{41}K-^{87}Rb mixture in the |1,1> state. Figure and caption taken from Ref [55].

Feshbach field at 75G can provide a 0 inter-atom interaction.

Chapter 3

Experimental apparatus

In this section, I will present the experimental setup in detail. The main blocks of our experimental system include the vacuum system, the laser system, the computer-based control system, and the detection system. The vacuum system consists of two vacuum chambers with different background pressures, one is used for the 2D MOT and the other is used for the 3D MOT and the evaporative cooling [59]. They are connected through a differential pumping stage, 2 cm long tube with a 1 mm diameter hole. A laser beam, which is referred to as push beam, delivers the atoms from the 2D MOT chamber into the 3D MOT chamber for further cooling. The 3D MOT chamber is the place where all the experiments described in this thesis take place, it is therefore also referred to as science chamber. In both chambers, pairs of counter-propagating beams can produce a viscous-like force and a position-dependent force exerting on the atoms in the presence of anti-Helmholtz coils, that confines the atoms and reduces the temperature of the atoms to a temperature near the Doppler limit. This process is referred to as MOT cooling. After MOT cooling, the sub-Doppler cooling can be implemented to break the Doppler limit in the following dark MOT and molasses stages. This makes it possible to load a sufficient number of atoms into an optical dipole trap. Eventually, adiabatically reducing the laser power of the dipole trap beams in the absence of magnetic field, when the temperature of atoms is reduced below the critical temperature, a BEC can be produced. To collect the

experimental data, the optical diagnose measurement has been used in our experiment after a ballistic expansion of the atom cloud. Through the data acquirement and analysis, our experimental results can be systematically exhibited in a scientific paradigm. One should also note that the experiment needs to be controlled precisely by a computer-based system.

Additionally, for the investigation of a single-atom heat engine, an experimental setup to load a neutral single atom has been also discussed at the end of this section.

3.1 Vacuum system

The typical temperature of an ultracold atom cloud experiment is about 100 nK, which is more than 9 orders of magnitude lower than the room temperature (300K). For the ultracold atoms, this large temperature difference strengthens the collisions with the background that not only acts as the media of heat exchange but also induces the losses of atoms. To circumvent a dramatic heating effect and atom loss, an ultrahigh vacuum (UHV) for maintaining low background pressure is necessary. In our experiment, the vacuum is required to reach 10^{-11} mbar in the science chamber and 10^{-7} mbar in the 2D MOT chamber.

A high background pressure of the desired species brings a fast atom loading in 2D MOT and a low background pressure can dramatically reduce the background collision rate for ultracold atoms. Our vacuum system has been shown in Fig. 3.1

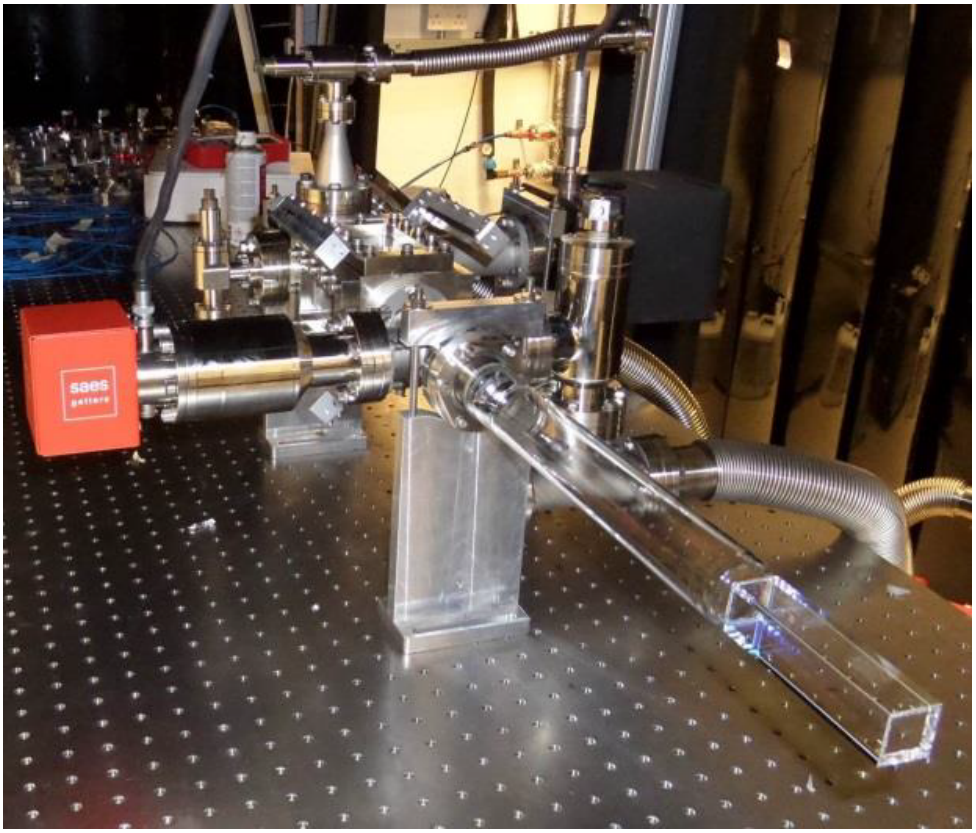


Figure 3.1: Picture of vacuum setup from side view.

The 2D MOT chamber dimensions are 12 cm× 9 cm × 9 cm. Four rectangular windows, 8 cm× 3.5 cm, are on the sides of the 2D MOT chamber which allow two perpendicular beams passing through the chamber and being retro-reflected by two prisms. This provides a compact design for achieving σ^+-σ^- configuration. At the back end of the 2D MOT chamber, an ion pump and a UHV valve are placed at two ends of a "T" through flanges. On the top end of the "T", another window allows a laser transferring the atoms into the science chamber through a differential pump stage, a metallic tube (length: 20 mm) with a hole (diameter: 1 mm), which maintains different pressures in the two chambers and collimates the atom flux. The chamber and the differential pump stage are made of titanium and the windows are made of BK7. Both materials have similar thermal expansion coefficients which are important during the baking. The windows are sealed by an epoxy glue 353ND with a low degassing rate [60], which has also been used successfully in a previous experiment [61].

The atom sources are ampules in flexible metallic tubes. Breaking the glass ampules after baking, the ^{87}Rb and ^{39}K or ^{41}K atoms can be delivered into the chamber. However, due to the conductance between the bellow and the chamber, the atomic density of ^{87}Rb is not sufficient. In additional, the degassing rate of the K atoms is lower at room temperature. Therefore, the tubes are required to be heated to 50^{o}C and 90^{o}C for the Rb and K atoms, respectively.

The science chamber on the other side of the differential pump stage is a glass cell in the size of 2.5 cm$\times$ 2.5 cm $\times$ 10 cm and is connected to the titanium chamber using a CF-40 flange. A NEXTorr-100D ion pump (SAES Getters), connected to the titanium chamber on the science chamber side, is used to pump the glass cell. Eventually, the pressures reach 10^{-7} mbar and $<10^{-11}$ mbar in the 2D MOT and the science chamber, respectively.

3.2 Laser system

The laser system designed for cooling and confining the ^{87}Rb and ^{39}K atoms or the ^{87}Rb and ^{41}K atoms comprises two colours of laser at wavelengths 780 nm and 767 nm. Due to the laser cooling depends on frequency detuning, power intensity and polarisation, several control techniques are applied in our experiment, such as the frequency locking system is used to generate a stable and tunable frequency detuning, the acousto-optic-modulators (AOMs) are used to control the power intensity, and etc.

The laser cooling is possible only if the linewidth of the laser is narrower than the linewidth of the atomic transition Γ. The linewidth of a bare diode is about 100 MHz that can be reduced in the presence of an external cavity. In our experiment, the external cavity diode lasers (ECDLs) are used in different types of equipment, two of them are commercial (New focus Vortex and DL Pro Toptica) and the other one is homemade as the design described in [62]. All of them can achieve a linewidth below 1 MHz, with being narrower than the natural linewidths of the ^{87}Rb 6.066 MHz and the ^{39}K or ^{41}K

6.035 MHz.

The frequency detuning of the laser with respect to the atomic transition is also critical in laser cooling. To prevent the frequency drift, the laser frequencies should be fixed to a reference signal which is usually produced from a spectroscopy cell. Then the error signal will be processed electronically to fed back into the piezo actuator for compensating the frequency drift. In our experiment, two individual frequency locking modules, the master locking, and the offset locking, are implemented for the ^{87}Rb atom, but for the ^{39}K and ^{41}K atoms, the offset locking module is not necessary, the frequency detunings can be set by AOMs. The homemade ECDL is used to produce the locking reference and the Vortex lasers act as the slave lasers in the ^{87}Rb setup. For the ^{39}K and ^{41}K atoms, the Toptica laser acts as the locking reference for both cooling and repumping lights. The laser locking modules are discussed in the supplement.

The excitation scheme of ^{87}Rb atom has been shown in Fig. 2.1, the frequency offsets for the cooling and repumping lights are set in the offset locking module and then in the AOMs,

$$\begin{aligned} \nu_{cooling} &= \nu_{crossover} + \nu_{offset-cooling} - \nu_{AOM} \\ \nu_{repumping} &= \nu_{crossover} + \nu_{offset-repumping} - \nu_{AOM} \end{aligned} \tag{3.1}$$

where ν_{AOM} is the frequency shift from the AOMs (160 MHz for a double pass), $\nu_{offset-cooling}$ = 293 MHz, and $\nu_{offset-repumping}$ = 6.861 GHz is the frequency shifts provided in the offset module, respectively.

The excitation scheme for ^{39}K and ^{41}K has been shown in Fig. 3.2

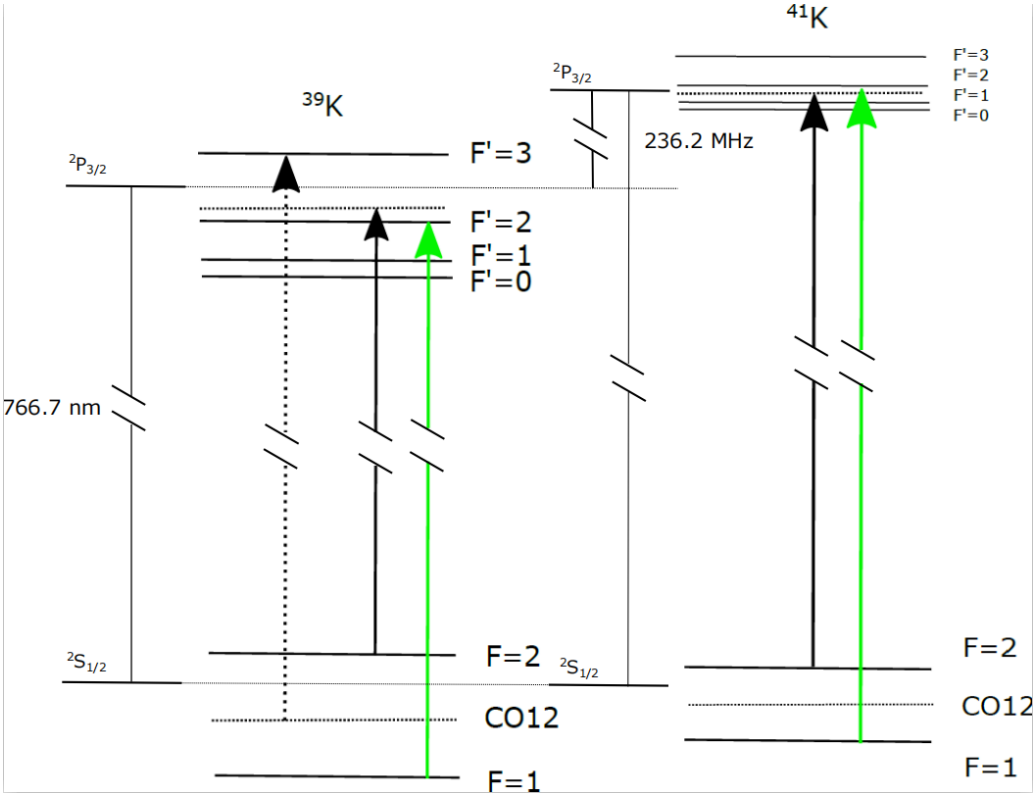


Figure 3.2: Excitation scheme of the ^{39}K and ^{41}K atoms. Where F and F' are the quantum numbers of the hyperfine ground states and the hyperfine excited states, the dashed lines represent the cross-over of the hyperfine ground states. The black (green) solid arrow is the cooling (repumping) transition. The dashed arrow is the locking frequency.

The excited-state hyperfine splittings are 3.5Γ and 2.2Γ for ^{39}K and ^{41}K atoms, respectively. The ground-state hperfine splittings are 77Γ and 42Γ for ^{39}K and ^{41}K atoms, respectively. The laser frequency is locked at the resonant frequency with respect to the D2 line transition of ^{39}K atom from the crossover of the two ground hyperfine states $|F = 1>, |F = 2>$ to the excited state $|F' = 3>$. The frequency offsets with respect to the locking frequency are $\nu_{AOM-cooling}$ =-231 MHz and $\nu_{AOM-repumping}$ = 210 MHz for ^{39}K, $\nu_{AOM-cooling}$ = 77 MHz and $\nu_{AOM-repumping}$ = 317 MHz for ^{41}K, respectively. Due to the nuclear magnetic moments of both isotopes are relatively small, the hyperfine splittings of the excited state are comparable to the natural linewidths, which leads to not only the atomic transition $|F = 2> \rightarrow |F' = 2>$ can be pumped as in the case of ^{87}Rb atoms, but

also this transition can bring a considerable heating effect. Furthermore, the repumping light can also contribute to the laser cooling or in the opposite produce heat, which makes the distinction between the cooling laser and the repumping laser does not make much sense. Here, we still label the two lasers as the cooling light and the repumping light to denote they are corresponding to different hyperfine ground states. In contrast to the ^{87}Rb atoms, the power balance and polarisation maintaining of the repumping light is also required to be considered. According to the nature of the fibre splitter, the output powers can be balanced only if the polarisation of the input beam is aligned in the same direction with the slow axis of the fibre, therefore, an extra effort on the design of optical transmission to put the polarisation of the cooling and the repumping beams in the same direction has to be made.

3.2.1 Fibre preparation

To make the optics compact, optical fibres are commonly used in most cold atom experiments. In contrast to the fibre used in optical communication, these fibres used in cold atom experiments should be polarisation maintaining. In our experiment, to produce the ultracold mixture of Rb and K atoms, the fibres are required operating at both wavelengths 780 nm and 767 nm. It however cannot be fulfilled rigorously. The 2:2 beam splitters being used in our experiment can provide a power balance between the two laser outputs is 51% to 49% at the wavelength 780 nm and at wavelength 767 nm, it can be wrong up to 25%. It brings some detrimental effects, including the limit on the cooling efficiency, the misalignment of the centres of ^{87}Rb and ^{39}K MOTs or the centres of ^{87}Rb and ^{41}K MOTs and etc. This misalignment is potentially to impede the research on inter-species thermodynamics if the atom density is dramatically affected. Therefore, a density filter is required to re-balance the laser powers in some occasions.

To precisely control the power and frequency of the lasers and fast switch off the lasers completely, the AOMs with variable voltage attenuators (VVAs) and digital switches are required to be used before the fibre coupling (See the supplement).

To implement the MOT cooling and the sub-Doppler cooling for ^{87}Rb and ^{39}K atoms or ^{87}Rb and ^{41}K atoms, the optical setups are coupled into a layout as shown in Fig. 3.3

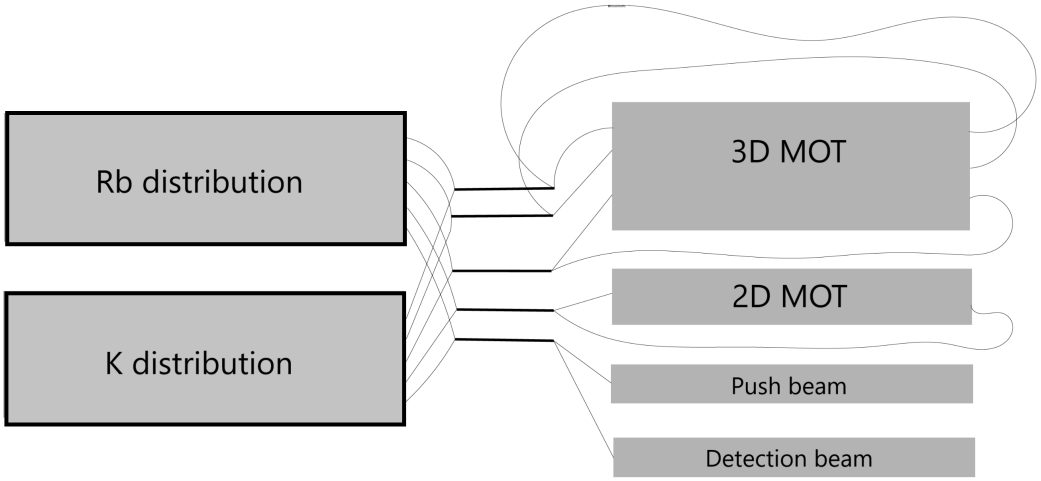


Figure 3.3: Schematics of the fibre transmission.

For ^{87}Rb distribution, the optical setup has been shown in a layout Fig. 3.4

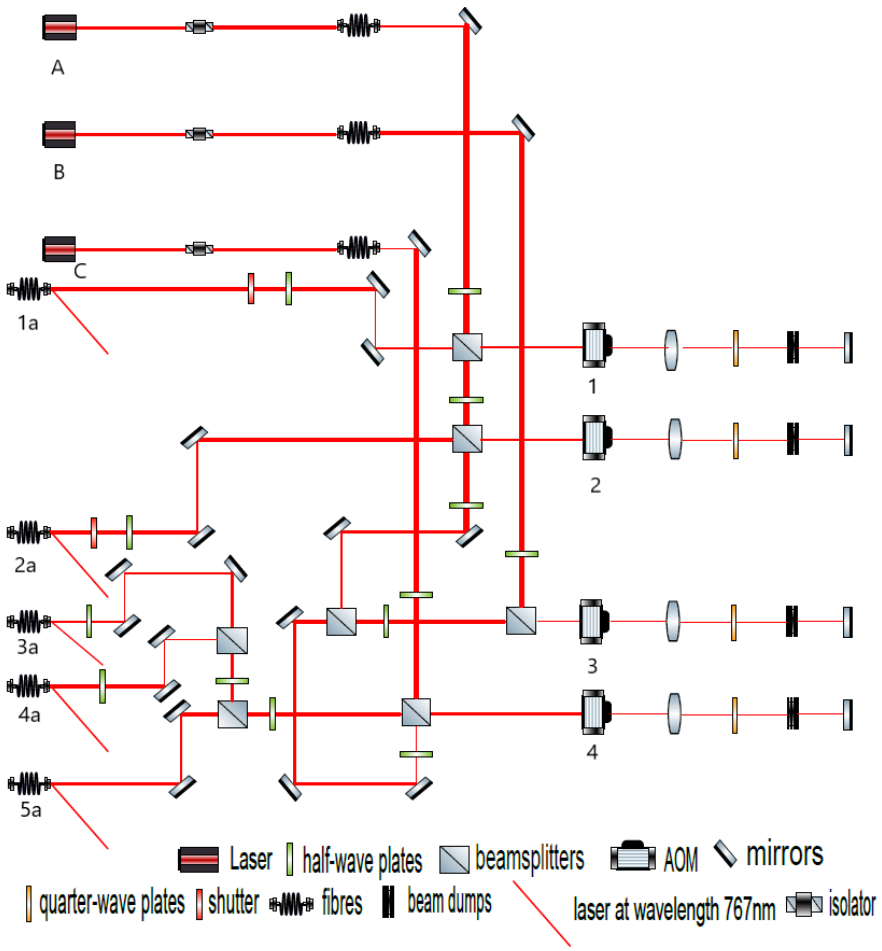


Figure 3.4: Schematics of the laser layout used for ^{87}Rb laser cooling. The input lasers are from 3 TAs and their frequencies are already locked.

The laser beams after the TAs pass through 4 AOMs. The three inputs A,B, and C are used for 2D MOT cooling pushing detection, repumping, and 3D MOT cooling, respectively. The AOMs are used to control the light intensity. The frequency settings of the AOMs are -156.4 MHz, -158 MHz, -156.4 MHz, and -141.6 MHz, respectively. There are 5 fibre couplers, 1a is for the pushing detection beams, 2a is used for the 2D MOT beams, and 3a,4a,5a is used for the 3D MOT light.

For the ^{39}K distribution, in contrast to the ^{87}Rb, all the detunings of the cooling, repumping, and etc lasers are engineered by AOMs. The layout of the laser transmission has been shown in Fig. 3.5.

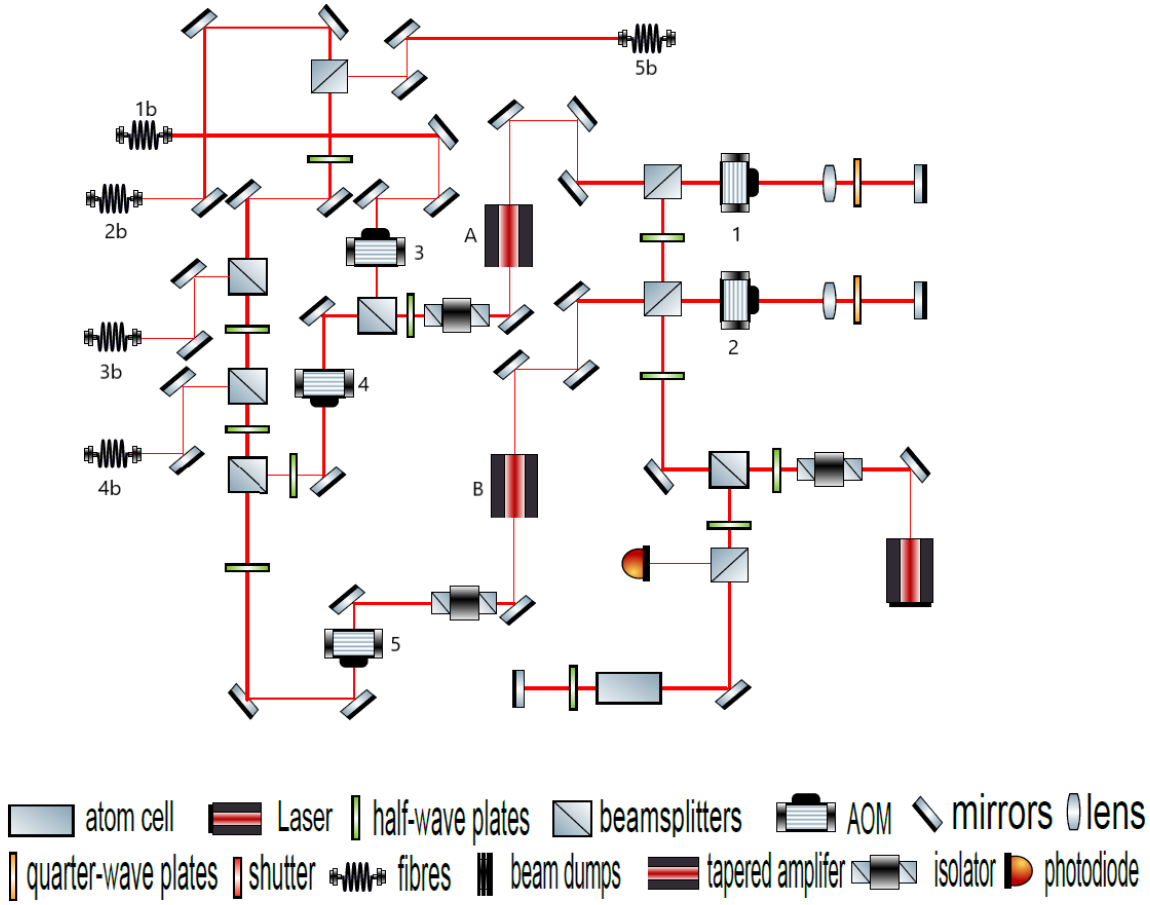


Figure 3.5: Schematics of the laser layout used for ^{39}K laser cooling. The laser input is from Optica It is locked by the absorption spectroscopy shown in the figure.

The seed laser passes through 2 AOMs before being sent into the TAs. The frequency shift from the AOMs is -157.5 MHz (AOM 1) and 141.2 MHz (AOM 2). They are used to provide control of the frequency detunings. The output of TA A is used for the cooling pushing detection and the output of TA B is used for the repumping. The beams continually pass through 3 single-pass AOMs their frequencies are -81.5 MHz (AOM 3), -68.7 MHz (AOM 4) and 70.7 MHz (AOM 5). They are responsible to provide the intensity control. The 5 fibre couplers, 1b is for the pushing detection beams, 4b is used for the 2D MOT beams, and 2b,3b,5b are used for the 3D MOT light.

The design for the ^{41}K distribution has been shown in Fig. 3.6

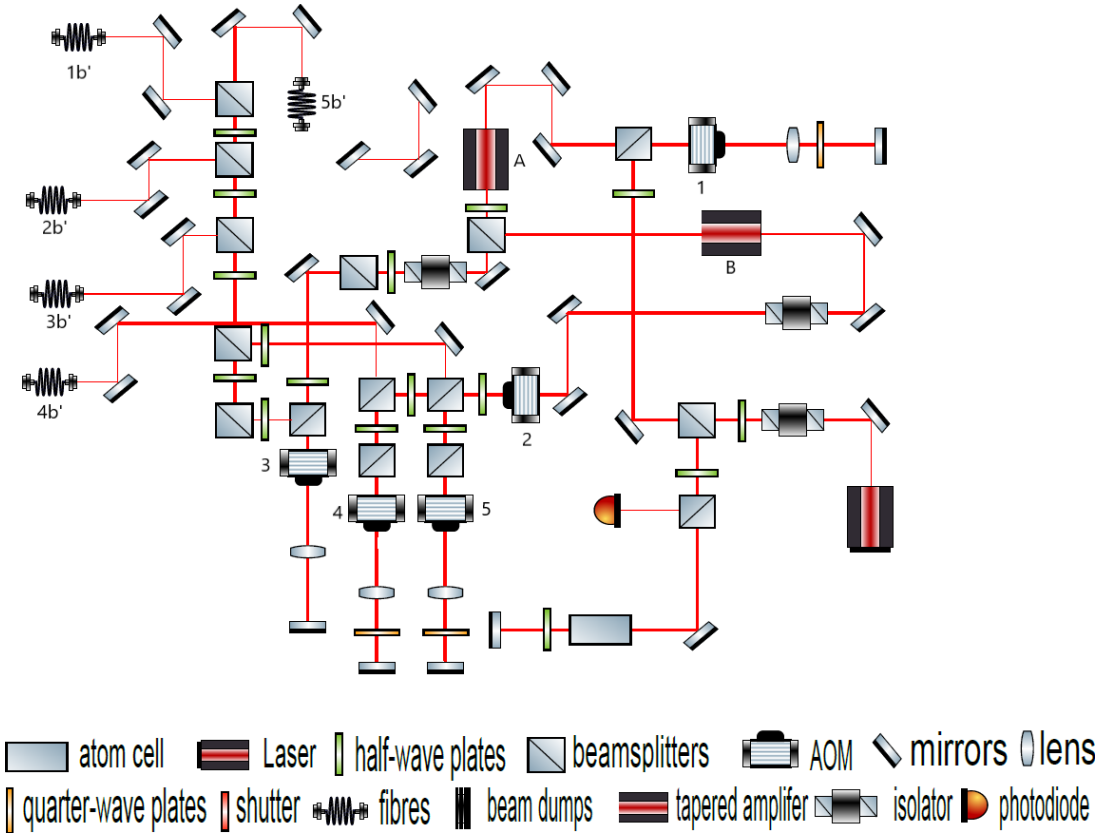


Figure 3.6: Schematics of the laser layout used for ^{41}K laser cooling. The laser input is from Optica It is locked by the absorption spectroscopy shown in the figure.

The seed laser passes through a double pass AOM 1 at first, whose frequency shift is 156.2 MHz. The output beam is sent to the TA A and then split into two beams, one of them is sent to the TA B. The output of TA B continually passes through a single pass AOM 2 and then further split into 2 beams and pass through 2 double pass AOM 4 5. They create 79.3 MHz, -176 MHz, and AMO -158.6 MHz frequency shifts, respectively. The output of the TA A also passes through a double pass AOM 3, it can provide 160.8MHz frequency shift. The AOM 3 is for the repumping light, the AOM 4 5 are used for the pushing detection, and cooling. All of them are responsible for the control of the intensity and the frequency detunings. The 5 fibre couplers, 4b' is for the pushing detection, 3b' is used for the 2D MOT beams, and 1b',2b',5b' are used for the 3D MOT.

In our experiment, the polarisation stability is mainly affected by the quality of the

fibre. In our experiment, the polarisation-maintaining (PM) fibre splitter can achieve an extinction ratio >20dB. Additionally, due to the polarisation drift that can be also produced by the temperature fluctuation of the environment and the mechanical stress on the surface of fibre, some extra efforts have been also made. Such as fixing the fibre to the optical table, where the accidental movement of the fibre and the heat exchange between fibre and the environment can be both inhibited.

As discussed previously, due to the hyperfine splittings of ^{39}K and ^{41}K atoms are 21.1 MHz and 13.4 MHz, the polarisation of both cooling and repumping lights needs to be aligned to the same direction of the slow axis of the fibre. Unfortunately, in practice, because the cooling and the repumping lasers are aligned and overlapped through PBCs, the polarisation cannot be aligned to the same direction without power loss. As a solution, the lost power is effectively used for the 2D MOT in our experiment, by paying the price that the relative powers of the cooling and the repumping lights can no longer be tailored independently for the 2D and 3D MOT.

3.2.2 Magneto-optical trap

In the 2D MOT chamber, the atoms are directly loaded from the background [63–65]. The polarisation of the input beam, comprising the cooling and repumping lights for both species ^{87}Rb and ^{39}K or ^{87}Rb and ^{41}K passing through a zeroth-order $\lambda/4$ wave plate, is changed from linear to circular. A cylindrical lens expands the beam shape rectangular at size $5cm \times 2cm$. The beam then passes through the 2D MOT chamber and is retro-reflected by a large prism. The reflection of the prism flips the polarisation of the beam from σ^- to σ^+. In total, this design can construct a $\sigma^+ - \sigma^-$ configuration for the 2D MOT. Combined with a 10 G/cm magnetic field gradient, an axial-eccentric trapping potential can be created. The magnetic field is produced by the pair of Anti-Helmholtz coils.

In the zero-field direction, assuming the atoms can only escape from the optical pump region if they are moving fast, the maximum velocity of the loading atoms can be estimated

as

$$F = m \cdot a = \frac{\Gamma \hbar \pi}{m\lambda} \tag{3.2}$$

$$t = \sqrt{\frac{2s}{a}}, v_m = d/t \tag{3.3}$$

where Γ is the scattering length, and d is the beam size in the zero-field direction. This provides a velocity selection in the zero-field direction.

After that, the loaded atoms are transported to the science chamber by the push beam. The atom flux is collimated by a differential stage and the atomic transfer rate is approximate 1×10^9 atoms/s. In the 3D MOT as shown in Fig. 3.7, the counter-propagating beams are collimated by spherical tube lenses and then overlapped with the atom flux. The polarisation configuration in the 3D MOT is also $\sigma^+ - \sigma^-$ and the magnetic gradient is produced by a sealed anti-Helmholtz coil at the centre of the trap. More than in the 2D MOT, a pair of compensation coils is used to align the MOTs for both atomic species, the Zeeman splitting of the atoms is produced by an additional bias coil, and a quick switch provided by a MOSFET is also applied. In the future experiment, a uniform magnetic field for the Feshbach resonance control is required, it can be achieved by flipping the polarity of the coils from the anti-Helmholtz to the Helmholtz configuration. Therefore, an insulated gate bipolar transistor (IGBT) has also been used in our experiment.

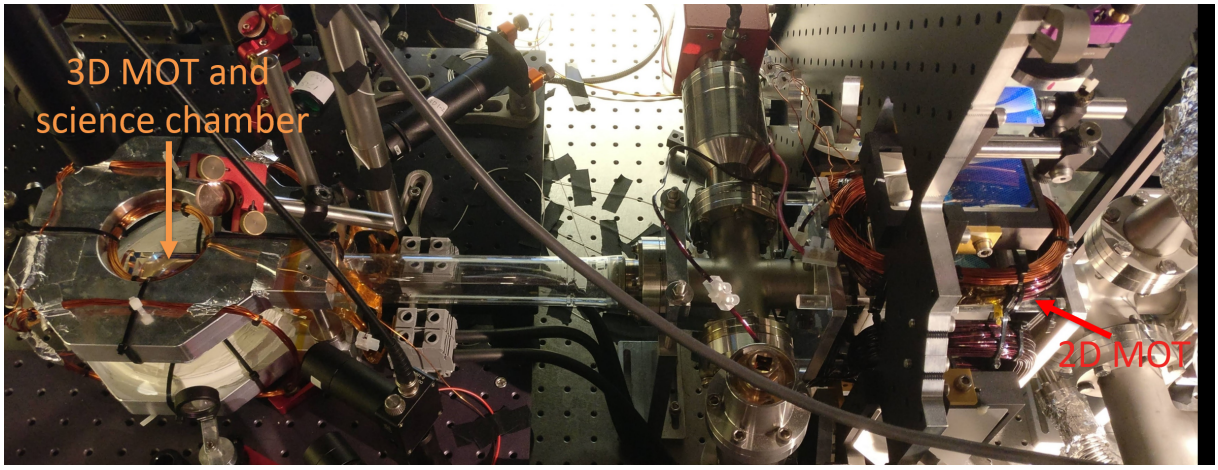


Figure 3.7: Picture from the top of the vacuum system, with the 3D MOT chamber in the left and the 2D MOT chamber in the right.

Due to the presence of both Rb and K atoms, the lights at wavelengths 780 nm and 767 nm are mixed by polarization beam splitter (PBS) before the fibre transmission. After that, the imbalances of the laser outputs at wavelength 767 nm are 15%, 20%, and 25% for each pair of beams in the 3D MOT. This can be re-balanced by using the density filters with attenuation -1 dB. All the optics after fibre transmission are coated within a 15 cm long and 1-inch diameter lens tube.

3.2.3 Optical dipole trap

Evaporative cooling can be achieved in either a magnetic trap or an all-optical dipole trap. In our work, the all-optical regime is selected due to it has a faster repetition rate (less than 10s per measurement instead of 1min in the magnetic trap) and is independent with respect to the Feshbach field. After the dark MOT, the PSD of ^{87}Rb atoms can reach 3×10^{-6} that is sufficient for atom loading into the dipole trap. Once the atoms are loaded, adiabatically reducing the dipole potential, the temperature of atoms can be reduced by paying the price of atom loss. As a result, a BEC can be observed when the PSD is enhanced up to >2.612 by the evaporative cooling.

The optical dipole trap is produced by two far detuned lasers at the wavelengths 1550 nm and 1070 nm with beam waists 35 μm and 45 μm, and their full powers are 4 W and

11.5 W, respectively. Compared to a single beam design, the evaporative cooling can be achieved more efficiently in a crossed dipole trap. This is because the re-thermalization rate can be enhanced by avoiding a lower trapping frequency in the axial direction of the laser. (In the single beam design, the trapping frequencies in the radial direction is 2 orders of magnitude more than in the axial directions.) Our experimental layout has been shown in Fig. 3.8

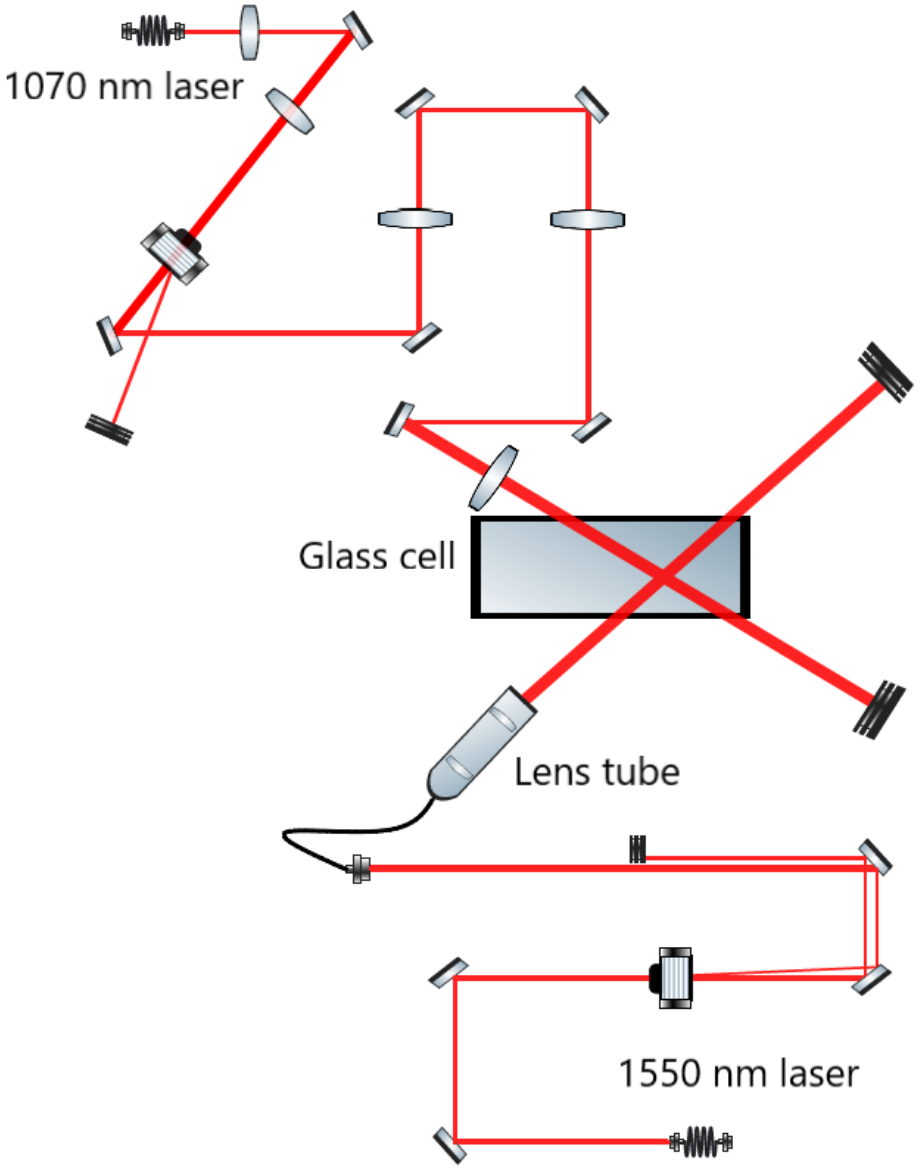


Figure 3.8: Layout of the transmission of the laser beams for the optical dipole trap. Yellow (green) beam represents 1070 nm (1550 nm) beam.

The 1550 nm and 1070 nm lasers are overlapped at an angle 40^o and the single-pass AOMs provides the power control and the on/off switch. The power stability of 1550 nm laser is protected by a temperature control, the 1070 nm laser is a IPG-Photonics ytterbium multimode fiber laser which is also fulfill the requirement on power stability. The absorption imaging measurement can be taken in any stage of the evaporative cooling, which allows us to check the beam alignment: the propagation direction of the 1070 nm beam can be adjusted until we can see a clear beam cross with the 1550 nm beam. Then the fine-adjustment can be achieved by optimizing the optical density of the atoms in the beam cross. The measurement of the waists of these beams has been shown in Fig. 3.9.

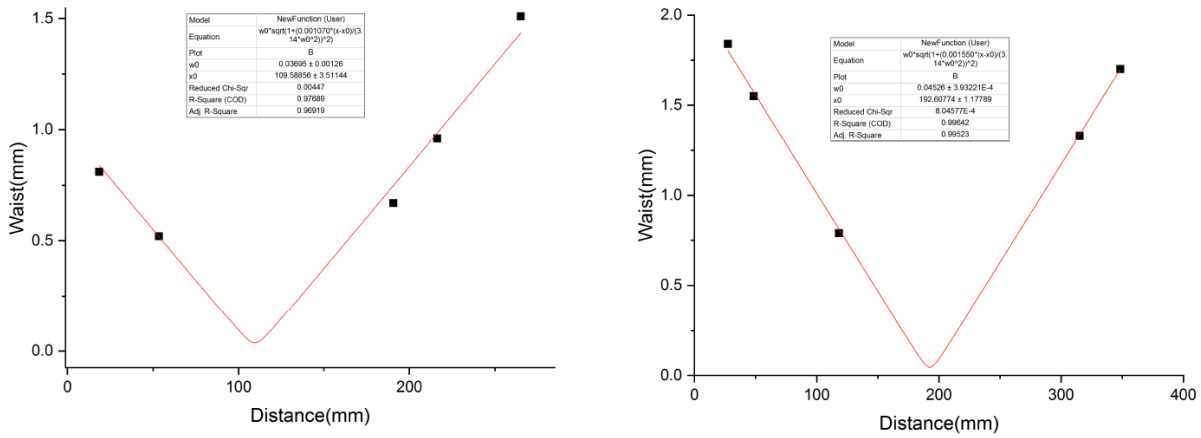


Figure 3.9: Measurement of the widths for dipole trap beams. left (right) beam represents 1070 nm (1550 nm) beam.

the data are fitted by the Gaussian profile. In fact, the atoms behave as a mechanical oscillator in this trap, the frequency of this oscillation is referred to as trapping frequency. The geometric average trapping frequency in the 3-dimensional frame is $\omega_{mean} = \sqrt[3]{\omega_x\omega_y\omega_z}$.

One approach to measuring the trapping frequency is the parametric heating measurement [66, 67]. It is based on the fact when the atoms occupy the ground state, a small external sinusoidal modulation on the trapping depth can only cause a dramatic atom loss when its frequency is twice the fundamental frequency $2\omega_{trapping}$, as shown in Fig.

3.10.

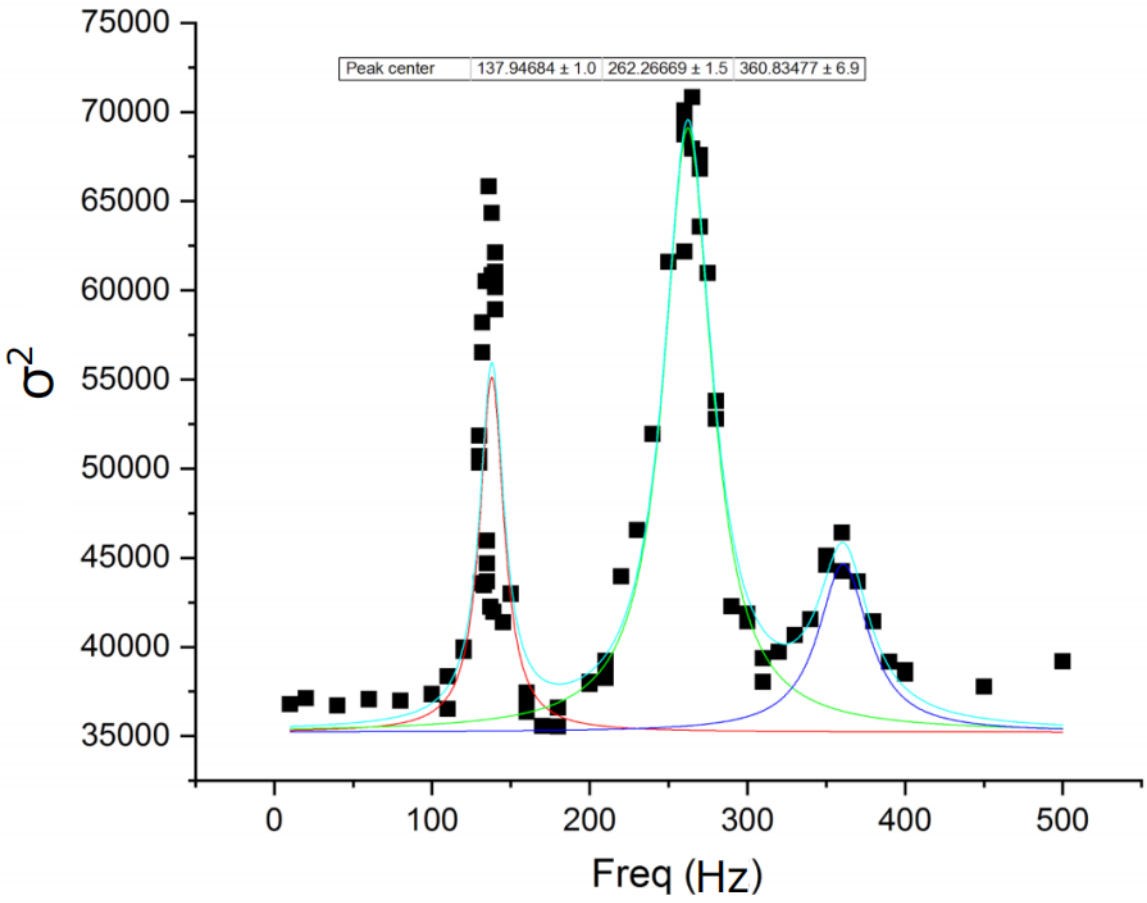


Figure 3.10: Trapping frequency measurement through parametric heating approach: The average width of the atom cloud in the optical dipole trap has been measured after 20ms TOF as a function of the modulation frequency applied to the 1070nm trap beam. The depth of the modulation is 10% of the total beam power.

However, a direct atom loss observation may be confused by the atom loss at the fundamental frequency, therefore the diameter of the atom cloud is instead observed after the end of evaporation and a 3s holding time. The measured trapping frequencies are 69 Hz, 131 Hz, and 180 Hz (the half values of the frequencies of three peaks recognized in the Fig.3.10) and their geometric mean value is $\omega_{mean} = \sqrt[3]{\omega_x\omega_y\omega_z}$=117.6 Hz.

The collective mode measurement can be also used to measure the trapping frequency [68]. In this measurement, the collective motion of the atoms is stimulated by

an external kick of the trapping potential [68], which can be produced by applying a magnetic gradient pulse at the end of the evaporation. After a variable amount of holding time, an oscillation of centre of mass (CM) of atoms can be observed, whose frequency is the trapping frequency of the atoms. As shown in Fig. 3.11

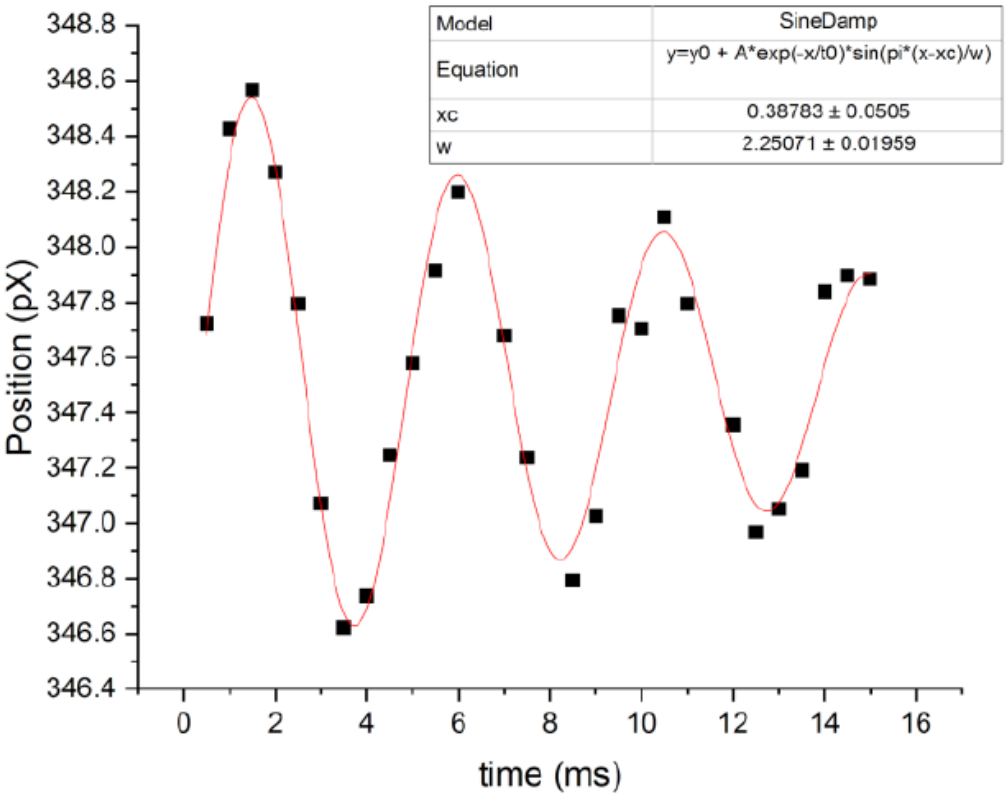


Figure 3.11: Trapping frequency measurement through collective mode of BEC: The centre mass of the atom cloud in the optical dipole trap has been measured with 20ms TOF after a magnetic gradient pulse and a variable amount of holding time.

The horizontal coordinate is labeled by the pixels on the camera (1 pixel = 6.45 μm). The result of the trapping frequency is 222 Hz (the half value of the oscillation frequency recognized in the Fig.3.11), compared with the result in the parametric heating measurement, they coincide within 20%.

Additionally, in the all-optical dipole trap, all of the Zeeman components of atoms can be held, for the research of the thermodynamics of two species mixture, a distillation to a specific component is required (see the supplement).

3.3 Detection system

An ultracold atom gas can be held by the optical dipole trap for up to several seconds. However, it is too small (40 μm) and too cold (100 nK) for applying a contact measurement, as a solution, the optical diagnostic measurement is widely used in cold atom experiment [69]. In our experiment, the absorption imaging or the fluorescence imaging is achieved after a time of flight (TOF) by taking a photo of the detection beam or the fluorescence of the atoms through a high spatial resolution camera. The frequency of the imaging beam is set on resonance with respect to the atomic transition and this detection can provide the information about the number and the temperature of the atoms.

Our cameras are Guppy Pro F-031 from Allied Vision techniques (AVT) which has 656×492 pixels for horizontal imaging and Marko G-040 which has 728×544 pixels for vertical imaging. The exposure time of the camera is precisely controlled by a computer-based program. The imaging process is achieved by two telescopes with different magnifications 3:1 and 1:2.6, which can help to take a clear photo of either of the cold atoms in the 3D MOT or of the ultracold atoms in the optical dipole trap. As shown in Fig. 3.12, the optical path can be easily changed from one telescope system to another by flipping the mirror.

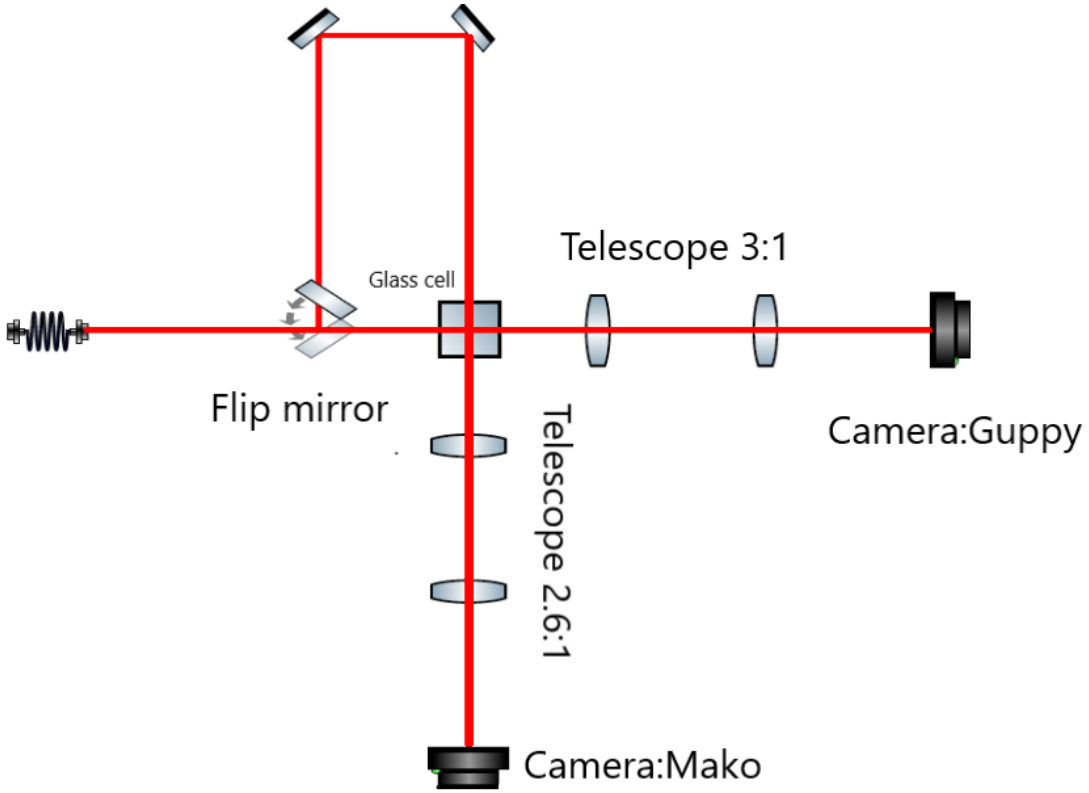


Figure 3.12: Schematics of the imaging system.

In principle, either the absorption imaging or the fluorescence imaging relies on the interaction between the photons and the atoms. The atomic absorption of probe field is ruled by Beer-Lambert law:

$$I = I_0 exp\left(-\int n(z)\sigma dz\right) \tag{3.4}$$

where n(z) is the density of the atoms and I_0 is the intensity of the probe beam. σ is the absorption cross-section, which is defined as

$$\sigma = \frac{\sigma_0}{1 + 4(\Delta/\Gamma)^2 + I_0/I_s} \tag{3.5}$$

where Γ is the linewidth of the atomic transition, I_s is the saturation intensity, and $\sigma_0 = \frac{\hbar\omega\Gamma}{2I_s}$ is the resonant absorption cross-section. To implement the absorption imaging, 3 pictures are taken, the picture of the probe beam after the absorption I_1, the picture

of the probe beam without absorption I_2, and the picture of the background I_3. The optical density of the atoms Ω can be deduced by $\Omega = -ln(\frac{I_1-I_3}{I_2-I_3})$. When the probe beam is resonant and at low intensity ($\Delta \approx 0$, $I_s \gg I_0$), the absorption cross-section is reduced to σ_0. The number of the atoms $N = \int n(z)dz$ can be deduced by $\Omega = \frac{\sigma_0 N}{2\pi}$. The accuracy of the measurement is protected by avoiding saturation of the absorption during the measurement.

For the fluorescence, the total number of the photons is determined by its decay rate which can be calculated out by

$$R_{sc} = (\frac{\Gamma}{2})\frac{(I/I_s)}{1 + 4(\Delta/\Gamma)^2 + (I/I_s)} \tag{3.6}$$

to deduce the atom number from the measured photon number, the solid angle of the camera with respect to the atom cloud need to be estimated by

$$d\Omega = \frac{A_d}{\Omega} = (\frac{D}{4d_0})^2 \tag{3.7}$$

where $d\Omega$ is the solid angle to the detector, D is the effective aperture of the first detection lens and d_0 is the distance from the atom cloud to the first detection lens (a telescope system is applied to collect the photons into the active area of the camera). The atom number can be read out from $N_{det} = NR_{sc}d\Omega$. Where N_{det} is the detected photon number from the camera.

Furthermore, the temperature of the atom cloud can be also deduced by fitting the optical density distribution of the image. When $T > T_c$, the density distribution is assumed to be ruled by a Gaussian profile (here the density means the column density, it can be obtained by integrating the respective density distribution along the detection axis z), where T_c is the critical temperature:

$$\Omega = \sigma_0 \frac{N}{2\pi\sigma_x\sigma_y} exp\left[-\frac{(x-x_0)^2}{2\sigma_x^2} - \frac{(y-y_0)^2}{2\sigma_y^2}\right] \tag{3.8}$$

where N is the total number of atoms and σ_x and σ_y are the width of the distribution.

After a TOF, the width is ruled by Maxwell-Boltzmann distribution,

$$\sigma_{TOF}^2 = \frac{t_{TOF}^2 T k_B}{m} \tag{3.9}$$

where k_B is the Boltzmann constant and T is the temperature of the atoms. Initial the width of the trapped atoms, the temperature of the atoms can be extracted from

$$\sigma^2 = \sigma_{trap}^2 + \frac{T k_B}{m} t^2 \tag{3.10}$$

in Fig. 3.13

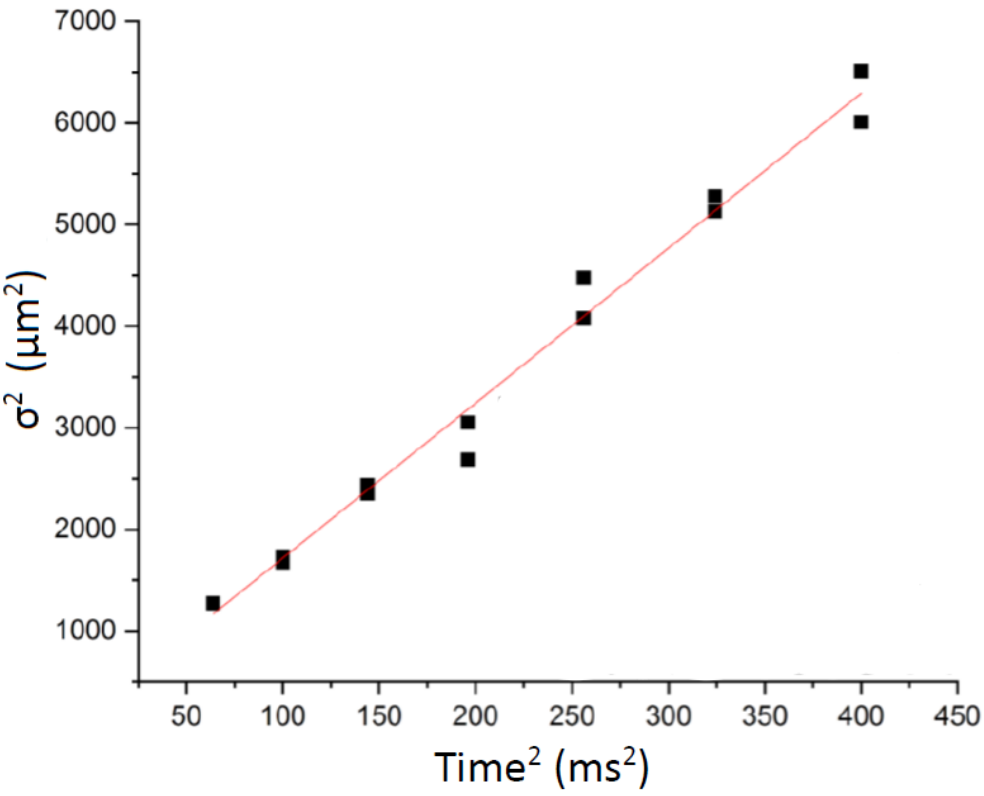


Figure 3.13: Temperature measurement of the ultracold atoms. The black solid dots are the experimental measurement of $\sigma^2 = \sigma_x^2 + \sigma_y^2$. The red line is the linear fit of σ^2 over the square of the expansion time t^2.

where σ_{trap} is the width of the atom distribution in the optical dipole trap and the result associated with the temperature is 156 nK.

In another limit $T << T_c$, the density distribution is ruled by the Thomas-Fermi distribution

$$\Omega = n_{TF}^2 max(1 - \frac{(x-x_0)^2}{r_x^2} - \frac{(y-y_0)^2}{r_y^2}, 0)^{3/2} \tag{3.11}$$

where n_{TF}^2 is the atom density of the condensate. Its TOF is also ruled by Maxwell-Boltzmann distribution.

In the more common case, the condensed component and the non-condensed component (or the thermal component) can coexist in measurement, an effective fit model, bi-model, combined with the Gaussian distribution and the Thomas-Fermi distribution is applied. The proportion of the Thomas-Fermi distribution and the Gaussian distribution is referred to as BEC fraction. Furthermore, when the temperature below the transition value, due to the momentum distribution an associated polylogarithm, the distribution of the atoms is ruled by Bose-enhanced distribution instead of the Gaussian distribution. This effect on our data analysis will be discussed in the later chapter.

3.4 Computer control system and data acquisition

The accuracy and the reliability of the experiment are protected by a computer-based control system which has three parts: Cicero program, PXI controller, and the field-programmable gate arrays (FPGA). Cicero is a program used to modulate the experimental parameters through both digital and analog channels, meanwhile it can also communicate with the data acquirement program to complete the experiment measurement. PXI controller is a hardware unit that stores the sequence and triggers FPGA to execute the experimental procedure. It includes several individual chassis:

(1) PXI 8360: It connects the other chassis with the computer.

(2) PXI 6533: It provides 32 digital channel control signals.

(3) PXI 6713: It controls 8 analog channels.

The layout of the control system has been shown in Fig. 3.14

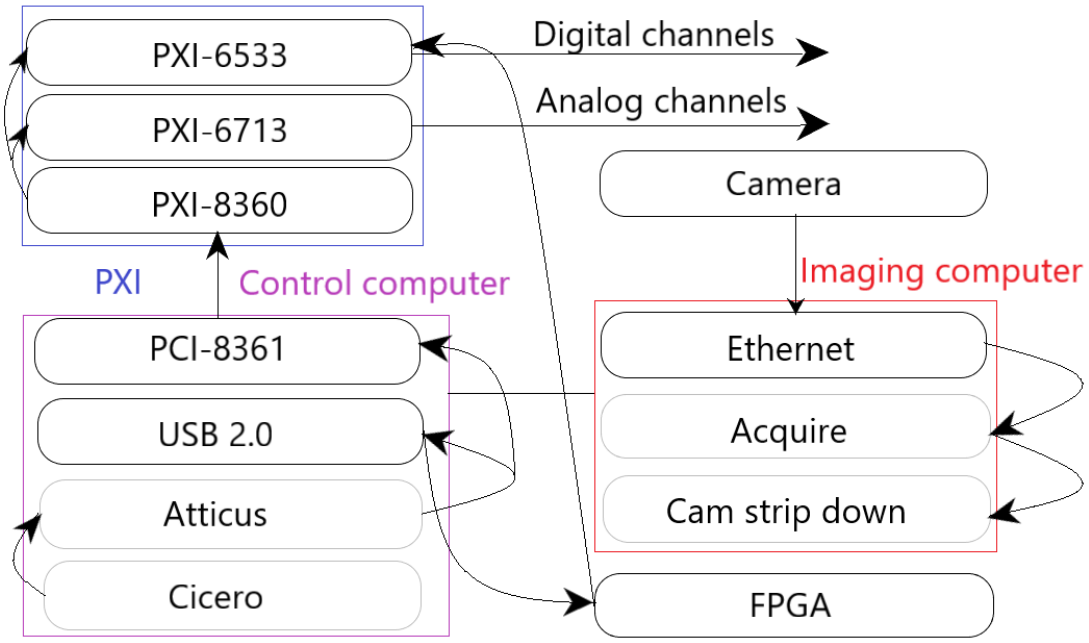


Figure 3.14: Schematic of control system.

8 analog channels and 32 digital channels can provide -10V to 10V control voltage with an update rate 1 MHz and 5V TTL with an update rate 40 MHz. This in turn means the time resolution of the controls are 1 μs and 25 ns. The experimental sequence for ^{87}Rb BEC on the interface of Cicero has been shown in Fig. 3.15

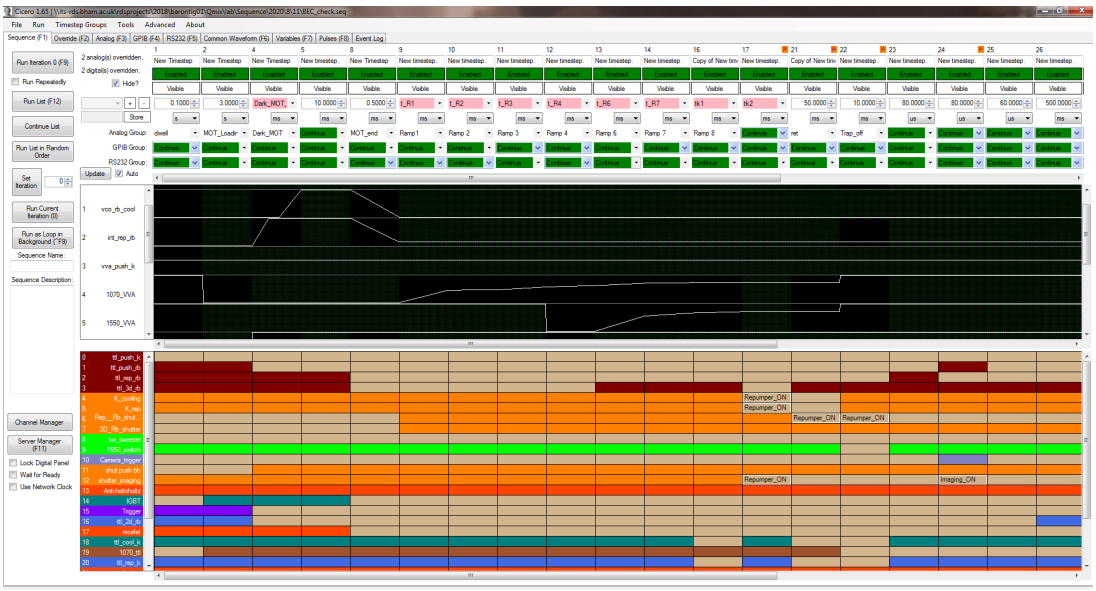


Figure 3.15: The experimental sequence on the interface of Cicero.

In this sequence, the evaporative cooling can be achieved as shown in Fig. 3.16

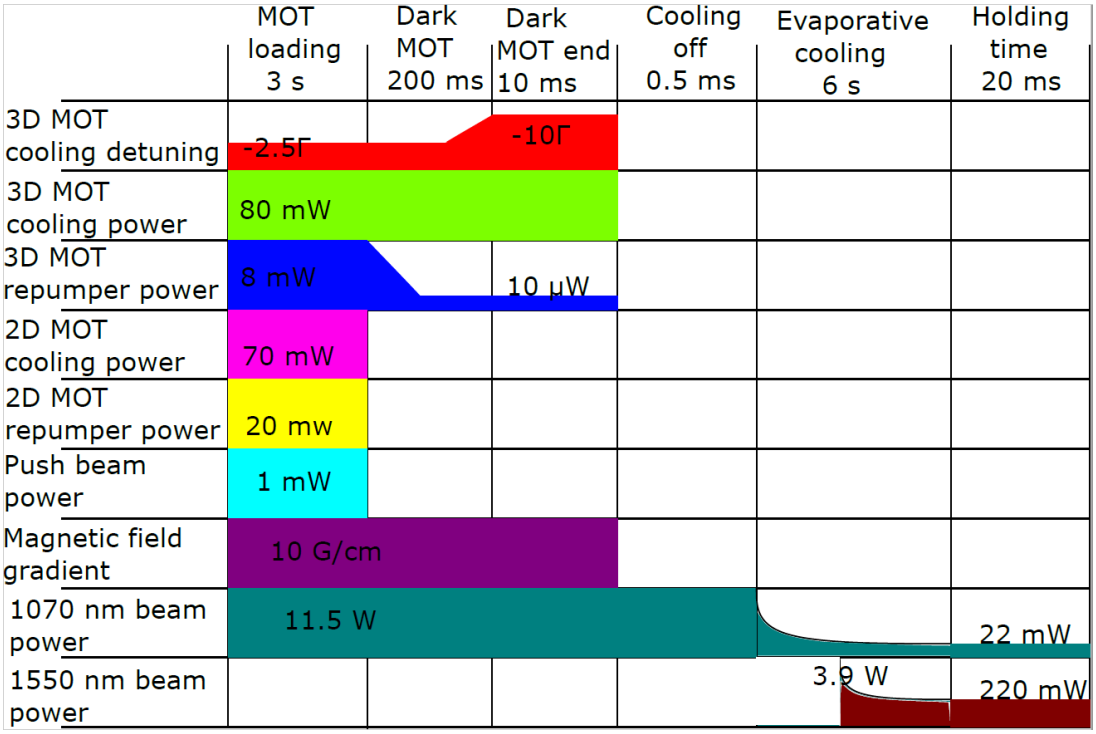


Figure 3.16: The experimental sequence for ^{87}Rb BEC.

In the beginning, a ^{87}Rb 3D MOT is loaded with the cooling light being locked at red detuning, 2.5 Γ, and the repumping light being resonant. The magnetic gradient is 10 G/cm and the laser at wavelength 1070 nm is switch on with full power during the MOT loading. After 4s, 10^9 ^{87}Rb atoms at temperature 300 μK can be loaded. Then, a dark MOT is achieved by ramping the detuning of the cooling light from 2.5 Γ to 10 Γ and reducing the intensity of the repumping light to 3% with respect to the full power. Due to the photon mediated repulsive inter-particle interaction has been avoided in the dark MOT, the atom density can be strengthened. At the same time, the polarisation gradient cooling is eligible to reduce the temperature when the centre of MOT has a higher atomic density and 0 magnetic field. Eventually, 10^8 atoms at temperature 60 μK can be produced that makes it possible to load a sufficient number of atoms in the optical dipole trap as shown in Fig. 3.17. From a rough estimation, at least 10^7 atoms are trapped. (The number of atoms is observed after 50ms of thermalization time, which

is underestimated due to the anisotropic geometry of the atom cloud.)

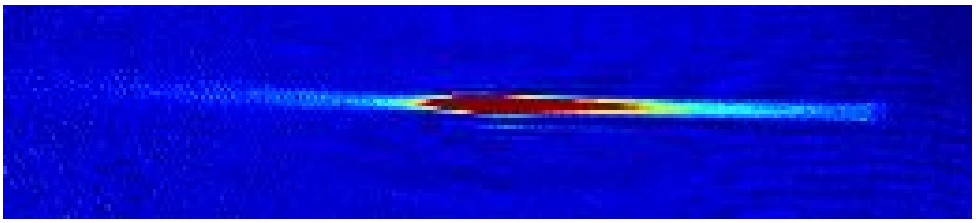


Figure 3.17: Measurement of the atoms in the optical dipole trap. The atoms are trapped by the laser at wavelength 1070 nm with power 12 W. The photo is taken from the horizontal imaging system.

At the initial stage of the evaporative cooling, an exponential power ramping of the 1070 nm laser from 11.5 W to 1.2 W is carried out in 1.5s. Then, the 1550 nm light is switched on with its full power, both the 1070 nm and 1550 nm laser powers are continually ramping down to 1% and 5% with respect to their full powers in the later 6s. Due to the rethermalization rate scales as the trapping frequency, to maintain the remaining atoms sufficiently rethermolized, the ramping rate is required to be slowed down. After the end of evaporation, the dipole trap is still held with a constant power for 2s to complete the on-going rethermalization. A BEC with 10^5 atoms can be observed through absorption imaging after a 25 ms ballistic expansion as shown in Fig. 3.18

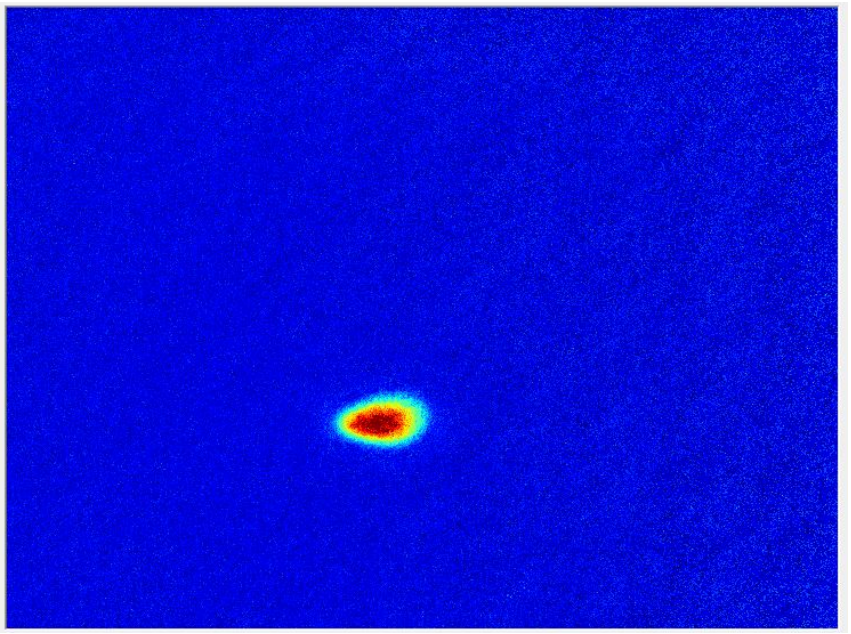


Figure 3.18: Absorption image of a BEC after 25 ms ballistic expansion.

The sequence in Fig. 3.15 is designed for the investigation of the evaporative cooling in a dissipative environment, where during the evaporative cooling of ^{87}Rb atoms, the 3D MOT of ^{39}K atoms is switched on to create a dissipative environment.

The data analysis has been implemented after absorption imaging. The photos of the atom cloud can be saved with the experimental settings in an image acquisition program. A real-time analysis, fitting the column density of the atom cloud with Gaussian distribution or Thomas-Fermi distribution is completed, as shown in Fig. 3.19

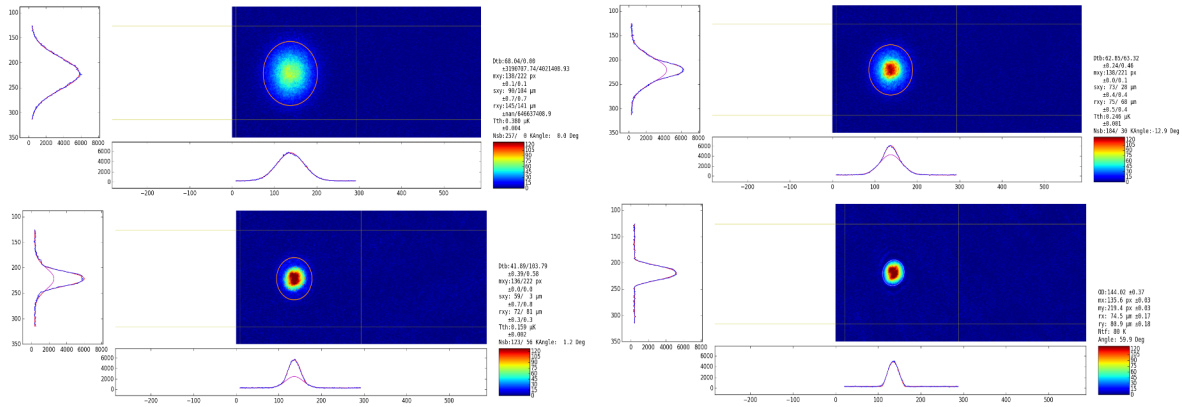


Figure 3.19: Absorption measurement of BEC with different BEC fraction. (top left) fitting by the Gaussian profile, (bottom right) fitting by the Thomas-Fermi profile, (top right and bottom left) fitting by the bi-model distribution.

The thermal wings of the fitting profile of the ultracold atoms disappear when the BEC fraction approaches 1. It represents the atoms are ruled by a pure Thomas-Fermi distribution.

An effort on a ^{39}K BEC producing has already been made. Unfortunately, it seems frustrated to be achieved in our system (see the supplement).

3.5 Optical tweezer

3.5.1 Optical setup

The optical tweezer is a tightly focused beam from a Narrow Linewidth, tunable CW Ti:Sa (Titanium Sapphire) laser, model SolsTis from M-Squared, the wavelength can be tuned from 600 nm to 900 nm. A high numerical aperture (NA) optical objective,10x magnification Mitutoyo Apochromatic Objective, NA=D/2f, where D is the entrance pupil and f is its effective focal length and the waist is $w_0 = \frac{\lambda_0}{\pi NA}$, at the wavelength 789.82 nm, can provide a waist less than 2 μm at its working distance (34 mm). The setup of the optics has been shown in Fig. 3.20

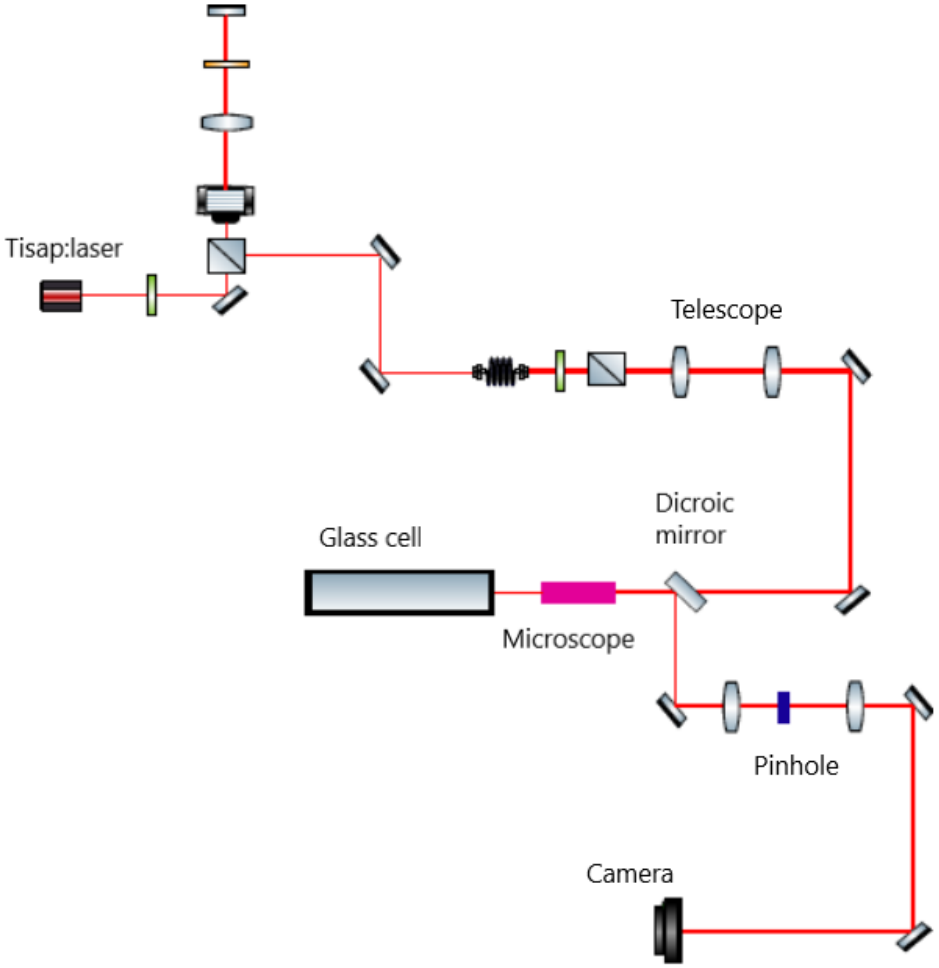


Figure 3.20: Schematics of the optic layout for the optical tweezer.

The double-pass AOM provides the power control for the tweezer light, a PBC is used to clean the polarisation, and the telescope system can expand the beam size. The incident light is transmitted through a dichroic mirror and focused into the glass cell by the microscope. The fluorescence of atoms are detected by a low noise camera, Hamamatsu C11440, a band pass filter transparent at 767 nm is placed in front of the camera. In order to eliminate the undesired reflection, a spatial filter is also used in the optical path, the diameter of its pinhole is 50 μm.

3.5.2 Tweezer loading and fluorescence imaging

The atoms are loaded into the optical tweezer during the dark MOT. The sequence has been shown in Fig. 3.21

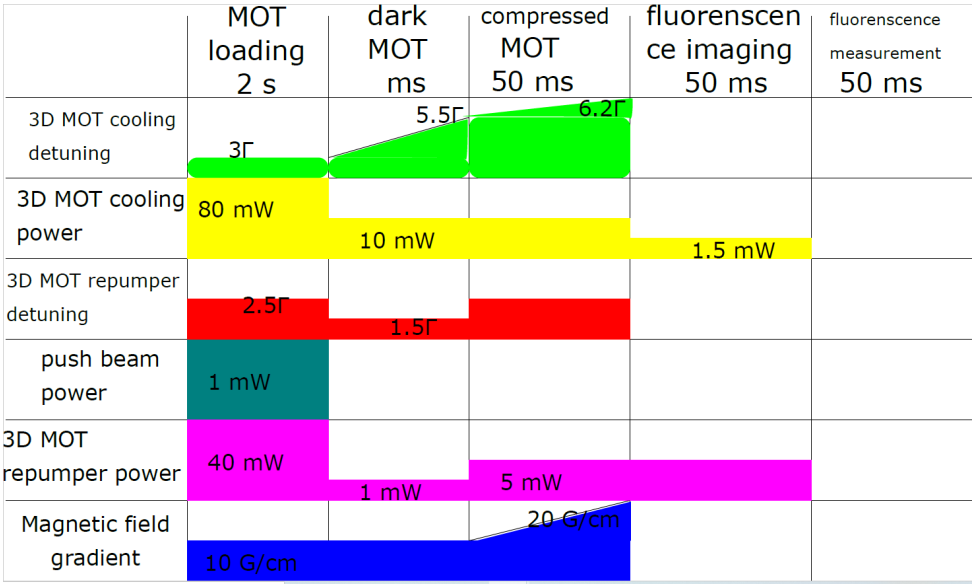


Figure 3.21: Sequence of the fluorescence imaging of the ^{41}K atoms in the optical tweezer.

At the beginning of the sequence, the ^{41}K MOT is switched on for 2s, then the dark MOT is achieved by reducing the intensity and increasing the frequency detuning for both cooling and repumping light, where the temperature can be reduced from 1 mK to 125 μK. A compressed MOT is then applied by increasing the magnetic field gradient from 10 G/m to 20 G/m and the optical tweezer is switched on during the dark MOT and the compressed MOT. A fluorescence imaging is applied to detect the atoms in the optical tweezer after compressed MOT. The imaging light here is not resonant but red detuned to avoid the atom loss caused by the light-induced heating effect. As compensation, the fluorescence efficiency can be enhanced by expanding the interrogation time in this scheme, that is 50 ms in our experiment.

The optical molasses can be also valid for the atoms in the optical tweezer. However, due to there exist an induced atomic dipole moment $\tilde{P} = \alpha\tilde{E}$, where α is the complex

polarisability, a light shift of the energy level can be produced. According to the second-order time-independent perturbation theory,

$$\Delta E_i = \sum_{i \neq j} \frac{| < j|H|i > |^2}{\epsilon_i - \epsilon_j} \tag{3.12}$$

for the two-level system, the energy shifts of the excited state and the ground state are

$$\Delta E = \pm \frac{| < e|\mu|g > |^2}{\Delta} |E|^2 \tag{3.13}$$

where $| < e|\mu|g > |$ is the dipole matrix and Δ is the energy gap between the ground state and the excited state. The light shifts are usually different for the excited state and ground state[70, 71]. Some detrimental effects might affect the laser cooling, such as fluctuating dipole force heating, inhibition of cooling due to breakdown of the hyperfine coupling, and spatial dependent detuning and scattering rate, see the reference [71]. As a solution, inspired by the method developed in [71], the tweezer and fluorescence lights are chopped by a square-wave modulation to circumvent these undesirable effects in our experiment (Chopping means when the one in the two lights is on, the other one is off). The chopping frequency is 0.7 MHz that is fast enough as to its effect on molasses can be ignored.

After the optical molasses, the fluorescence image of atoms in the optical tweezer has been taken as shown in Fig. 3.22

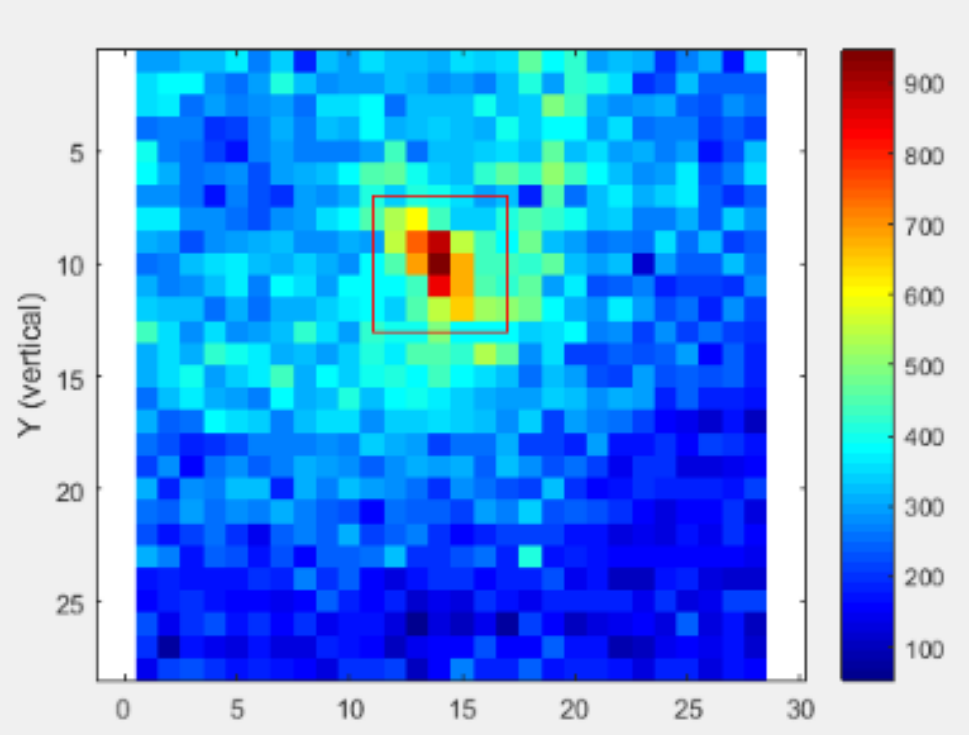


Figure 3.22: (left) measurement of the fluorescence of the atoms in the optical tweezer. Readout from the histogram measurement corresponding to these data set, we can deduce that 5 atoms are in the optical tweezer.

The molasses has been optimized following the procedure as shown in Fig. 3.23

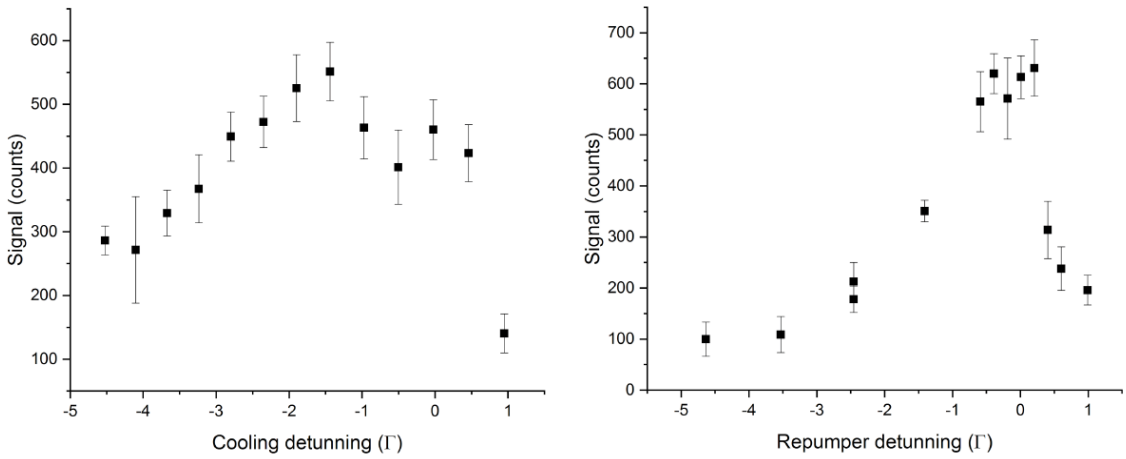


Figure 3.23: (left) Florescence imaging of the atoms in the tweezer versus the detuning of the cooling light, (right) florescence imaging of the atoms in the tweezer versus the detuning of the repumping light.

We also tried the D1 gray molasses, however, it seems helpless on strengthening the fluorescence.

Chapter 4

Results and discussion

In this chapter, I will illustrate and discuss the experiment results in detail. The text and figures are mainly from my publications [27] and [28].

4.1 Non-equilibrium supercritical BEC

4.1.1 Inducing dissipation in ^{87}Rb BEC

In previous sections, the MOT cooling and the all-optical evaporative cooling have been discussed in details. In this section, I will illustrate the experimental results of the evaporative cooling in a dissipative environment. For the ultracold atom cloud, the dissipation in turn means the heating effect and the losses of atoms. They are usually detrimental to the condensate, however, if properly tailored, a new non-equilibrium state can be achieved where the BEC fraction is significantly higher than the case in equilibrium in our experiment [14, 72]. This state is referred to as supercritical BEC and can be maintained for an accessible time in the optical dipole trap that exhibits the features of a prethermalized state (which is non-equilibrium with a long relaxition time) [18, 23].

An ultracold ^{87}Rb atoms at a temperature below 500 nK is produced in an optical dipole trap and a ^{39}K MOT at a temperature 1mK is created surrounding the ^{87}Rb atoms. The experimental scheme has been shown in Fig. 4.1

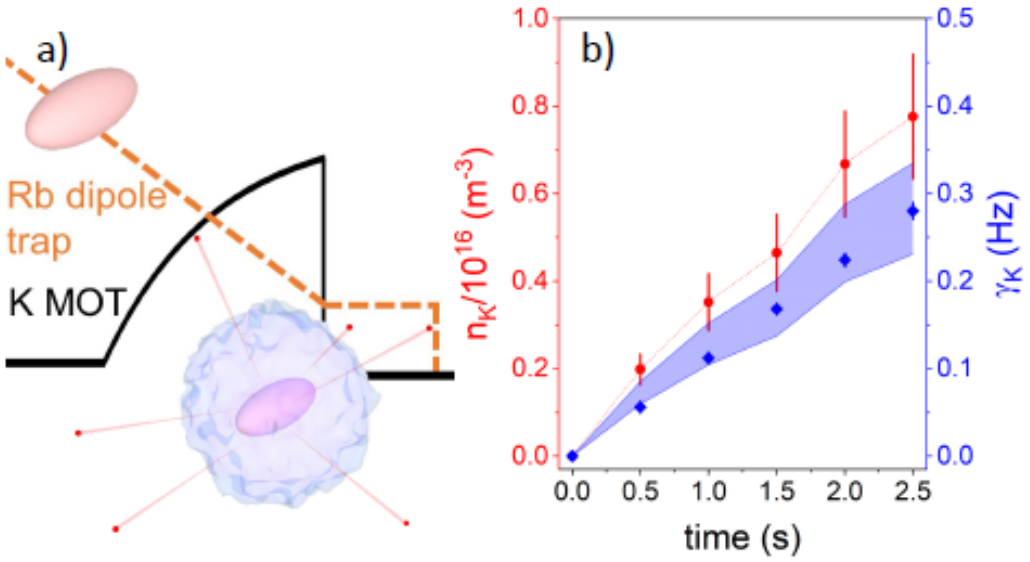


Figure 4.1: a) Schematic demonstration of the distillation protocol. we switch on an MOT of ^{39}K during the last stages of the ^{87}Rb evaporative cooling. This provides a dissipative environment for the ^{87}Rb atoms. b) The red dots are the measured densities of the ^{39}K atoms as a function of time. The blue diamonds are the measured dissipation rates of the ^{87}Rb while the blue shaded area is the calculated dissipation rate by the model explained in the text. Error bars are the standard errors of the mean. Figure and caption taken from Ref [27]

The ^{87}Rb and ^{39}K atoms are initially loaded in 2D MOTs and then transferred to the science chamber by the bichromatic push beam and recaptured by the 3D MOTs. After 4s MOT loading, 10^9 ^{87}Rb atoms at 300 μK can be obtained and its PSD is 1×10^{-6}. Then they are loaded into a crossed optical dipole trap, the two trapping beams are at the wavelengths 1070 nm and 1550 nm with an angle of 40 degrees. Their beam waists are 35μm and 45μm, respectively. In the absence of the magnetic field gradient and the MOT light, the evaporative cooling is achieved in 8s. To pinpoint the issue to inter-species thermodynamics, the ^{87}Rb atoms are distillated into the $|F{=}1, m_F = -1\rangle$ state by returning the magnetic field gradient during the last 6s of the evaporation. The trapping frequency of the crossed optical dipole trap is $2\pi\times$(70,120,120) Hz. The absorption imaging measurement of the ultracold cloud has been taken after the end of

evaporation, a 20 ms holding time and a ballistic expansion time (15 ms). The ^{39}K MOT acts as a dissipative environment surrounding the ^{87}Rb BEC, and it is loaded since the temperature of the ^{87}Rb atoms is below 1 μK. Its atomic density n_K has been shown as the red dots in Fig. 4.1 (b). Due to the temperature of the ^{39}K atoms is more than 3 orders magnitude higher than the temperature of ^{87}Rb atoms, we assume the inter-species collision is resemble to a collision between an ultracold atom cloud with classical background atoms.

4.1.1.1 Measuring the inter-species scattering rate

The scattering rate can be estimated by $\gamma_K = n_K \sigma \nu_K$, where ν_K is the average speed of the ^{39}K atoms that can be obtained from the temperature measurement and σ is the calculated cross-section. The cross-section can be deduced by using the model in reference [73],

$$\sigma(E_t) = \begin{cases} \alpha & \text{if} \quad E_t \leq E_c; \\ \alpha \left(\frac{E_c}{E_t}\right)^{7/6} & \text{if} \quad E_t \geq E_c \end{cases} \tag{4.1}$$

where E_t is the transfer energy of the collision. E_c is a defined parameter which can separate the two regimes. It is referred to as crossover energy and can be calculated by

$$E_c \approx 2\frac{\hbar^{12/5}}{C_6^{2/5}} \frac{1}{m m_b^{1/5}} E_{col}^{1/5} \tag{4.2}$$

where m and m_b are the mass of rubidium and potassium atoms. E_{col} is the energy of the collision which is approximately the kinetic energy of the potassium atom. the Van de Waas coefficient C_6 for the $^{87}Rb -^{39} K$ atoms is C_6=4290(2)$a_0^6 E_h$ [74]. From this estimation, E_c is $400\mu K$.

In eq. 4.1 α is defined as

$$\alpha = \frac{\pi}{6}\left(\frac{9C_6^2}{E_{col}}\right) E_t^{-7/6} \tag{4.3}$$

If the collision is elastic, the transfer energy can reach its maximum value,

$$E_t^{\max} = 4\frac{m_{\mathrm{Rb}} m_{\mathrm{K}}}{(m_{\mathrm{Rb}} + m_{\mathrm{K}})^2} E_{col} \approx 0.8549 mK \tag{4.4}$$

and the cross-section is

$$\sigma = \int_0^{E_c} \alpha dE_t + \int_{E_c}^{E_t^{\max}} \alpha \left(\frac{E_c}{E_t}\right)^{7/6} dE_t \approx 5.6099 \cdot 10^{-17} m^2 \tag{4.5}$$

Here, we assume the density of the ^{39}K atoms is uniform and can be estimated by $n \sim N/(4/3\pi\sigma_{cloud}^3)$, where N is the measured total number of the atoms and σ_{cloud} is the width of the atom cloud. The calculated dissipation rate has been shown as the blue shaded area in Fig. 4.1(b), which is way less than the intra-species collision rate (its value is in the range of 10-65 Hz) and due to the thermalization rate of the ^{87}Rb atoms is determined by the intra-species collision rate, it in turn means the ultracold atom cloud is still in its thermal equilibrium. Also, the losing rate of the ^{87}Rb atoms due to the scattering with the ^{39}K atoms γ_K can be also deduced from the lifetime measurement of ^{87}Rb atoms as shown in Fig. 4.2, that can be used to check the validity of the estimation $\gamma_K = n_K \sigma \nu_K$.

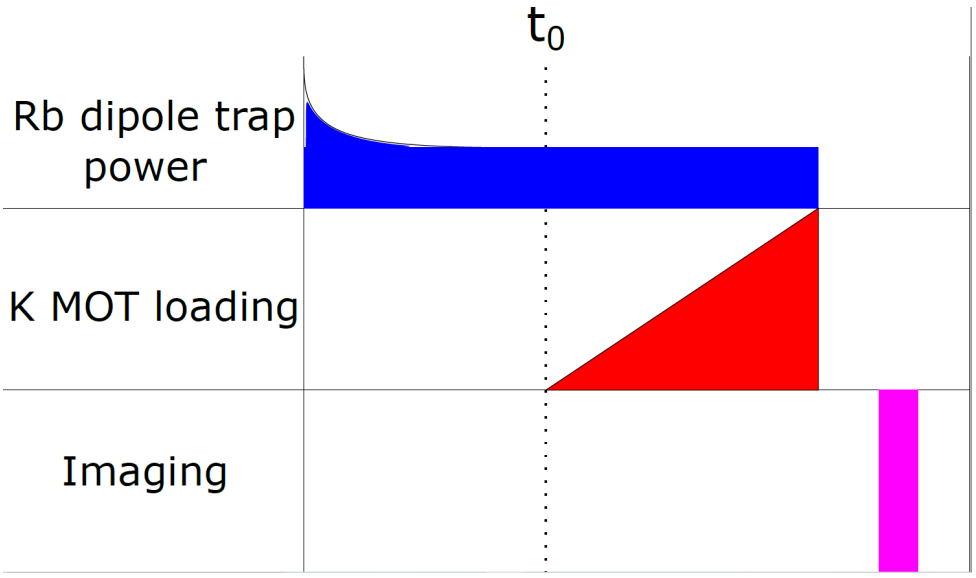


Figure 4.2: Experimental sequence used to study the dissipation rate of the ^{87}Rb atoms in ^{39}K MOT.

The ^{39}K MOT is switched on after the evaporation while the ^{87}Rb atoms are still held in the dipole trap with a constant potential. The number of the ^{87}Rb atoms decay can be written as

$$\dot{N}_{Rb} = -(\gamma_{Rb} + \gamma_K(t))N_{Rb} \tag{4.6}$$

Integrating the Eq. 4.6, the linear growth of the scattering rate is $\gamma_K = at$

$$N_{Rb}(t) = N_{Rb}(0)exp(-\gamma_{Rb}t - \frac{1}{2}at^2) \tag{4.7}$$

By engineering the laser power at the end of evaporation, we can reach two limits: the pure BEC limit and the thermal limit (no condensate). The number of ^{87}Rb atoms dissipate with or without ^{39}K MOT can be shown in Fig. 4.3

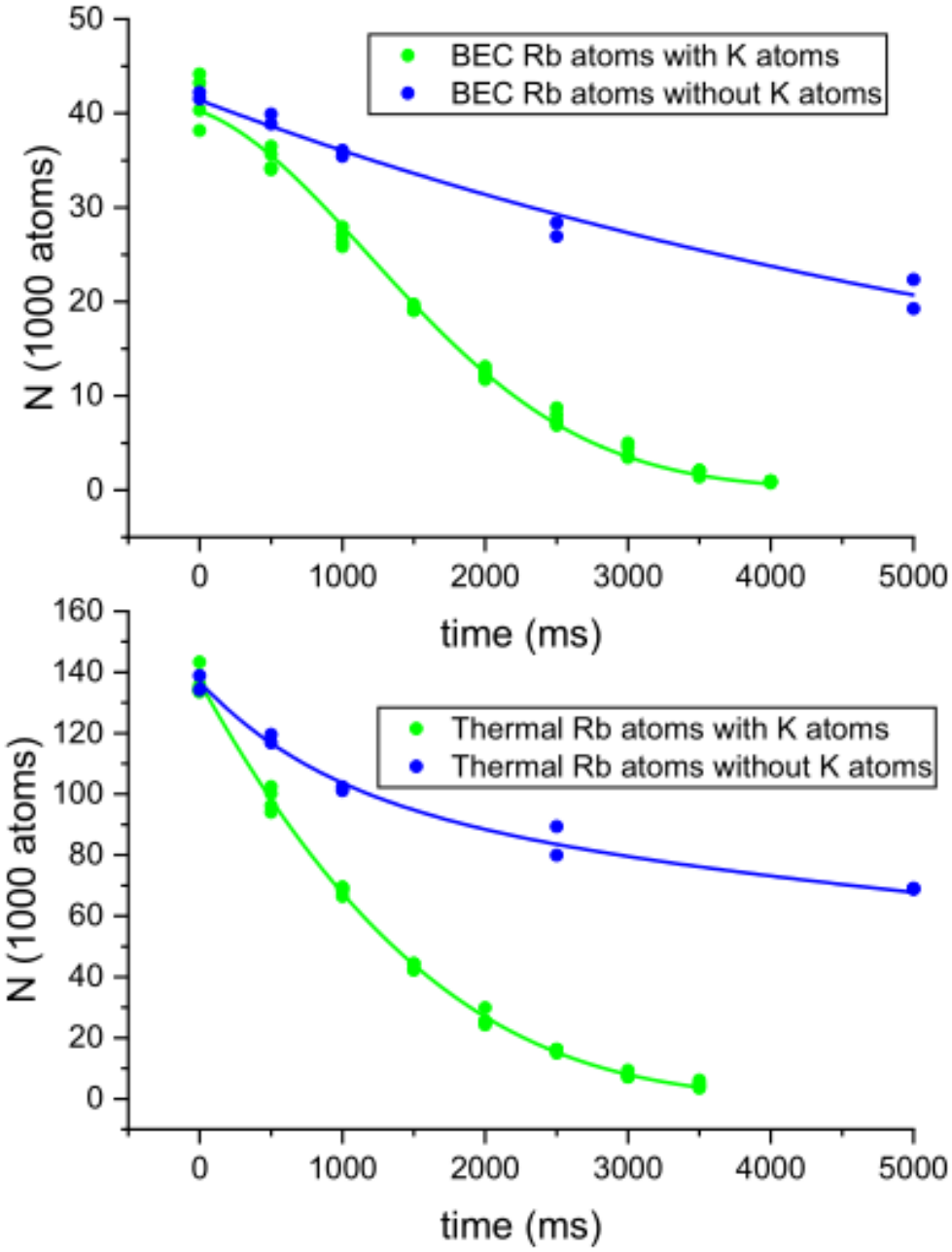


Figure 4.3: ^{87}Rb atom number as a function of time for a condensate (upper panel) and a thermal gas (lower panel). The blue points and curves correspond to the measurement without the dissipation. The green points and curves correspond to the measurement with the dissipation.

We extract γ_{Rb} from the measurement in the absence of dissipation (blue curve) and α from the measurement in the presence of dissipation (green curve). The values of γ_K

for the thermal component and the condensate are coincident to each other, which has also been shown as the blue diamonds in Fig. 4.1(b).

4.1.1.2 Systematic correction of error in data analysis

In the data analysis, the error of the thermal component is found to be always larger when the atom number is low either with or without the dissipation. Re-examining the experiment, this systematic error may come from the underestimation of the optical density for the thermal component, which is fitted by Gaussian profile. The number of atoms $N_{th} \propto A\sigma^2_{Gaussian}$ and the temperature $T \propto \sigma^2_{Gaussian}$, where A is the height of the Gaussian distribution that is proportional to the optical density, $\sigma_{Gaussian}$ is its standard deviation.

For an ideal atom gas in equilibrium, the BEC fraction as a function of the temperature can be described as

$$F = \frac{N_0}{N} = \begin{cases} 1 - \left(\frac{T}{T_c}\right)^3 = 1 - \tau^3 & \text{for} \quad T < T_c \\ 0 & \text{for} \quad T > T_c \end{cases} \tag{4.8}$$

where N_0 is the atom number of BEC and N is the total number of atoms and τ is the reduced temperature defined as $\tau = T/T_c$. $T_c = 0.94\hbar\omega N^{1/3}/k_B$ is the critical temperature, where ω is the average trapping frequency of the optical dipole trap, it is also a function of the trapping depth $\omega = \chi\sqrt{U}$. The typical value for χ is about 1/6 and due to $U = T/\xi$, where $\xi = 1/k_B$. The critical temperature and the eq 4.8 can be rewritten as $T_c = BN^{1/3}T^{1/2}$, where B is a (N, T) independent constant, and

$$\frac{N_0}{N} = 1 - \frac{T^{3/2}}{B^3 N} \implies N - N_0 = \frac{T^{3/2}}{B^3} \tag{4.9}$$

where $N - N_0$ is the atom number thermal part N'_{th}. We define the correction factor as $\Delta = N'_{th}/N_{th}$, where N_{th} is the measured atom number, we plot Δ versus N_{th}/T from the measurement with or without dissipation respectively, where $\Delta \propto A$. It has been shown in Fig. 4.4 and Fig. 4.5

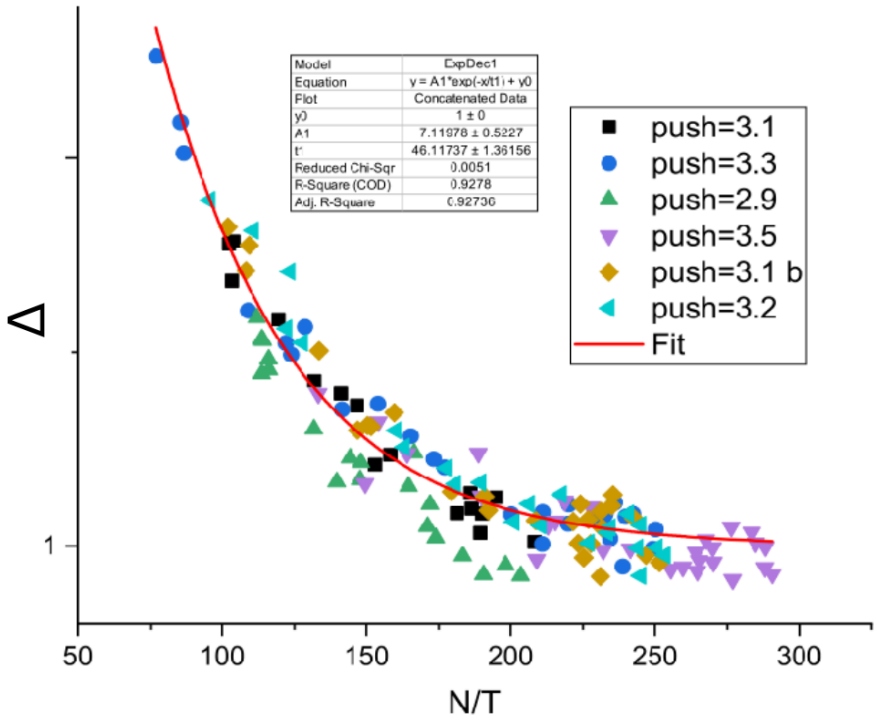


Figure 4.4: Δ versus N_{th}/T without dissipation in a viable amount of intensity of push beam for ^{87}Rb atom

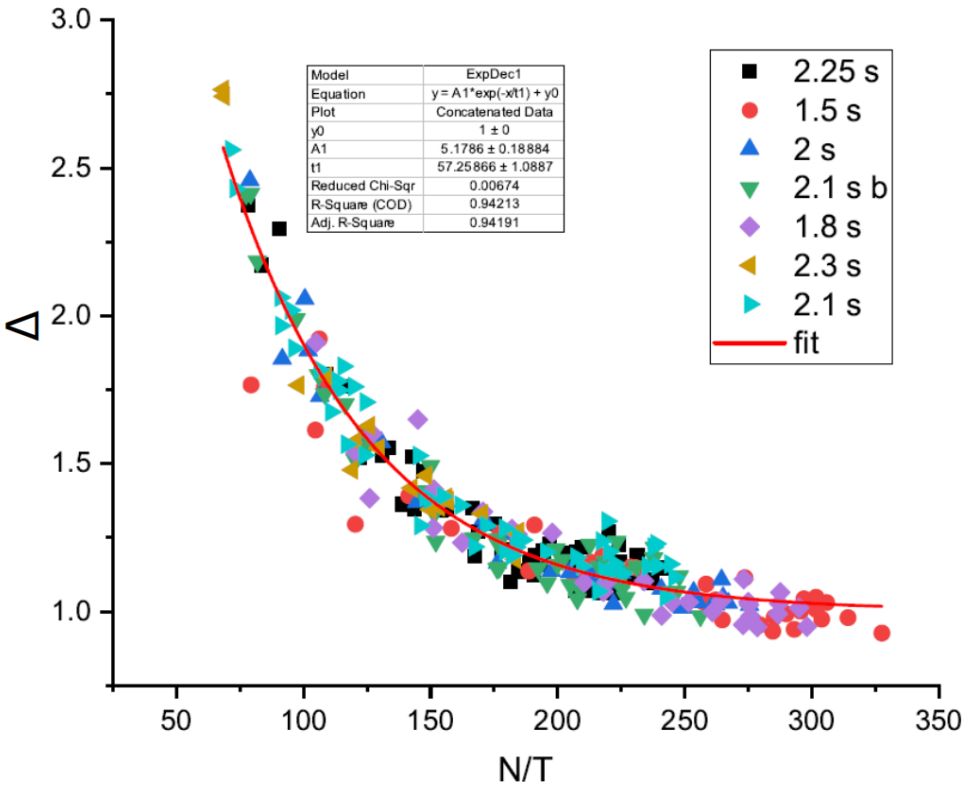


Figure 4.5: Δ versus N_{th}/T with dissipation in a viable amount of ^{39}K MOT loading time

The correction factors in the presence and absence of dissipation are are consistent after the systematic correction.

To simplify the parameters, all experimental data can be fitted by the profile

$$y = 1 - (\frac{x}{\beta})^{\alpha} \tag{4.10}$$

where $x = \frac{T^{3/2}}{N}$ and $y = \frac{N_0}{N}$. In the equilibrium, $\beta = B^3$ and $\alpha = 1$, shown as the dash line in Fig. 4.6 and 4.7. To compare the different behaviors of parameters α and β in the presence and absence of dissipation, we measure the BEC fraction evolution during the evaporative cooling without dissipation in a variable amount of intensity of the push beam which can change the number of ^{87}Rb atoms (Fig. 4.6)

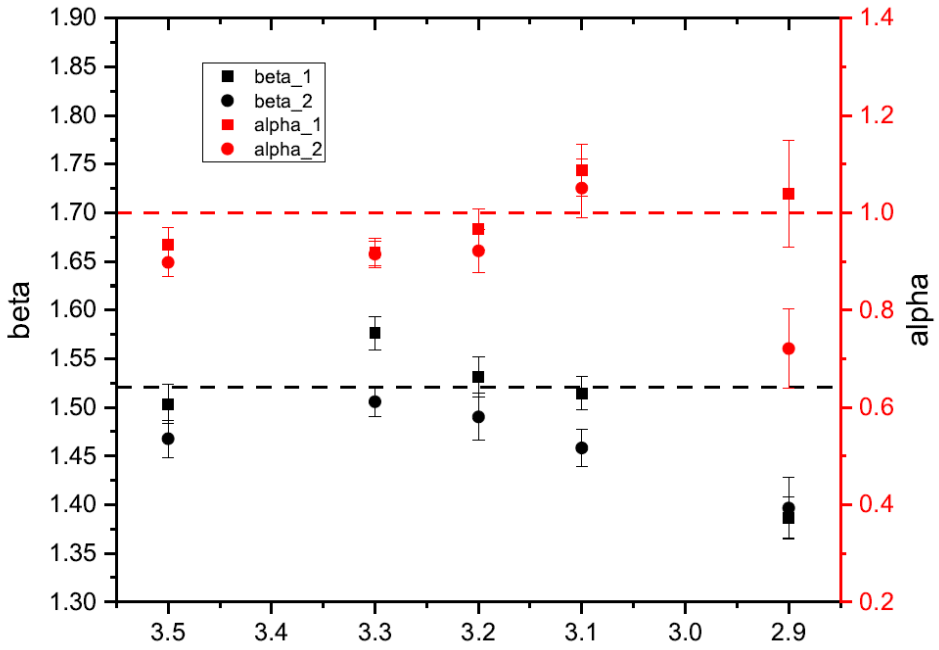


Figure 4.6: α and β without dissipation as a function of ^{87}Rb MOT push intensity. $\alpha_1\beta_1$,$\alpha_2\beta_2 are from the different datasets.$

and the fraction evolution in the presence of dissipation in a variable amount of ^{39}K MOT loading time (Fig 4.7).

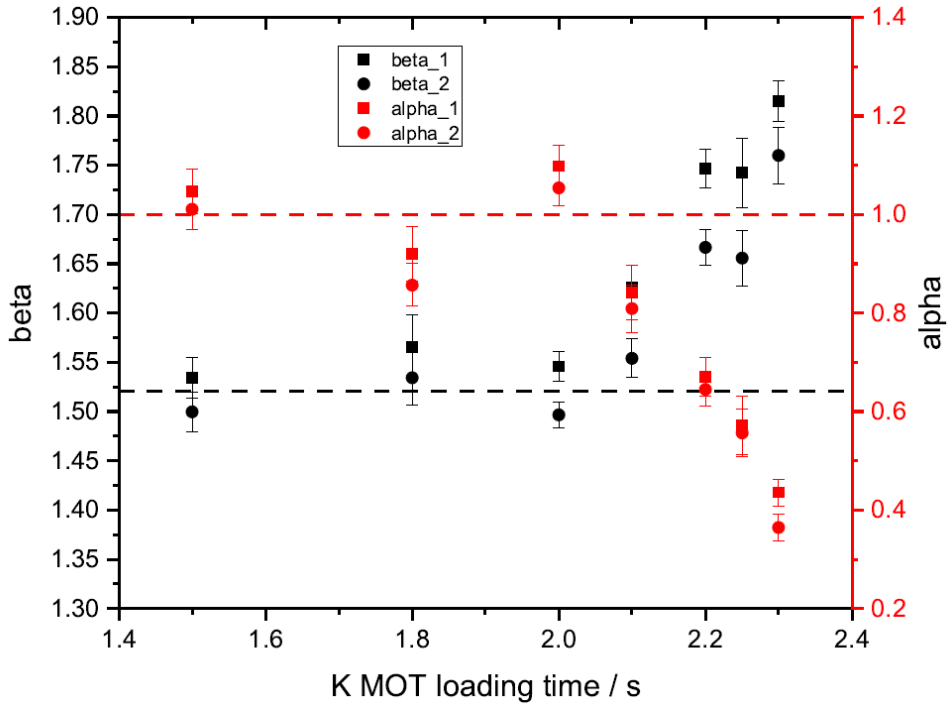


Figure 4.7: α and β without dissipation as a function of ^{39}K MOT loading time. $\alpha_1\beta_1$,$\alpha_2\beta_2 are from the different datasets.$

The deviation of the parameters in the presence of dissipation is a strong evidence that the atoms are in non-equilibrium.

4.1.1.3 Calibration of trapping frequency

Consider the influence of the inter-atom interaction on the BEC fraction, in s-wave approximation, the Eq. 4.8 can be expanded to

$$F = \begin{cases} 1 - \tau^3 - \eta\tau^2(1-\tau^3)^{2/5} & \text{for} \quad T < T_c \\ 0 & \text{for} \quad T > T_c \end{cases} \tag{4.11}$$

where $\eta = 2.15(aN^{1/6}/a_{\mathrm{ho}})^{2/5}$, a is the s-wave scattering length and $a_{ho} = \sqrt{\hbar/m\omega}$ is the harmonic trap length. During the evaporation, both of the trapping frequency and the total number of atoms is not constant [75], which lead to a reduction of critical temperature. However, due to the mild change at the end of evaporation, the Eq. 4.11 is fairly valid.

To estimate the critical temperature T_c at any time during the evaporation, we assume the geometric mean trapping frequency is ruled by $a + bt + ct^2$, where t is the evaporation time. This assumption is extracted after analysing how the power of the dipole trapping beams change with respect to time while we do the evaporation ramp. As a comparison, the trapping frequency can be also measured using the parametric heating, shown as the blue triangles in Fig .4.8.

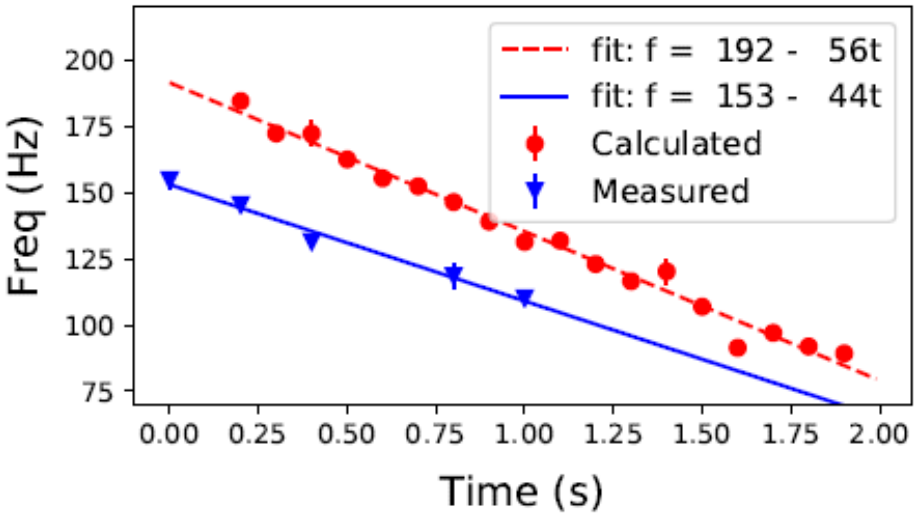


Figure 4.8: Measurement of the trapping frequency. The red dots are the mean trapping frequency $\omega/2\pi$ calculated from eq. 4.11 and the equation $T_c = 0.94\hbar\omega N^{1/3}/k_B$. The blue triangles are the mean trapping frequencies measured using parametric heating and centre of mass oscillations. The lines are linear fits to the data, the coefficients are reported in the legend. Figure and caption taken from Ref [27]

The red dots are the calculated trapping frequency based on the atom number and the temperature measurement. The red dashed line extrapolates the trapping frequency and it is referred to as calibration frequency which is using for our data analysis. To compare with the value in parametric heating measurement, the consistency can be maintained within 15%. This inconsistency can be produced from the systematic underestimation of the measured trapping frequency caused by the anharmonicities of optical dipole trap in the parametric heating measurement. On the other side, the calculated trapping frequency can be also deviated by as like e.g. the overestimation or underestimation of the atom

number and the common-mode secondary effects as discussed in the later context.

4.1.1.4 Evolution of the thermodynamics parameters and phase diagram

During the evaporative cooling without dissipation, a reduction of the BEC fraction can be observed with an increase of the reduced temperature. However, it could have inverted if accounting for the dissipation, that in turn means the parameters are quenched by the dissipation. This effect can induce a long-lived metastable state where the BEC fraction exceeds the calculated value in the Eq. 4.8. The property of this state is resemble to the superheated BEC reported in reference [17].

To switch on the ^{39}K MOT in 2s before the end of the evaporation where we set t=0, as shown in Fig. 4.1, the temporal evolution of the thermodynamics parameters during the evaporation both in the presence and absence of dissipation has been illustrated in Fig. 4.9 .

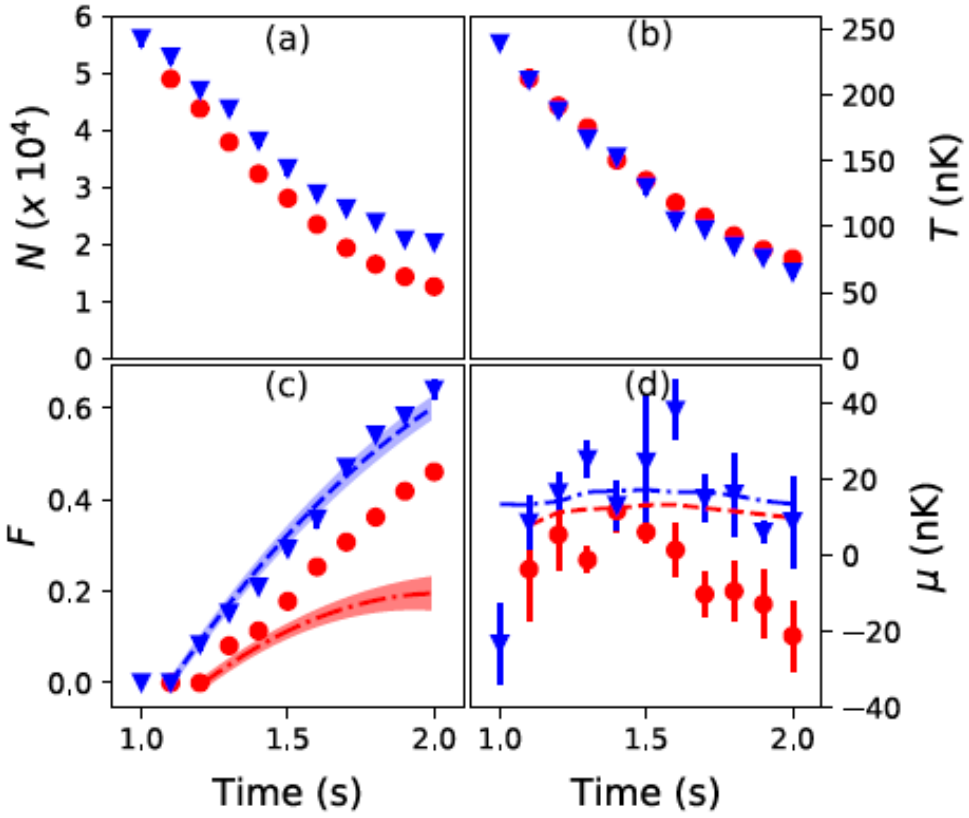


Figure 4.9: Measured parameters of the ^{87}Rb sample as a function of time. Red circles are with dissipation (distillation) and blue triangles are without dissipation. a) The total number of atoms. b) The temperature c) The condensate fraction F. The red dotted dashed line and the blue dashed line show the expected fraction from Eq. (1) for with and without dissipation respectively. d) The chemical potential of the thermal part in units of temperature. The dashed and dash-dotted lines are the chemical potential of the BEC with and without dissipation respectively. Error bars and the shaded regions are the standard errors of the mean. Figure and caption taken from Ref [27]

For a valid comparison, the data without dissipation are chosen to match the conditions with dissipation at t = 1s, right before the onset of the BEC. In the presence of the dissipation, the drop of the atom number is faster than the optimized evaporation, see Fig. 4.9(a). A crucial assumption has been put forward here is that the evaporation favors to remove the atoms with more kinetic energy from the dipole trap, in the opposite the atom loss due to the dissipation is uniform and acts equally on all the velocity classes. The

temperature can not be changed substantially by the atom loss as shown in Fig. 4.9(b), that also in turn means the thermalization of the ^{87}Rb atoms is much faster than the dissipation rate. As shown in Fig. 4.9(c), the measured (blue triangles) and calculated (blue dashed line) BEC fractions in the absence of dissipation are consistent within 5 %. However, due to the critical temperature is quenched by the dissipation, the measured fraction (red dot) is significantly higher than the calculated value (red dashed line). The BEC is substantially more pure than what can be obtained with the same atom number and temperature but without dissipation. The chemical potential of the thermal component both in the presence and absence of dissipation is shown in Fig. 4.9(d). Initially, both their trajectories approach the chemical potential of the BEC, then, in contrast to the optimal evaporation, it reduces after 1.5s in the presence of dissipation even the BEC fraction is still increasing. This strongly implies the system is not in equilibrium. Additionally, the BEC fraction as a function of the reduced temperature can be plotted by the measurement in the presence and absence of dissipation with different initial conditions or holding times, as shown in Fig. 4.10

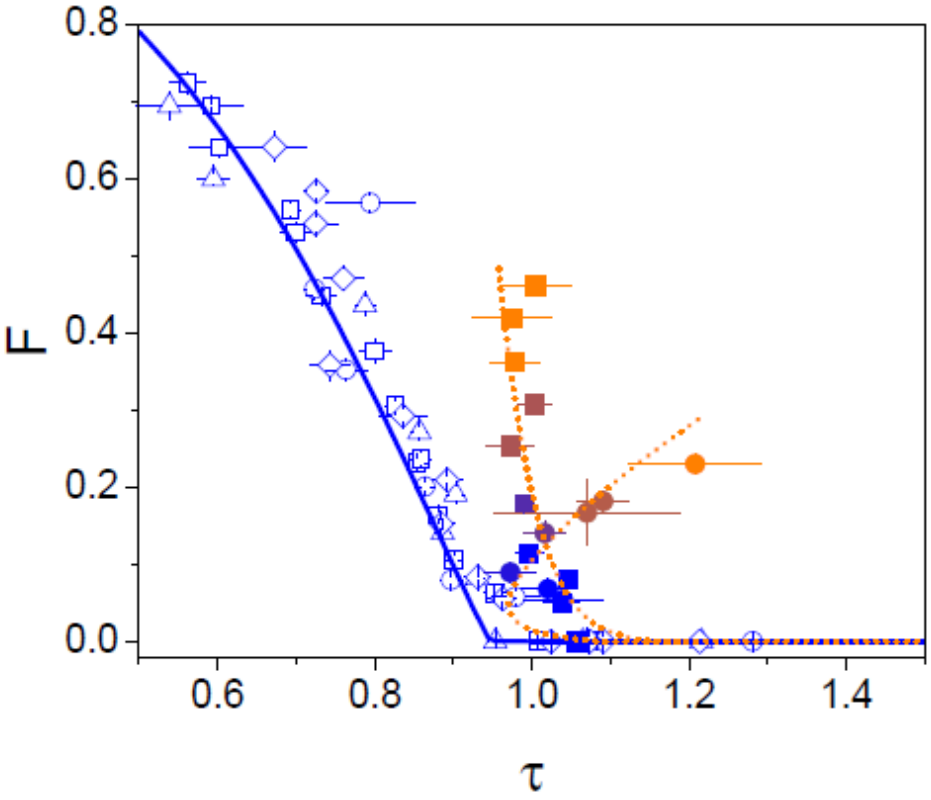


Figure 4.10: Phase diagram showing the BEC fraction as a function of reduced temperature τ. The open symbols are for the case of no dissipation while filled symbols are the trajectories during our distillation protocol. For open diamonds and circles, the wait time after the end of the evaporation ramp is 4 s, while for others it is 20 ms. For the filled circles the dissipation rate is 4 times the dissipation rate of the filled squares. For the data in absence of dissipation, we vary the number of atoms from 7×10^4 to 2.5×10^4 at t = 1s in order to explore as much parameter space as possible. The solid blue line corresponds to Eq. 4.11. The dotted lines are the results of the rate equation model described in the latter. Error bars are the standard errors of the mean. Figure and caption taken from Ref [27]

The open symbols are the results in the absence of dissipation and the solid blue curve is the prediction value from Eq. 4.8. The filling squares are corresponding to the results shown in Fig. 4.9. The presence of dissipation leads to a substantially different behavior of the trajectory, that indicates a higher purity of the condensate. As a potential application, these states can be used to investigate the phase diagram that is not accessible

in equilibrium. Here we also refer these states to as supercritical BEC.

The dissipation induce a reduction of the critical temperature duiring the evaporative cooling which results in the reduced temperature can maintain in a constant value during a continuum growth of BEC fraction to 0.5, shown as the filled squares in Fig. 4.10. In a microscopic explanation, this in turn means when the reduction of the temperature pumps atoms into the BEC, it is not able to de-pump them back into the thermal component at the same rate. Furthermore, we are also interested in to understand the thermodynamics behavior of ultracold atoms with higher dissipation rate, therefore, we strengthen the ^{39}K atom density by a factor 4 through increasing the power of the push beam. The parametric evolution is also illustrated in Fig. 4.11

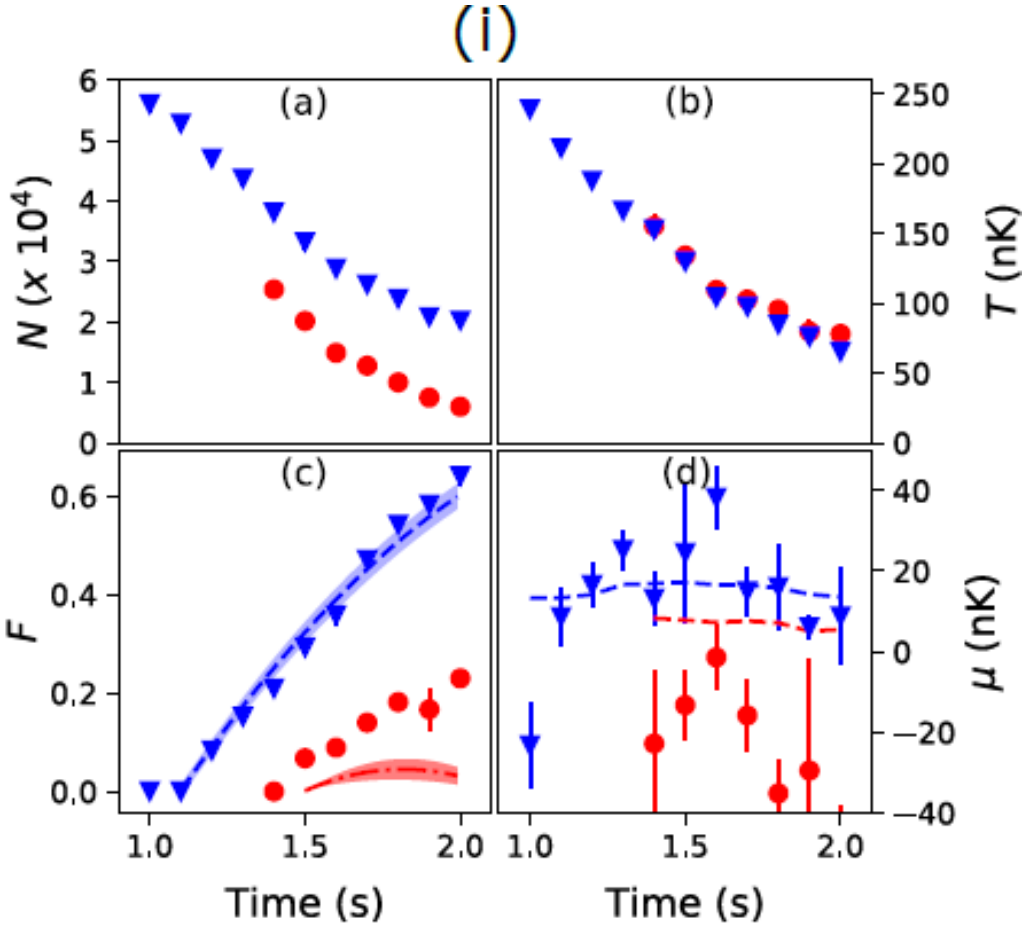


Figure 4.11: Same as the Fig. 4.9, but with the dissipation rate increased by a factor of 4, corresponding to filled circles in Fig. 4.10. Figure and caption taken from Ref [27]

Its BEC fraction evolution has already been plotted as the filling circles in Fig. 4.10. We can observe that the trajectory is inverted, the BEC fraction can be increased even with an increase of the reduced temperature.

In a summary, our results are mainly compared against the calculation in Eq. 4.11. The accuracy of the calculation is determined the experimental measurement of the atom number and the temperature. It should note that the systematic error of this calculation can be produced by several effects including the finite size effect, Bose enhancement effect, and the critical temperature change due to the inter-atom interaction.

The finite-size effect can be estimated by the equation $\delta T_c/T_c = -\bar{\omega}/2\omega \cdot \zeta(2)/\zeta(3)^{2/3} \cdot N^{1/3}$ where $\bar{\omega}$ is the arithmetic average of the trapping frequency. This deviation is less than 1% which can be safely ignored.

The BEC fraction and the temperature of the thermal component are extracted by a fitting model which is combined with a 2D Gaussian profile and a 2D Tomas-Fermi distribution in our experiment. When the temperature of the system is below the critical temperature, due to the bosonic nature of ^{87}Rb atom, the momentum distribution, to be rigorous, is an associated polylogarithm which is the so-called Bose-enhanced distribution instead of the Gaussian distribution. To illustrate in what extent this can change the data analysis, the experimental data is also fitted by a combined model of a 2D Bose-enhanced distribution and a 2D Tomas-Fermi distribution, shown in Fig. 4.12.

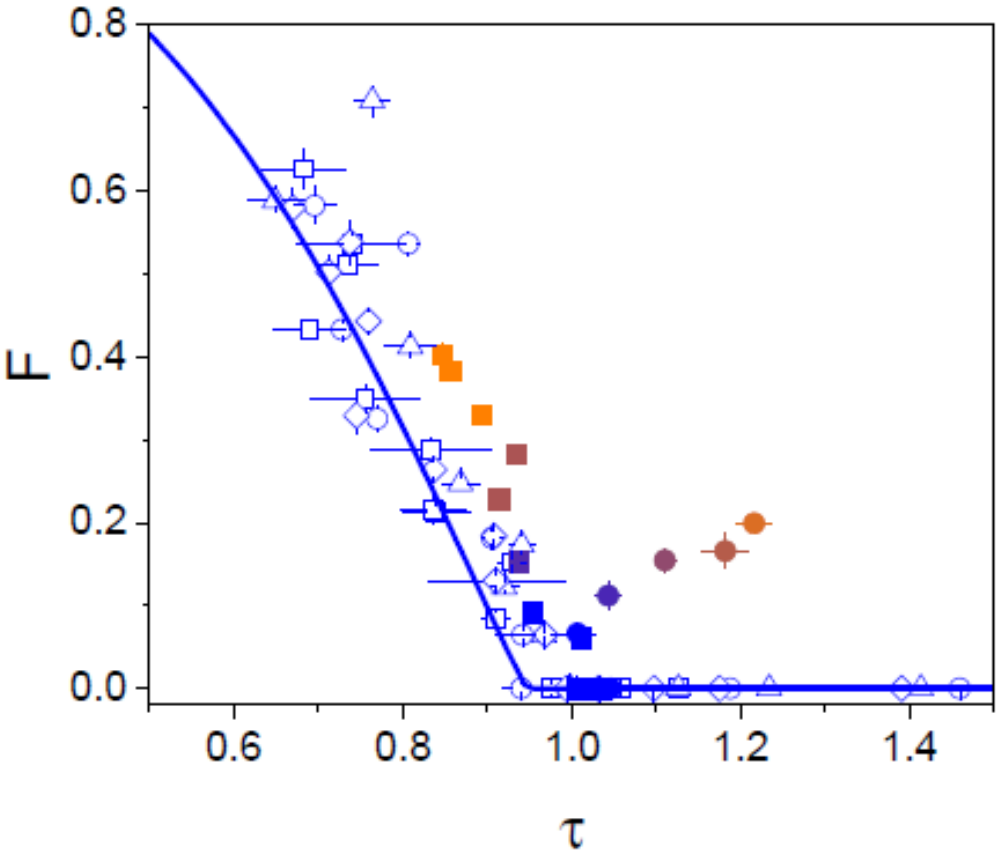


Figure 4.12: Same as Fig. 4.10 but using the Bose-enhanced polylogarithm to fit the data. Figure and caption taken from Ref [27]

To compare with the Gaussian fit in the previous Fig. 4.10, the estimation of the temperature with 2D Bose-enhanced distribution is increased by 10%. The new model can certainly enhance the accuracy of data analysis, however, an issue for the Bose enhanced fitting is due to the complexity of the polylogarithm function, the fitting curve is not convergent when the atom number of the thermal component is low, to show the whole data set is frustrated. Additionally, the new model as mentioned previously can be also absorbed by the calibration of the trapping frequency. Although the phase diagram (Fig. 4.12) has been changed, its role in physics seems not significant to reverse the conclusion made in discussion of Fig. 4.10. Therefore, we still exhibit the thermodynamics of the ^{87}Rb atoms with the Gaussian fit model.

In another concern, the Eq. 4.8 is valid as long as the interaction within the thermal cloud can be neglect, that in turn means $N_0 \gg a/a_{ho}$. It corresponds to $N_0 \gg 1000$ in our

experiment. This condition holds for most of our experimental data set. The reduction of critical temperature, $\delta T_c/T_c = -1.3a/a_{ho}N^{1/6}$ is never above 3%.

4.1.2 Relaxation towards equilibrium state

Another property of the supercritical state we focus on is its relaxation. In the measurement, the state is held in the dipole trap with a constant potential depth in a variable amount of time in the absence of dissipation. The differences between the measured BEC fraction and the counterpart value in Eq. 4.8 δF have been plotted as a function of the holding time in Fig. 4.13.

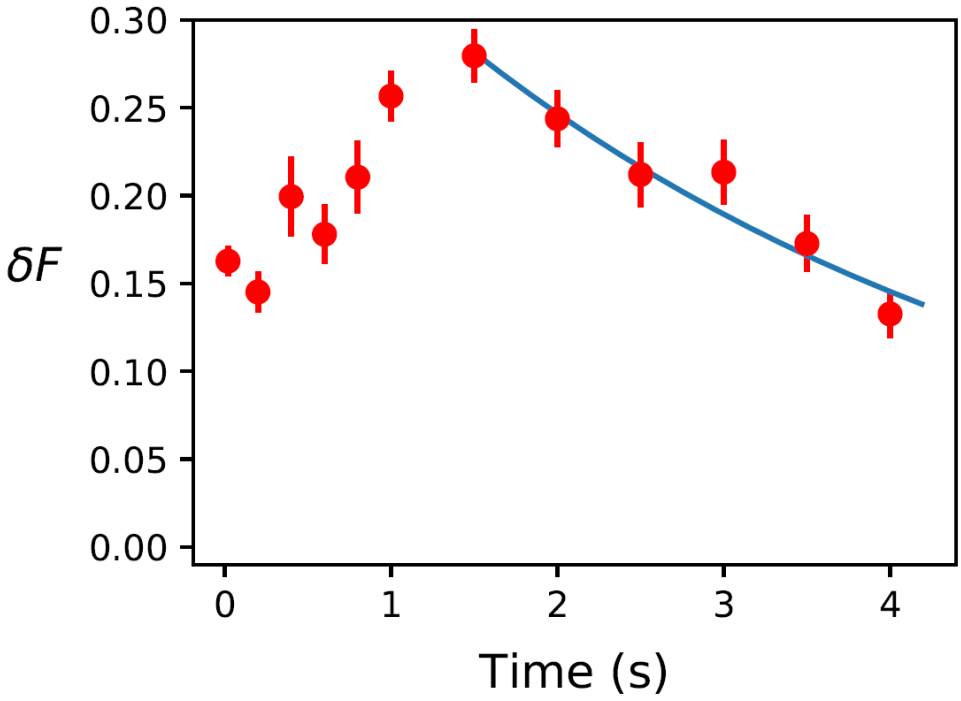


Figure 4.13: Difference between the measured F and that expected using Eq. (4.8) after the dissipation from the ^{39}K MOT is switched off and the sample is held with constant trap depth. Error bars are the standard errors of the mean. The line shows an exponential fit to the data after 1.5 seconds, when the supercritical gas relaxes towards equilibrium. The time constant is 3.9 ± 0.3 s. Figure and caption taken from Ref [27]

In this process, the temperature of the atoms is continually reduced slowly through

the rethermalization but the trapping frequency does not change in a constant dipole trap. We can observe the system still evolves to even further out-of-equilibrium in 1.5s after the dissipation and then relax back to equilibrium. As long as we can measure in the experiment, δF moves to zero has never been seen. Comparing to the typical time scale of the experiment, which is usually in the order range from 0.1ms to 100ms, the relaxation dynamics can be considered as quasi-static. A state with this property is also referred to as prethermalized state.

4.1.3 Modeling the system

Due to the complexity of the thermodynamics, an exact microscopic quantitative theory of out-of-equilibrium that governs the growth of the condensate still has not been seen. Some simplified theoretical models by put forward of the assumptions as constant temperature and infinite atom reservoir have been reported in references [76, 77], however, in some cases the parameters need to be adjusted up to one order of magnitude. It seems more challenging to describe a system in presence of the evaporation and of the dissipation with a microscopic theory. As a compromise, unlike the rigorous treatment, we develop a phenomenological two-mode rate equation model to explain our experimental results. This method has been discussed in several references [17, 76–78]. We hope it may provide useful information for the further works on a more rigorous model.

In our model, the two modes are the condensed component and the thermal component. We indicate N_0, N_{th} as the atom number in the condensate and of the non-condensed atoms. As shown in Fig.4.14, the starting point of our model is to separate the sample into the ground state energy level ϵ_0 (the condensate) and the energy levels directly above it (the thermal component). Then, the energy band above the condensate is simplified to a single effective energy level ϵ_{th}. Rigorously, ϵ_0 is determined by the time-dependent chemical potential of the BEC and ϵ_{th} is also dynamically influenced by the condensate growth. However, to understand the time-dependent of the energy levels is a challenging task and goes beyond our research scope. We address our problem in a time-independent

approximation structure.

The growth rate for a certain energy level in the absence of dissipation has been developed in references [76–78]:

$$\dot{N}_n = W(N)[(1 - e^{(\epsilon_n - \mu_e)/k_B T})N_n + 1] \tag{4.12}$$

where N_n is the population of the energy level n, ϵ_n is its energy, μ_e is the chemical potential in equilibrium and W(N) is the growth coefficient. For the condensed state, the exponential implies that the steady state can be reached when the chemical potential of the condensate equals the chemical potential in equilibrium. To simplify the model, the approximation of the energy levels ϵ_n are time independent has been made. With this assumption to account for the reaching of the steady state in absence of dissipation, the exponential term in Eq. 4.12 is replaced by a term t/t_f, where t_f is the time when it reaches the steady-state of all the atoms are in the BEC. This model has been shown in Fig. 4.14

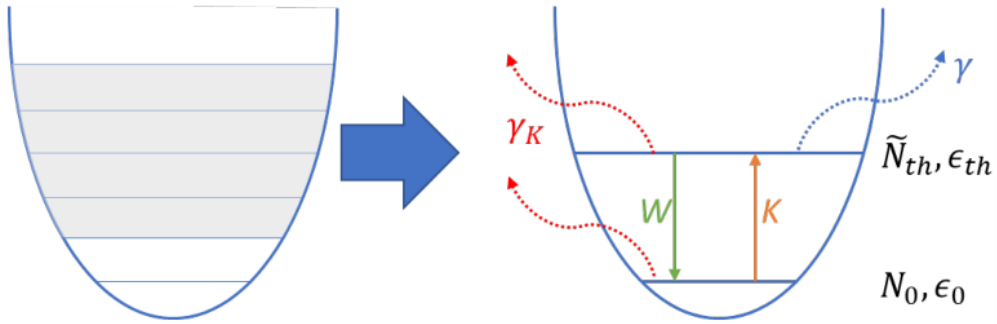


Figure 4.14: Pictorial representation of our rate equation model. Figure and caption taken from Ref [27]

With this approximation, the rate equation for the two modes can be re-written as

$$\begin{aligned}\dot{N}_0 &= \bar{W}\left[\left(1-\frac{t}{t_f}\right)N_0+1\right]-\bar{K}(\tilde{N}_{th}+1)-\gamma_K(t)N_0\\ \dot{N}_{th} &= -\bar{W}\left[\left(1-\frac{t}{t_f}\right)N_0+1\right]+\bar{K}(\tilde{N}_{th}+1)-[\gamma_K(t)+\gamma]N_{th}.\end{aligned} \tag{4.13}$$

this is valid if $t \leq t_f$, where γ_K is the dissipation rate from the ^{39}K MOT and γ is the dissipation rate due to the evaporative cooling. The effective number of thermal atoms $\tilde{N}_{th}$ accounts for the reduction of the non-condensed energy band to a single state. In principle, if such simplified state is populated by N_{th} atoms, the bosonic stimulation should be enhanced by a factor N_{th}. However, the non-condensed energy band is not uniformly populated and in this band more energetic particles are less involved in the exchange of particles with the condensate. This effectively reduce the bosonic stimulation, however it is difficult to be evaluated. Therefore, $\tilde{N}_{th}$ is used as a free time-independent fit parameter in our model.

In general, W and K should be complicated functions of T, μ, N_0, and N. The relations exhibited in Eq. 4.13 are only valid when the temperature is constant and the atom number in the reservoir is infinite and even it is valid the calculation for W and K, can be still wrong up to an order of magnitude. In our model, we drop these functions to average constants $\bar{W}$ and $\bar{K}$, the growth of the condensate can be explained as a result of the unbalanced two-body scattering without the creation or absorption of quasi-particles. According to the first-order treatment for a uniform Bose gas with contact interactions, for $\tau \leq 1$, the energy of the ultracold atoms can be described as

$$E = \sum_p \frac{p^2}{2m} + \frac{4\pi\hbar^2 a N^2}{mV}\left(1-\frac{1}{2}F^2\right) \tag{4.14}$$

where a is the s-wave scattering length and V the trapping volume. When an atom leaves the condensed phase, the energy change $\Delta = 2\pi\hbar^2 a N_0/mV$ yields an imbalance

between $\bar{W}$ and $\bar{K}$.

$$\bar{W} \simeq \exp(\Delta/k_B T)\bar{K} \tag{4.15}$$

Where Δ is referred to as energy gap between the two components. Eq. 4.15 means that for a given temperature, a larger energy gap favors to pump an atom into the condensate and in the opposite frustrates to excite an atom to the thermal component. This makes it possible to drive the system to out-of-equilibrium.

In summary, to compare with the other models, our model is a simplified version in the absence of dissipation, it maintains the core features include:

(1) the separation of the condensed and thermal components.

(2) The bosonic stimulation, i.e., the fact that if N bosons occupy the given state, the transition rates into that state are proportional to (N + 1)

(3) W and K are imbalanced.

(4) the growth of the BEC slow down and eventually stops when it reaches equilibrium. In reference [76–78], the growth rate scales as the exponential term $e^{(\epsilon_n-\mu_e)/k_B T}$, which stops once $\epsilon = \mu_e$, This term is replaced by the linear function of t/t_f in our model and we have verified this simplification does not change the behavior of the model substantially.

The main modifications we have made are:

(1) We have dropped the functional dependence of the coefficient W and K to consider them as constants. This is because, from previous comparisons of the model with experimental data, it was found that the coefficients calculated in references [76–78] could be wrong up to one order of magnitude. This modification is valid due to the coefficient K doesn't change substantially to the first order if $\mu \ll k_B T$ and the W is only determined by the elastic collision rate and doesn't change substantially in our experiment.

(2) We consider the non-condensed component as a single energy level with an effective population $\tilde{N}_{th}$ instead of an energy band and remove the time-dependence of the energy levels. This simplification is dictated by the lack of a sufficiently precise microscopic model.

(3) We also add the dissipative terms γ_K and γ to the model. Concerning the data in Fig. 4.9, we derive the $\bar{W}$ by fitting the curve $N_0(t)$ in the absence of dissipation with the solution of

$$\dot{N}_0 = \bar{W}\left[\left(1 - \frac{t}{t_f}\right) N_0 + 1\right] \tag{4.16}$$

with t_f=1.4 s, the time at which the evaporation ends (please note the origin of time is shifted by 0.6s in this data analysis), obtaining $\bar{W}$ = 3.45±0.1 Hz. Then We derive $\bar{K}$= 0.255±0.03 Hz from an exponential fit of the relaxation curve in Fig. 4.13. The evaporation loss rate γ = 0.95±0.03 Hz is obtained by fitting with an exponential the decay of the total atom number in absence of dissipation. And the $\gamma_K(t)$ has already been extracted in Fig. 4.3. The only free parameter of our model is $\Xi = N_{th}/\bar{N}_{th}$, which determines the effective occupation of the thermal energy band. We found that we can reproduce our data by imposing Ξ= 25 ± 5, as shown in Fig. 4.15.

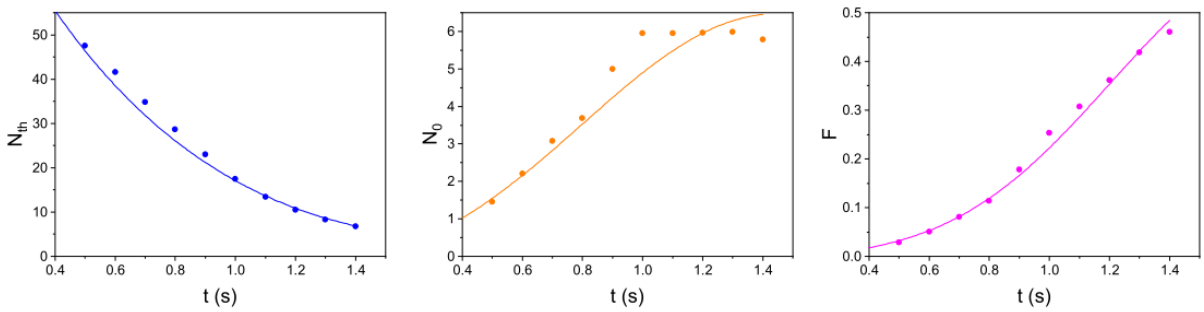


Figure 4.15: From left to right, evolution as a function of time of the atom number (in thousands) in the thermal component, the atom number in the BEC (in thousands) and the condensate fraction F. The points are the experimental data, the line are the results of our model. Figure and caption taken from Ref [27]

The result of our model is also reported as the dotted trajectory in Fig. 4.10. By increasing the dissipation rate γ_K by a factor of 4, leaving all the other parameters unchanged, the second trajectory can be depicted which reproduces the open circle data well in Fig. 4.12. In a word, our data can be nicely reproduced using our our model with a constant value for Ξ, however it could not be extended to describe other kind of

experiments, e.g. a quench in the atom number requires to implement a time dependence on Ξ.

4.2 Vortex conveyor belt for matter-wave coherent splitting and interferometry

As mentioned previously, in the first year of my Ph.D, we also cooperate with a former member of our group, Dr. Jixun Liu, to complete a theoretical work on atom interferometry. In this section, I will illustrate the main idea of this work.

The atom interferometer has been commonly used as a quantum technique in many areas, such as the fundamental physics constant measurement [79], the test of the equivalence principle [80, 81] and the detection of the gravity wave measurement [82, 83]. An extraordinary application of the atom interferometer is to measure the acceleration and rotation [84]. It can be used for navigation and geophysics surveys. As the same as the optical interferometer, the matter-wave can be also coherently split and recombined, that has been reported being achieved by using micro-fabricated gratings [85], Bragg scattering [86, 87] and Kapitza-Dirac scattering [88, 89]. Nowadays an pioneer experiment using a free-falling atom interferometer [90] can reach the accuracy to the level up to 3.9 μ Gal in the recent record [91], in excess of the other state-of-the-art techniques. However, it is challenging to make further improvements of the accuracy. The major obstacle is the growth of the interrogation time of the system. In the conventional atom interferometer, the atom trajectory only can be occasionally bent by an external field. The acceleration is extracted from the measurement of the phase difference between the atomic matter waves in two different paths. The time of atom motion from launch to recombination in the two paths is defined as interrogation time. It scales as the transmission distance of the atom beams. For example, to achieve a free-falling system with 2.3s interrogation time requires the length of the vacuum enclosure in the order of 10m [92].

Thanks to the developments of the atom confinement and atom cooling, a trapped

and guided atom interferometer is possible to be achieved by applying proper external potentials [93, 94]. The main advantage of this system is the atoms are allowed to be directed to a more complex trajectory promising a longer interrogation time. Besides, it provides a possibility to control the atoms in a size smaller than the de Broglie wavelength. In our work, a BEC sample is considered due to its macroscopic phase coherence. The BEC can be split by deforming a single-well potential to a double-well potential and maintains still coherent in this two potential wells. In fact, many ways can be used to realise this in experiment such as changing the optical trap [95], applying radio-frequency [93] and microwave fields [96]. Here, we consider to control the phase of the BEC by the imprinting from a SLM, where the phase modulation is considered within the column density [97, 98]. In practice, we create two opposite velocity fields on the two halves of a trapped BEC through the phase imprinting. The evolution of the BEC is simulated and shows that a string of vortices arises along the central line of the BEC and these vortices effectively act as a conveyor belt to move the atoms on its two sides in opposite directions. The BEC is coherently split into two parts and forms an interference pattern after a half oscillation recombined in the center. As a result, the phase of the interference fringe can be used to measure the external acceleration. The potential use of this system as a new generation of the atom interferometer has been clearly demonstrated.

As mentioned above, with the mean-field approximation, a trapped BEC can be described by the Gross-Pitaevskii equation,

$$i\hbar\partial_t\phi(\vec{r},t) = (-\frac{\hbar^2\nabla^2}{2m} + U(\vec{r}) + \xi|\phi(\vec{r},t)|^2)\phi(\vec{r},t) \tag{4.17}$$

where the order parameter $\phi(\vec{r},t)$ can be written as

$$\phi(\vec{r},t) = \sqrt{n(\vec{r},t)}e^{iS(\vec{r},t)} \tag{4.18}$$

where $n(\vec{r},t)$ and $S(\vec{r},t)$ are the density distribution and the phase distribution of the condensate respectively. The velocity of the superfluid can be fixed by the gradient of

$S(\vec{r},t)$,

$$v(\vec{r},t) = (\hbar/m)\nabla\vec{S}(\vec{r},t) \tag{4.19}$$

Modulating the external optical potential can provide the spatial and temporal control of the velocity of the superfluid. In the presence of a spatially varied external potential, the phase of BEC can be described as $S(\vec{r},t) = U(\vec{r})\tau/\hbar$, where τ is the exposure time of the imprinting laser.

In an optical dipole trap, the trapping frequencies of the BEC are $\omega_x, \omega_y, \omega_z$. We assume the imprinting laser is propagating in the z-direction and the trapping frequencies are designed as $\omega_z \gg \omega_x, \omega_y$. In this case, we can expect the BEC has a pancake shape. We exhibits the distance in the unit of the harmonic oscillator length $a_{ho} = \sqrt{\hbar/m\omega_{ho}}$, time in the unit of $\omega_{ho}^{-1} = (\omega_x\omega_y\omega_z)^{-\frac{1}{3}}$ and the energy in the unit of $\hbar\omega_{ho}$. We set the initial conditions of the simulation as 3×10^4 ^{87}Rb atoms with the trapping frequency $\omega_x = \omega_y = 0.06\omega_z$. The spatial distribution of the phase of the BEC can be described as

$$\phi_1(x,y) = \begin{cases} -2\pi y/l & \text{if} \quad x < 0 \\ 2\pi y/l & \text{if} \quad x \geq 0 \end{cases} \tag{4.20}$$

at t=0. We solve the Eq.4.17 using a standard split-step Fourier algorithm. The phase pattern has been shown with the velocity of the superfluid in Fig. 4.16(a) and Fig. 4.16(c).

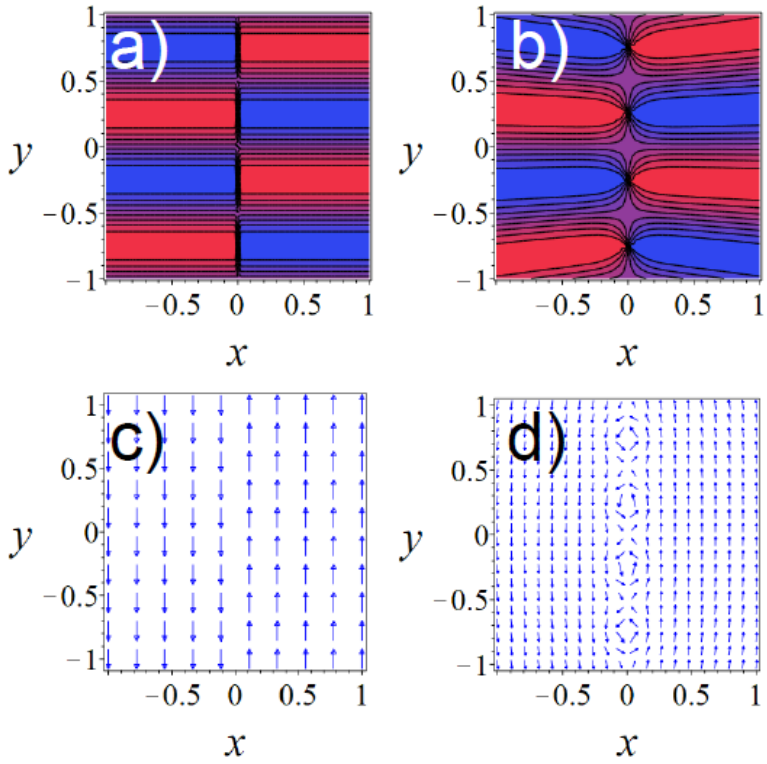


Figure 4.16: a) Phase pattern resulting from the imprinting of Eq. 4.20 with l = 1. b) Phase pattern generated by Eq. 4.21 with d = 0:25. c) and d) are the corresponding velocity fields. Figure and caption taken from Ref [28].

Where the velocity field is the derived gradient of the imprinting phase, it has two opposite constants on the two halves of the condensate within the phase pattern 4.16(a). As a result, the dynamics of the column density distribution of the BEC has also been shown in Fig. 4.17

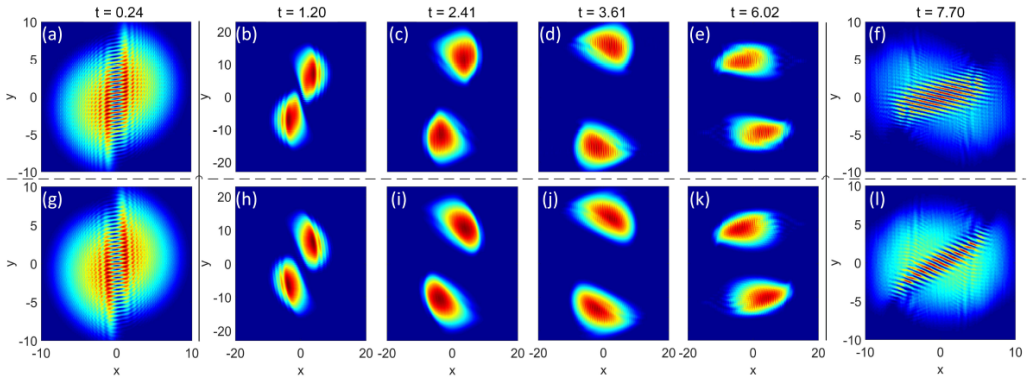


Figure 4.17: Column density profiles of the BEC at different evolution times t after the phase imprinting. (a)-(f) shows the dynamics after the imprinting of Eq. 4.20, while (g)-(l) of Eq. 4.21 Note that for t=0.24 and 7.7 the axis range is reduced to better show the initial formation of the vortex conveyor belt and the final interference patterns. Figure and caption taken from Ref [28].

Due to the phase pattern with being a period of l in the y-axis and a jump when passing across x=0, the uniform density distribution of BEC rapidly decays into a regular line of vortices pinned at x = 0 and separated by l/2. The vortex line behaves as a conveyor belt for the matter-wave, launching the two halves of the BEC in the opposite directions. Then, the trap potential pull the BEC back to the center, the two separated parts recombine after a half oscillation. A clear interference pattern of the density distribution can be observed during this recombination. Fitting the interference by a distribution combined with the Gaussian profile and the sine function, the phase of the interference fringe α can be extracted. Additionally, to expand the understanding of the splitting and launching action of the conveyor belt and the relation of the imprinting phase pattern and the overall dynamics, we imprint another pattern followed by Eq 4.21 on the BEC,

$$\phi_2(x,y) = \sum_{k=1}^{N} 2(arctan\frac{y+(2k-1)d}{\sqrt{x^2+(y+(2k-1)d)^2}+x} + arctan\frac{y-(2k-1)d}{\sqrt{x^2+(y-(2k-1)d)^2}+x}) \tag{4.21}$$

where N is an integer, and d is a positive constant. This phase pattern can create singly quantized vortices along the x = 0 line with an initial distance of 2d between them. We notice that if d=l/4, the velocity field is similar to the one without quantized vortices when | x | is much higher than the healing length. However, when the x close to 0, the phase pattern resulting from ϕ_2 is clearly distorted and intrinsically presents vorticity. These behaviors have been shown in Fig. 4.16(d). Where the initial exit velocities along the y-direction v_y are traced to compare with in the presence of phase pattern ϕ_1 or ϕ_2. In the ϕ_2 case, the motion of the centre of mass of two clouds in Fig. 4.17 is fitted by a 2D Gaussian model. Due to the atom clouds are confined in optical dipole trap, the motion of the centre of mass can be described by a cosine function. The exit velocities in the ϕ_2 case are exhibited in Fig. 4.18 as the blue circles and red squares.

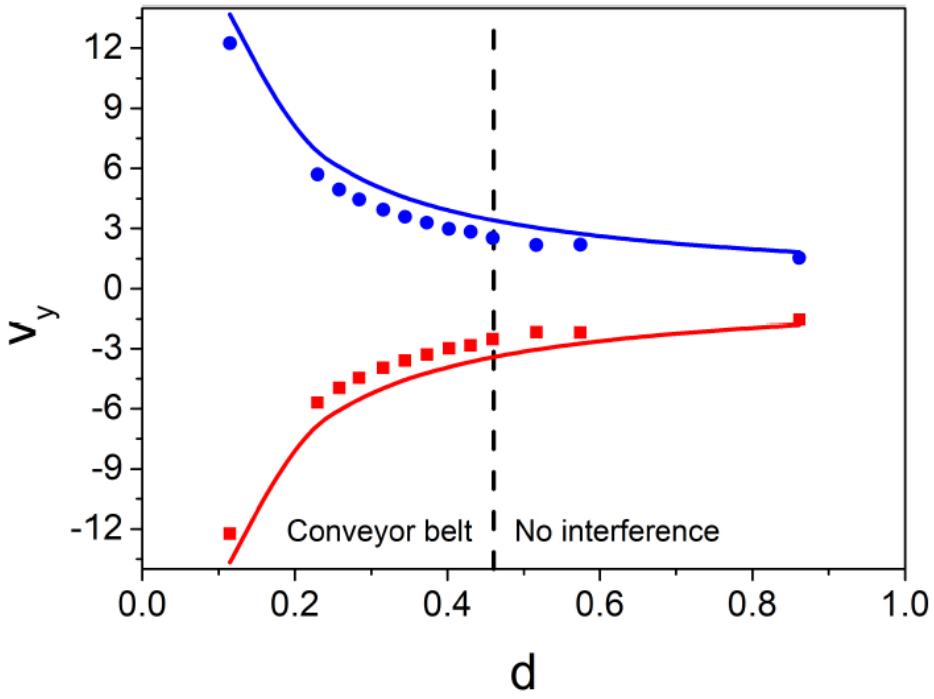


Figure 4.18: Initial exit velocity along the y-axis v_y vs. half initial vortex distance d after the imprinting of the pattern in Eq. 4.21. The blue circles and the red squares represent the values obtained by fitting the simulated density profiles with the procedure explained in the text. The solid lines are calculated with $v_y = d\phi_1/dy$ with l = 4d. Figure and caption taken from Ref [28].

We also plot the exit velocities from the phase pattern ϕ_1: $v_y = d\phi_1/dy$ within l = 4d as the red and blue curves in Fig. 4.18. The discrepancy between the velocities being observed with the two patterns is from the distortion of the phase pattern ϕ_2. From Fig. 4.18, either in ϕ_1 or in ϕ_2, it can be confirmed that the initial vertex distance increases with the injected energy being decreasing. One should note that when the vertex distance $d \geq 0.46$, the coherence is broken down, the interference pattern of the two halves BEC can no longer be observed.

Measuring the inertial force is the major application of an interferometer, the trapped interferometer is expected to strengthen the sensitivity of this measurement. In our simulation, to illustrate the potential of this system as an acceleration meter, we plot

the phase of the fringe α (from Fig. 4.17) as a function of the acceleration β in a varied amount of the injected velocities in Fig. 4.19 (We assume the constant acceleration β is towards the negative direction of the y-axis.)

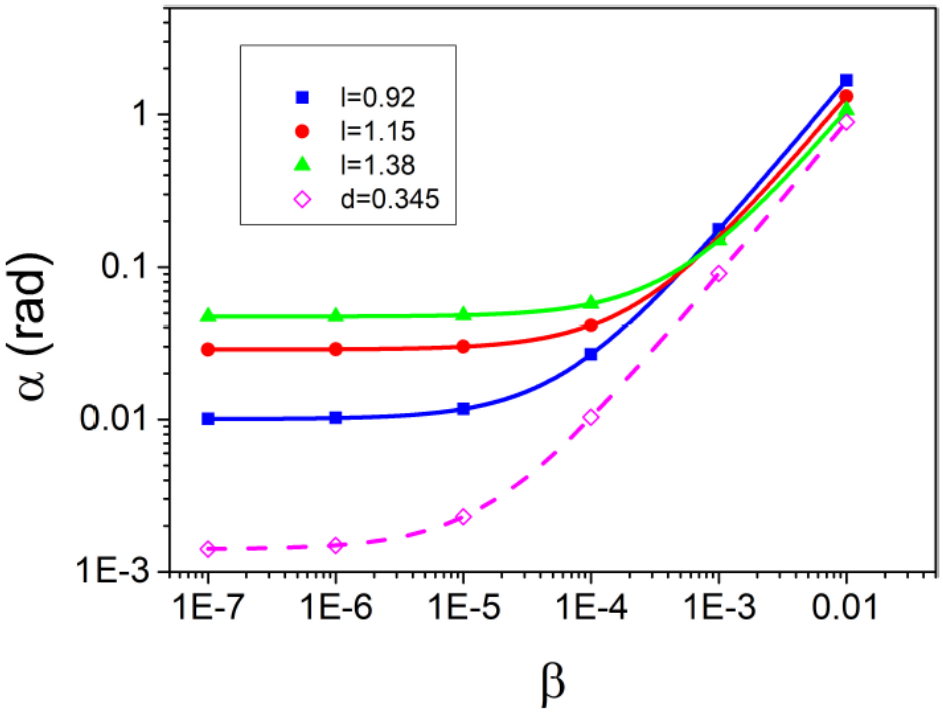


Figure 4.19: Phase of the interference fringe α vs. acceleration β for different values of the phase imprinting coefficient l or d. The filled symbols are the results of the numerical simulations after imprinting the pattern in Eq. 4.20. The solid lines are linear fits to the data. The open points are data extracted from the simulations resulting from the imprint of Eq. 4.21. The dashed line is the corresponding linear fit. Figure and caption taken from Ref [28].

The sensitivity of the accelerometer is given by the slope of the fitting lines. It can be increased by decreasing l. For a high acceleration, the system imprinted by phase pattern ϕ_2 is compatible with one imprinted by phase pattern ϕ_1. However, its sensitivity is reduced by 10% when the acceleration is low. To give an example, the sensitivities of the curves in Fig. 4.19 range from 1 10^5 μ Gal, when we set the trapping frequencies of the optical dipole trap to (ω_x, ω_y, ω_z)=2π (15, 15, 250) Hz.

Chapter 5

Conclusions and Further Remarks

The majority of this thesis was devoted to experimental research on non-equilibrium quantum thermodynamics using ultracold atoms. The experimental apparatus designed to capture the two species of atoms from the background gas and implement efficient laser cooling has been illustrated. A dissipative distillation of a supercritical quantum gas has been observed in our experiment. Specifically, a ^{87}Rb BEC with 1×10^5 atoms is produced after all-optical evaporative cooling and then immersed in a ^{39}K MOT. The collisions between the two atomic species, which have a temperature difference of four orders of magnitude, results in the losses of ^{87}Rb atoms from the BEC. The dissipation rate caused by the ^{39}K MOT is way less than the intra-species collision rate of the ^{87}Rb atoms. Therefore, the system can be always kept in thermal equilibrium, but the kinetic equilibrium cannot be preserved during the evaporation. This in turn means the chemical potentials of the thermal component and the condensed component are imbalanced. As a result, a metastable state can be produced with a finite BEC fraction when the temperature is above the critical temperature in non-equilibrium. Additionally, the relaxation property of this state is also investigated, demonstrating the lifetime is longer than the typical experimental time scale (0.1ms to 100ms). Consequently, this state can be potentially used as a novel tool to distillate environmentally resilient states and engineer quantum phases in open quantum system. To understand these thermodynamics at the

microscopic level, we also provide a phenomenological model, although this explanation is not rigorous, it may trigger the development of the microscopic theory of quantum gases in non-equilibrium.

For our other research goal, to engineer a single-atom quantum heat engine, an experimental apparatus to trap the single ^{41}K atom has been designed which will be immersed in an ultracold ^{87}Rb atoms in the future work. This apparatus is still under construction. Once achieved, the ^{41}K atom will act as the working fluid and the ^{87}Rb atoms will play the role of the thermal bath in thermodynamics transformations. The inter-species interaction will be used to manipulate the heat exchange between the working fluid and the thermal bath and the optical potential of the tweezer will be used to implement the state density compression. The energy level of the ^{41}K atom in the optical tweezer will be measured by Raman side-band spectroscopy.

The other result of my PhD, the numerical study of a matter-wave interferometer realised by splitting a trapped Bose-Einstein condensate with phase imprinting has been also discussed. I illustrate a simple step-like imprinting pattern can cause the BEC to form a string of vortices and then the two halves of the condensate launch with opposite velocities. The whole evolution of the BEC from launching to recombining resembles the one of a conveyor belt and the initial exit velocity along the vortex conveyor belt can be controlled continuously by adjusting the vortex distance. At the of this work, I resolve the correlation between the interference fringe and the external acceleration. Its potential application as a compact accelerometer has been clearly illustrated.

References

(1) Brandner, K.; Saito, K. *Physical Review Letters* **2020**, *124*.

(2) Carollo, F.; Gambetta, F. M.; Brandner, K.; Garrahan, J. P.; Lesanovsky, I. **2019**.

(3) Goold, J.; Huber, M.; Riera, A.; Del Rio, L.; Skrzypczyk, P. *Journal of Physics A: Mathematical and Theoretical* **2016**, *49*, 143001.

(4) Quan, H. T. *Physical Review E* **2009**, *79*, 041129.

(5) Popescu, S.; Short, A. J.; Winter, A. *Nature Physics* **2006**, *2*, 754–758.

(6) Vinjanampathy, S.; Anders, J. *Contemporary Physics* **2016**, *57*, 545–579.

(7) Scully, M. O.; Zubairy, M. S.; Agarwal, G. S.; Walther, H. *Science* **2003**, *299*, 862–864.

(8) Roßnagel, J.; Abah, O.; Schmidt-Kaler, F.; Singer, K.; Lutz, E. *Physical review letters* **2014**, *112*, 030602.

(9) Carollo, F.; Gambetta, F. M.; Brandner, K.; Garrahan, J. P.; Lesanovsky, I. *Physical Review Letters* **2020**, *124*, 170602.

(10) Klatzow, J.; Becker, J. N.; Ledingham, P. M.; Weinzetl, C.; Kaczmarek, K. T.; Saunders, D. J.; Nunn, J.; Walmsley, I. A.; Uzdin, R.; Poem, E. *Physical Review Letters* **2019**, *122*, 110601.

(11) Brantut, J.-P.; Grenier, C.; Meineke, J.; Stadler, D.; Krinner, S.; Kollath, C.; Esslinger, T.; Georges, A. *Science* **2013**, *342*, 713–715.

(12) Anderson, M. H.; Ensher, J. R.; Matthews, M. R.; Wieman, C. E.; Cornell, E. A. *science* **1995**, *269*, 198–201.

(13) Myatt, C.; Burt, E.; Ghrist, R.; Cornell, E. A.; Wieman, C. *Physical Review Letters* **1997**, *78*, 586.

(14) Bu ča, B.; Jaksch, D. *Phys. Rev. Lett.* **2019**, *123*, 260401.

(15) Dogra, N.; Landini, M.; Kroeger, K.; Hruby, L.; Donner, T.; Esslinger, T. *Science* **2019**, *366*, 1496–1499.

(16) Barontini, G.; Hohmann, L.; Haas, F.; Estève, J.; Reichel, J. *Science* **2015**, *349*, 1317–1321.

(17) Gaunt, A. L.; Fletcher, R. J.; Smith, R. P.; Hadzibabic, Z. *Nature Physics* **2013**, *9*, 271–274.

(18) Langen, T.; Geiger, R.; Schmiedmayer, J. *Annual Review of Condensed Matter Physics* **2015**, *6*, 201–217.

(19) Hofferberth, S.; Lesanovsky, I.; Fischer, B.; Schumm, T.; Schmiedmayer, J. *Nature* **2007**, *449*, 324–327.

(20) Trotzky, S.; Chen, Y.-A.; Flesch, A.; McCulloch, I. P.; Schollwöck, U.; Eisert, J.; Bloch, I. *Nature Physics* **2012**, *8*, 325–330.

(21) Sadler, L. E.; Higbie, J. M.; Leslie, S. R.; Vengalattore, M.; Stamper-Kurn, D. M. *Nature* **2006**, *443*, 312–315.

(22) Smith, R. P.; Beattie, S.; Moulder, S.; Campbell, R. L.; Hadzibabic, Z. *Physical review letters* **2012**, *109*, 105301.

(23) Gring, M.; Kuhnert, M.; Langen, T.; Kitagawa, T.; Rauer, B.; Schreitl, M.; Mazets, I.; Smith, D. A.; Demler, E.; Schmiedmayer, J. *Science* **2012**, *337*, 1318–1322.

(24) Grünzweig, T.; Hilliard, A.; McGovern, M.; Andersen, M. *Nature Physics* **2010**, *6*, 951–954.

(25) Blickle, V.; Bechinger, C. *Nature Physics* **2012**, *8*, 143–146.

(26) Roßnagel, J.; Dawkins, S. T.; Tolazzi, K. N.; Abah, O.; Lutz, E.; Schmidt-Kaler, F.; Singer, K. *Science* **2016**, *352*, 325–329.

(27) Munoz, J. M.; Wang, X.; Hewitt, T.; Kowalczyk, A. U.; Sawant, R.; Barontini, G. *arXiv preprint arXiv:2004.14686* **2020**.

(28) Liu, J.; Wang, X.; Muñoz, J. M.; Kowalczyk, A.; Barontini, G. *Scientific reports* **2019**, *9*, 1–7.

(29) Raab, E.; Prentiss, M.; Cable, A.; Chu, S.; Pritchard, D. E. *Physical Review Letters* **1987**, *59*, 2631.

(30) Steck, D. A. **2001**.

(31) Tiecke, T. *University of Amsterdam, The Netherlands, Thesis* **2010**, 12–14.

(32) Dalibard, J.; Cohen-Tannoudji, C. *JOSA B* **1989**, *6*, 2023–2045.

(33) Davidson, N.; Lee, H. J.; Kasevich, M.; Chu, S. *Physical review letters* **1994**, *72*, 3158.

(34) Boiron, D.; Michaud, A.; Lemonde, P.; Castin, Y.; Salomon, C.; Weyers, S.; Szymaniec, K.; Cognet, L.; Clairon, A. *Physical Review A* **1996**, *53*, R3734.

(35) Townsend, C.; Edwards, N.; Zetie, K.; Cooper, C.; Rink, J.; Foot, C. *Physical Review A* **1996**, *53*, 1702.

(36) Gröbner, M.; Weinmann, P.; Kirilov, E.; Nägerl, H.-C. *Physical Review A* **2017**, *95*, 033412.

(37) Landini, M.; Roy, S.; Carcagni, L.; Trypogeorgos, D.; Modugno, G. *Physical Review A* **2011**, *84*, 1504–1512.

(38) Ashkin, A. *Physical review letters* **1970**, *24*, 156.

(39) Bjorkholm, J.; Freeman, R.; Ashkin, A.; Pearson, D. *Physical review letters* **1978**, *41*, 1361.

(40) Chu, S.; Bjorkholm, J.; Ashkin, A.; Cable, A. *Physical review letters* **1986**, *57*, 314.

(41) Miller, J.; Cline, R.; Heinzen, D. *Physical Review A* **1993**, *47*, R4567.

(42) Grimm, R.; Weidemüller, M.; Ovchinnikov, Y. B. **2000**, *42*, 95–170.

(43) Nogrette, F.; Labuhn, H.; Ravets, S.; Barredo, D.; Béguin, L.; Vernier, A.; Lahaye, T.; Browaeys, A. *Physical Review X* **2014**, *4*, 021034.

(44) Barrett, M.; Sauer, J.; Chapman, M. *Physical Review Letters* **2001**, *87*, 010404.

(45) Ho, T.-L. *Physical review letters* **1998**, *81*, 742.

(46) Schmaljohann, H.; Erhard, M.; Kronjäger, J.; Kottke, M.; Van Staa, S.; Cacciapuoti, L.; Arlt, J.; Bongs, K.; Sengstock, K. *Physical review letters* **2004**, *92*, 040402.

(47) Van Kempen, E.; Kokkelmans, S.; Heinzen, D.; Verhaar, B. *Physical review letters* **2002**, *88*, 093201.

(48) Chang, M.-S.; Qin, Q.; Zhang, W.; You, L.; Chapman, M. S. *Nature physics* **2005**, *1*, 111–116.

(49) Dalfovo, F.; Giorgini, S.; Pitaevskii, L. P.; Stringari, S. *Rev. Mod. Phys.* **1999**, *71*, 463–512.

(50) Barontini, G.; Paternostro, M. *New Journal of Physics* **2019**, *21*, 063019.

(51) Barredo, D.; De Léséleuc, S.; Lienhard, V.; Lahaye, T.; Browaeys, A. *Science* **2016**, *354*, 1021–1023.

(52) Barredo, D.; Lienhard, V.; De Leseleuc, S.; Lahaye, T.; Browaeys, A. *Nature* **2018**, *561*, 79–82.

(53) Schlosser, N.; Reymond, G.; Grangier, P. *Physical review letters* **2002**, *89*, 023005.

(54) Arora, B.; Safronova, M.; Clark, C. W. *Physical Review A* **2011**, *84*, 043401.

(55) Barontini, G.; Inguscio, M.; Cuccoli, A. Ultracold Bose-Bose mixtures with tunable interspecies interactions, Ph.D. Thesis, PhD thesis, University of Firenze, 2009.

(56) Kuppens, S.; Corwin, K.; Miller, K.; Chupp, T.; Wieman, C. *Physical review A* **2000**, *62*, 013406.

(57) Chin, C.; Grimm, R.; Julienne, P.; Tiesinga, E. *Reviews of Modern Physics* **2010**, *82*, 1225.

(58) Moerdijk, A.; Verhaar, B.; Axelsson, A. *Physical Review A* **1995**, *51*, 4852.

(59) Ospelkaus, S.; Ospelkaus, C.; Dinter, R.; Fuchs, J.; Nakat, M.; Sengstock, K.; Bongs, K. *Journal of Modern Optics* **2007**, *54*, 661–673.

(60) Campbell Jr, W. A.; Scialdone, J. J. **1993**.

(61) Hommelhoff, P. **2002**.

(62) Hauth, M. **2008**.

(63) Dieckmann, K.; Spreeuw, R.; Weidemüller, M.; Walraven, J. *Physical Review A* **1998**, *58*, 3891.

(64) Schoser, J.; Batär, A.; Löw, R.; Schweikhard, V.; Grabowski, A.; Ovchinnikov, Y. B.; Pfau, T. *Physical Review A* **2002**, *66*, 023410.

(65) Meyer, N.; Proud, H.; Perea-Ortiz, M.; O'Neale, C.; Baumert, M.; Holynski, M.; Kronjäger, J.; Barontini, G.; Bongs, K. *Physical review letters* **2017**, *119*, 150403.

(66) Friebel, S.; D'Andrea, C.; Walz, J.; Weitz, M.; Hänsch, T. *Physical Review A* **1998**, *57*, R20.

(67) Jáuregui, R.; Poli, N.; Roati, G.; Modugno, G. *Physical Review A* **2001**, *64*, 033403.

(68) Stringari, S. *Physical review letters* **1996**, *77*, 2360.

(69) Ketterle, W.; Durfee, D. S.; Stamper-Kurn, D. *arXiv preprint cond-mat/9904034* **1999**.

(70) Arora, B.; Safronova, M.; Clark, C. W. *Physical Review A* **2007**, *76*, 052509.

(71) Hutzler, N. R.; Liu, L. R.; Yu, Y.; Ni, K.-K. *New Journal of Physics* **2017**, *19*, 023007.

(72) Dogra, L. H.; Glidden, J. A. P.; Hilker, T. A.; Eigen, C.; Cornell, E. A.; Smith, R. P.; Hadzibabic, Z. *Phys. Rev. Lett.* **2019**, *123*, 020405.

(73) Cornell, E. A.; Ensher, J. R.; Wieman, C. E. *arXiv preprint cond-mat/9903109* **1999**.

(74) Simoni, A.; Zaccanti, M.; D'Errico, C.; Fattori, M.; Roati, G.; Inguscio, M.; Modugno, G. *Physical Review A* **2008**, *77*, 052705.

(75) Benedicto-Orenes, D.; Kowalczyk, A.; Bongs, K.; Barontini, G. *Optics express* **2017**, *25*, 19701–19710.

(76) Jaksch, D.; Gardiner, C. W.; Zoller, P. *Phys. Rev. A* **1997**, *56*, 575–586.

(77) Gardiner, C. W.; Lee, M. D.; Ballagh, R. J.; Davis, M. J.; Zoller, P. *Phys. Rev. Lett.* **1998**, *81*, 5266–5269.

(78) Gardiner, C. W.; Zoller, P.; Ballagh, R. J.; Davis, M. J. *Phys. Rev. Lett.* **1997**, *79*, 1793–1796.

(79) Richard H., P.; Chenghui, Y.; Weicheng, Z.; Brian, E.; Holger, M. *Science* **2018**, *360*, 6385.

(80) Dimopoulos, S.; Graham, P. W.; Hogan, J. M.; Kasevich, M. A. *Physical review letters* **2007**, *98*, 111102.

(81) Rosi, G.; D'Amico, G.; Cacciapuoti, L.; Sorrentino, F.; Prevedelli, M.; Zych, M.; Brukner, Č.; Tino, G. *Nature communications* **2017**, *8*, 1–6.

(82) Dimopoulos, S.; Graham, P. W.; Hogan, J. M.; Kasevich, M. A.; Rajendran, S. *Physical Review D* **2008**, *78*, 122002.

(83) Kovachy, T.; Asenbaum, P.; Overstreet, C.; Donnelly, C.; Dickerson, S.; Sugarbaker, A.; Hogan, J.; Kasevich, M. *Nature* **2015**, *528*, 530–533.

(84) Ménoret, V.; Vermeulen, P.; Le Moigne, N.; Bonvalot, S.; Bouyer, P.; Landragin, A.; Desruelle, B. *Scientific reports* **2018**, *8*, 1–11.

(85) Keith, D. W.; Ekstrom, C. R.; Turchette, Q. A.; Pritchard, D. E. *Physical review letters* **1991**, *66*, 2693.

(86) Giltner, D. M.; McGowan, R. W.; Lee, S. A. *Physical review letters* **1995**, *75*, 2638.

(87) Wang, Y.-J.; Anderson, D. Z.; Bright, V. M.; Cornell, E. A.; Diot, Q.; Kishimoto, T.; Prentiss, M.; Saravanan, R.; Segal, S. R.; Wu, S. *Physical review letters* **2005**, *94*, 090405.

(88) Rasel, E. M.; Oberthaler, M. K.; Batelaan, H.; Schmiedmayer, J.; Zeilinger, A. *Physical Review Letters* **1995**, *75*, 2633.

(89) Sapiro, R.; Zhang, R.; Raithel, G. *Physical Review A* **2009**, *79*, 043630.

(90) Kasevich, M.; Chu, S. *Physical review letters* **1991**, *67*, 181.

(91) Freier, C.; Hauth, M.; Schkolnik, V.; Leykauf, B.; Schilling, M.; Wziontek, H.; Scherneck, H.-G.; Müller, J.; Peters, A. **2016**, *723*, 012050.

(92) Dickerson, S. M.; Hogan, J. M.; Sugarbaker, A.; Johnson, D. M.; Kasevich, M. A. *Physical review letters* **2013**, *111*, 083001.

(93) Schumm, T.; Hofferberth, S.; Andersson, L. M.; Wildermuth, S.; Groth, S.; Bar-Joseph, I.; Schmiedmayer, J.; Krüger, P. *Nature physics* **2005**, *1*, 57–62.

(94) Kreutzmann, H.; Poulsen, U.; Lewenstein, M.; Dumke, R.; Ertmer, W.; Birkl, G.; Sanpera, A. *Physical review letters* **2004**, *92*, 163201.

(95) Shin, Y.; Saba, M.; Pasquini, T.; Ketterle, W.; Pritchard, D.; Leanhardt, A. *Physical review letters* **2004**, *92*, 050405.

(96) Guarrera, V.; Szmuk, R.; Reichel, J.; Rosenbusch, P. *New Journal of Physics* **2015**, *17*, 083022.

(97) Denschlag, J.; Simsarian, J. E.; Feder, D. L.; Clark, C. W.; Collins, L. A.; Cubizolles, J.; Deng, L.; Hagley, E. W.; Helmerson, K.; Reinhardt, W. P. et al. *Science* **2000**, *287*, 97–101.

(98) Becker, C.; Stellmer, S.; Soltan-Panahi, P.; Dörscher, S.; Baumert, M.; Richter, E.-M.; Kronjäger, J.; Bongs, K.; Sengstock, K. *Nature Physics* **2008**, *4*, 496–501.

(99) Ritt, G.; Cennini, G.; Geckeler, C.; Weitz, M. *Applied Physics B* **2004**, *79*, 363–365.

(100) Meyer, N. **2015**.

(101) Wilson, A. C.; Sharpe, J. C.; McKenzie, C. R.; Manson, P. J.; Warrington, D. M. *Applied optics* **1998**, *37*, 4871–4875.

(102) Landini, M.; Roy, S.; Roati, G.; Simoni, A.; Inguscio, M.; Modugno, G.; Fattori, M. *Physical Review A* **2012**, *86*, 033421.

(103) Salomon, G.; Fouché, L.; Lepoutre, S.; Aspect, A.; Bourdel, T. *Physical Review A* **2014**, *90*, 033405.

(104) Landini, M. A tunable Bose-Einstein condensate for quantum interferometry, Ph.D. Thesis, University of Trento, 2012.

Appendix A

appendix

A.1 Locking system

Due to the most reliable frequency reference is the atomic transition itself, the best way to make a stable frequency for laser cooling is atomic absorption spectroscopy. For an ECDL, the wavelength of the semiconductor laser diode is determined by the optical dispersion property inside of the cavity. The temperature fluctuation of the environment and the injection current can perturb the optical length of the cavity and the refractive index of the material. Additionally, the optical length of the external cavity can be also perturbed by the fluctuation of ambient air pressure. all of these factors result in an instability of the laser frequency. To eliminate the temperature fluctuation, a Peltier, a bulk of the semiconductor, can absorb heat at its junction when an electric current passing by. To compensate for the frequency drift by changing the optical length of the external cavity, a piezo element is applied. (The piezoelectric effect is an electrical pressure-induced mechanical deformation in a crystal, which can be also used to actively manipulate the laser frequency in the cavity.) To differential transformation on the absorption spectrum, the signal has been shown in Fig. A.1 which is referred to as frequency modulation spectroscopy (FMS)

The oscilloscope illustrates the error signals for the ^{87}Rb and ^{85}Rb atoms, respectively.

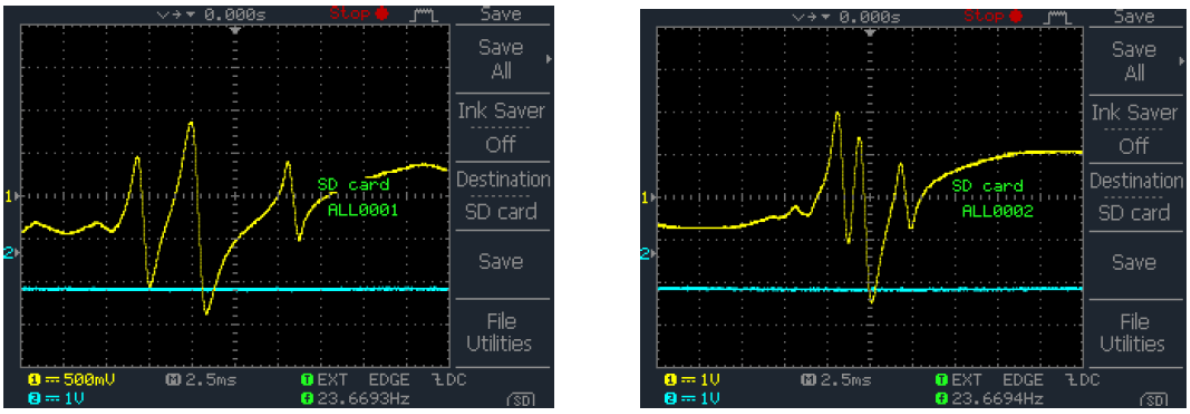


Figure A.1: Frequency modulation spectroscopy. Left panel: the error signal for ^{87}Rb; right panel: the error signal for ^{85}Rb.

The peaks from the left to the right correspond to the atomic transitions $|F = 2 > \rightarrow |F' = 2 >$, $|F = 2 > \rightarrow |F' = 2, 3 >$ and $|F = 2 > \rightarrow |F' = 3 >$ and our locking point is at the zero-crossing of the middle peak in the spectrum. The same locking mechanism is applied to the Toptica laser for ^{39}K or ^{41}K atom.

The offset locking module is also applied for ^{87}Rb atoms in our experiment. We use the same design as reference [99], the locking procedure has been shown in Fig A.2.

A beat signal can be produced from the fast photodiode (PD), whose frequency is based on the frequency difference between the master laser and the slave laser. Then, it is mixed with another RF signal from a voltage-controlled oscillator (VCO). Removing the higher-order oscillation by a low pass filter, an algorithm signal with frequency $\nu = \nu_{RF} - \nu_{VCO}$ is selected, which is subsequently split into two paths: (1) passing through a high pass filter whose cutting frequency is at the -3dB attenuation and (2) passing through a fixed -3dB attenuator. Due to the amplitude of the RF signal in the high pass filter is frequency-dependent, the frequency of the slave laser can be locked by comparing the amplitudes of RF signals in the two paths.

Despite all of the advantages, this design also has some drawbacks. For instance, the locking process provides several ms time delay in performing the frequency jump over a range of several 10 MHz, which is likely resulting from the analog electronics as shown in Fig. A.2. In principle, this can be improved by replacing the analog components with digital electronics, but it is not necessary for our experiment since the ramping time for the frequency detuning is usually more than 10 ms, the analog electronics are still competent.

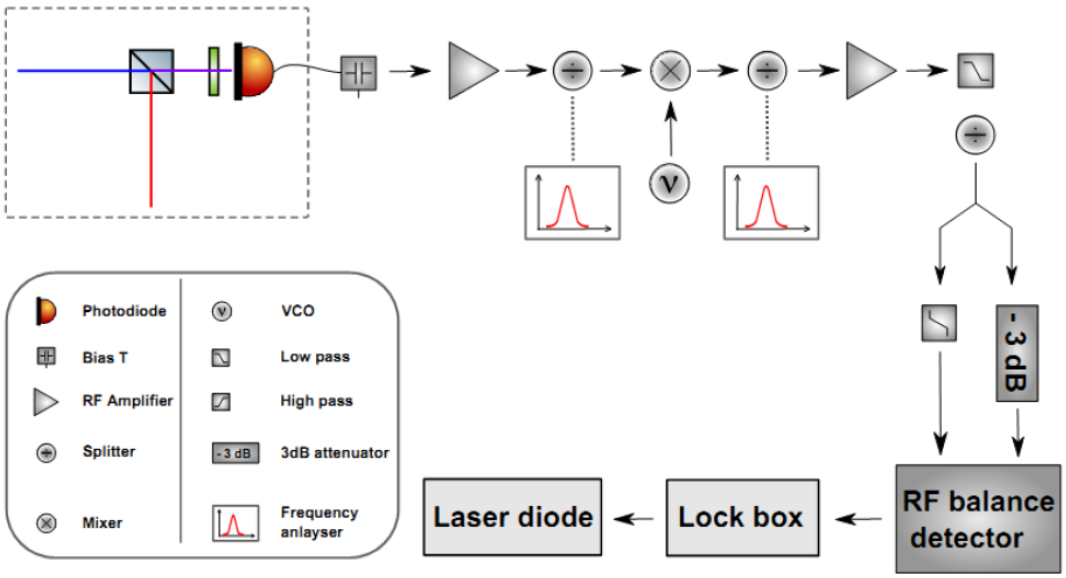


Figure A.2: Schematic principle of the offset locking: The beat signal is from a fast PD and amplified with up to 40 60dB. The power is split into two signals for a purely diagnostic reason. One is checked by a spectrum analyzer. The mixer produces a series of algorithm signals by mixing with a signal from the VCO. The consequent beat spectrum is filtered with a low pass filter, its high order contribution is removed. With the aid of another power splitter, the signal is split in half. One half passes through a constant -3dB attenuator, the other half passes through a high pass filter which has a cutting frequency at 3dB. Given that the frequency is above or below the cutting frequency, the signal experiences a larger or smaller attenuation. The amplitude response of the two signal paths is compared in the RF balance detector that gives out a voltage varying between positive and negative given which of the two signals is greater. Figure and caption taken from Ref [100].

A.2 Design of TAs and AOMs

The output power of the Vortex laser or Toptica laser is only about 20mW, a single MOT beam is on the order of a few mW itself, therefore a power amplification stage is required. This is achieved by a tapered amplifier (TA), a laser diode with a large area of output facet. The amplification of the laser power is 50-100 times [101]. The output beam of TA is irregularly expanded and it can be reformed and collimated by the optics shown in Fig. A.3

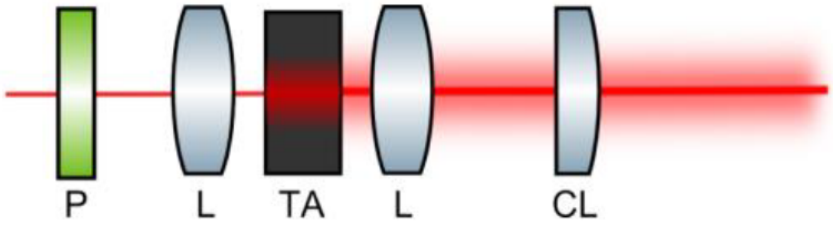


Figure A.3: Layout of the tapered amplifier: the incident seeding laser passes through a polariser (P) and is focused onto the tapered amplifier chip by a lens (L). The output laser is collimated by the collimation lens and its astigmatism is compensated by a cylindrical lens. Figure and caption taken from Ref [100].

The $\lambda/2$ wave-plate is used to align the direction of the polarisation of the seed laser, the telescope system is used to focus and collimate the laser transmission, and the cylindrical lens is used to reform the geometrical deformation of the laser. Additionally, due to the TA usually has a strong amplified spontaneous emission (ASE), the back-scattering can interfere with the stability of locking and damage the laser diode, several isolators are used before and after the TA.

After the power amplification, the beams are passing through AOMs. The double-pass design of AOM is selected instead of a single pass regime since it can adjust the alignment drift, as shown in Fig. A.4.

The RF signal triggers the AOM a mechanical oscillation in the optical crystal through an electro-acoustic transducer. This causes the incident beam deflected into a parallel multi-band beam by the crystal. Each band has an order-dependent frequency drift

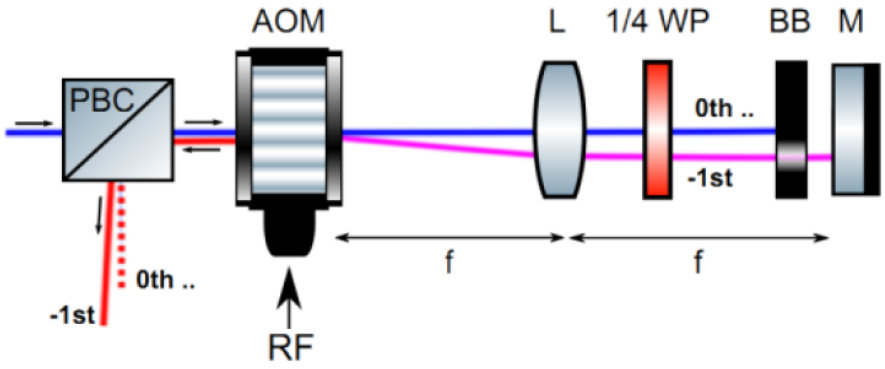


Figure A.4: Double pass regime of AOM: The linear polarised laser passes through a polarising beam cube (PBC) and the AOM. A lens (L) with a focus length of f=15cm focuses the laser onto a mirror (M). The laser passes twice through a quarter-wave plate (1/4 WP) and obtains a total polarisation shift of $\lambda/2$ followed by passing through the AOM for a second time. The output beam is deflected by the PBC to the perpendicular direction with respect to the incident beam.Figure and caption taken from Ref [100].

$\nu_{output} = \nu_{input} + m\nu_{RF}$ with respect to the carrier frequency, where m is the order number. Taking the -1st order as an example, the beam passes through the AOM and a quarter-wave plate twice, the polarisation is flipped from vertical to horizontal, which allows the output beam is deflected to a perpendicular direction by the same PBC. The beam block removes the interference light from the other orders. The frequency shift of the AOM is $-2\nu_{RF}$.

A.3 Distillation of Zeeman sub-level

In the research of the evaporative cooling of the ultracold atoms in a dissipative environment, the inter-species interaction between different ground Zeeman components of ultracold ^{87}Rb atoms is removed by distillation. In the further work of a single atom heat engine in the quantum regime, for engineering the heat exchange between the working fluid and the thermal bath, the inter-species interaction between ^{87}Rb and ^{41}K atoms is required to be controlled by the Feshbach field since the inter-species interaction is

sensitive to the Zeeman component, a state purification is necessary as well.

In the presence of an external magnetic field, an energy gap between adjacent Zeeman components can be induced, which is $\Delta E_{|F,m_F>} = g_F \mu_B m_F B_z$, where g_F is g-factor, μ_B is the Bohr magneton and since this gap is usually much smaller than the hyperfine splitting, the quantum number F can be considered as a good quantum number and the energy level can be labeled as $|F, m_F>$. Additionally, when an AC magnetic field is also applied by a small radio frequency antenna as $\tilde{B}_{RF} = |B_{RF}|cos(\omega_{RF}t + \phi)$, the total Hamiltonian can be written as

$$H = \hbar \begin{pmatrix} -p & \frac{g_B \mu_B |B_{RF}|}{\sqrt{2}\hbar} cos(\omega_{RF}t + \phi) & 0 \\ \frac{g_B \mu_B |B_{RF}|}{\sqrt{2}\hbar} cos(\omega_{RF}t + \phi) & 0 & \frac{g_B \mu_B |B_{RF}|}{\sqrt{2}\hbar} cos(\omega_{RF}t + \phi) \\ 0 & \frac{g_B \mu_B |B_{RF}|}{\sqrt{2}\hbar} cos(\omega_{RF}t + \phi) & p \end{pmatrix}$$

Where ω_{RF} is the frequency of the modulated field and p is the Zeeman splitting. We transform the Hamiltonian in a rotating frame with frequency ω_{RF} and apply the rotating wave approximation (RWA) to the Hamiltonian. It can be simplified as

$$H = \hbar \begin{pmatrix} -\Delta & \frac{\Omega_{RF}}{\sqrt{2}} & 0 \\ \frac{\Omega_{RF}}{\sqrt{2}} & 0 & \frac{\Omega_{RF}}{\sqrt{2}} \\ 0 & \frac{\Omega_{RF}}{\sqrt{2}} & \Delta \end{pmatrix}$$

where Δ is the frequency detuning of ω_{RF} with respect to the Zeeman splitting. The time evolution of the eigenstates of this Hamiltonian can be solved by

$$i\hbar \frac{d|\Phi>}{dt} = |\Phi(t=0)> e^{-\frac{i}{\hbar}Ht} \tag{A.1}$$

the population for each state is

$$
\begin{aligned}
c_{+1}^2 &= \frac{\Omega_{RF}^4}{\Omega_e^4} sin^4(\frac{\Omega_e t}{2}) \\
c_0^2 &= \frac{1}{2}[\frac{4\Delta^2\Omega_{RF}^2}{\Omega_e^4} sin^4(\frac{\Omega_e t}{2}) + \frac{\Omega_{RF}^2}{\Omega_e^2} sin(\frac{\Omega_e t}{2})^2] \\
c_{-1}^2 &= 1 - c_{+1}^2 - c_0^2
\end{aligned}
\tag{A.2}
$$

where $\Omega_e = \sqrt{\Omega_{RF}^2 + \Delta^2}$ is the effective Rabi frequency and the $c_{m_F}^2$ is the probability of the Zeeman state $|F, m_F>$. As shown in Fig. A.5

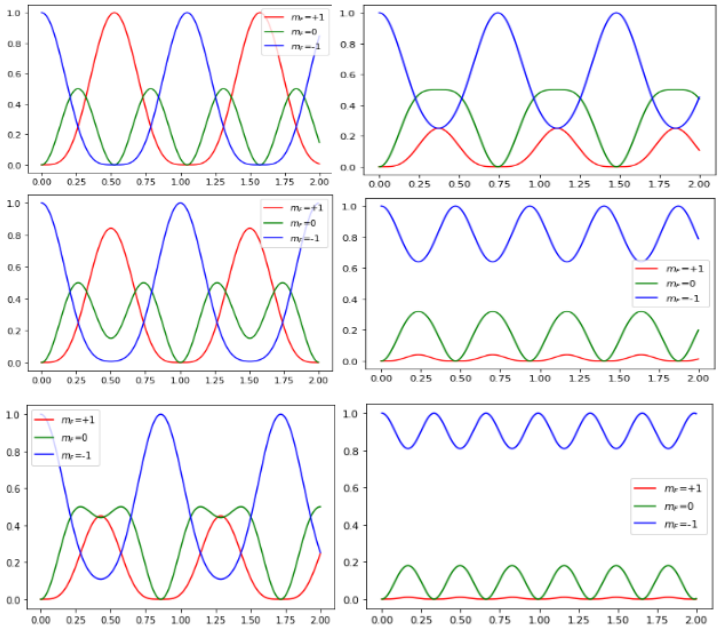


Figure A.5: Theoretical plots of Rabi oscillations. The red, green and blue lines correspond to the m_F=+1,0,-1 states respectively. Typical Rabi oscillations with different detuning are shown. In the left column from top to the bottom it illustrates the oscillation with detuning Δ=$0, 0.3\Omega_{RF}, 0.7\Omega_{RF}$, in the right column the oscillations with detuning $\Delta = \Omega_{RF}, 2\Omega_{RF}, 3\Omega_{RF}$ have been demonstrated.

To manipulate the driven time of the coupling field, the atoms can be adiabatically transferred into a selected Zeeman component. Applying a Stern-Gerlach field during the ballistic expansion, the Zeeman states can be observed in Fig. A.6

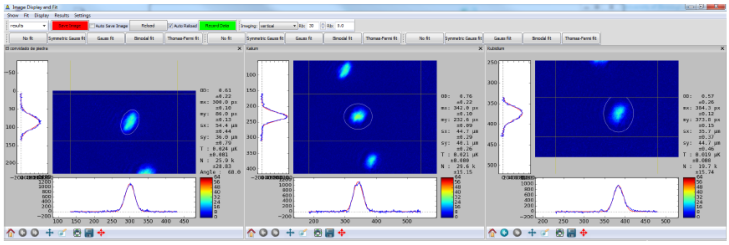


Figure A.6: Absorption imaging of different Zeeman components of the ^{87}Rb atoms

Another approach to distillate the Zeeman component is to apply a magnetic field during the evaporation. This is based on the fact that the magnetic field can increase (decrease) the trapping depth of the $|\, m_F{=}{+}1\rangle$ ($|\, m_F{=}\text{-}1\rangle$) state. The phase transition for the $|\, m_F{=}\text{-}1\rangle$ component can be induced earlier than the $|\, m_F{=}{+}1\rangle$ component within the same evaporative cooling. This method can distillate the Zeeman state to $|\, m_F = \text{-}1\rangle$ without introducing a radio-frequency field, which has been used in our research of the non-equilibrium thermodynamics of the ultracold atoms in a dissipative environment.

A.4 Effort on producing a ^{39}K BEC

An effort on loading a sufficiently large number of ^{39}K atoms into the optical dipole trap has been also made after the dark MOT and the molasses. Compared to the ^{87}Rb atoms, the density of ^{39}K atoms is 10 times lower however the temperature is also factor 4 lower as shown in Fig. A.7. Due to the PSD scales as $nT^{-2/3}$, similar behavior of the ^{39}K atoms during the evaporative cooling is expected to be observed in the dipole trap.

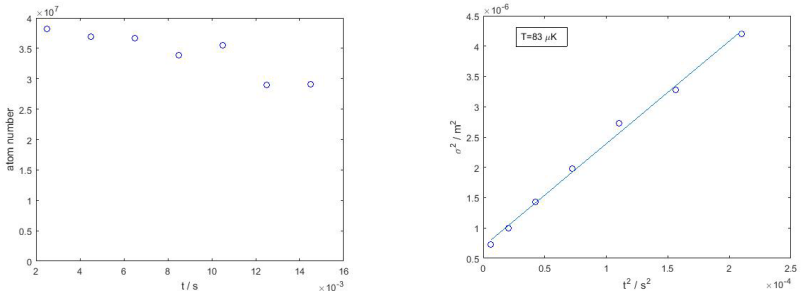


Figure A.7: Measurement of the atom number and the temperature after the sub-Doppler cooling of the ^{39}K atoms.

However, an undesired atom loss has been observed during the dipole trap loading as shown in Fig. A.8.

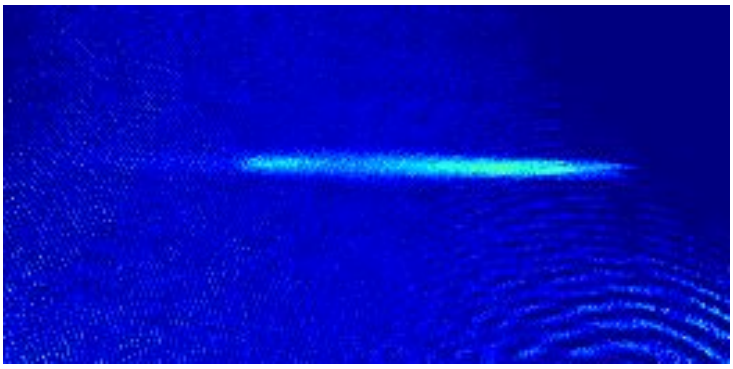


Figure A.8: Loading ^{39}K atoms in the optical dipole trap.

The ^{39}K atoms in the dipole trap favor to escape from the focus of the trap instead of being compressed towards the focus. This phenomenon strongly indicates a light-induced loss of the atoms.

As a reference, two other experiments achieved all-optical K BEC have also reported and one of them encounters a similar problem [102, 103]. One possible explanation[102, 104] is the 1070 nm laser pumps a Raman transition which can produce a bound molecular state and the binding energy of this molecule converts to kinetic energy which allows the molecule escapes from the dipole trap. This mechanism is referred to as photoassociation.

A smaller waist results in a higher laser power density that in turn means a stronger photoassociation. Thus, compared to the reference [102], the photoassociation may more severe in our experiment. In another reference [103], photoassociation has no longer been observed by using a laser at wavelength 1550 nm. Since the power of 1550 nm laser is insufficient and the D1 line gray molasses cannot be operated by our setup, an efficient evaporative cooling of ^{39}K atoms has never been succeeded in our experiment.